ELEMENTS OF OCEAN MESOSCALE EDDY-ATMOSPHERE INTERACTIONS

IN EXTRATROPICS

A Dissertation

by

XUE LIU

Submitted to the Office of Graduate and Professional Studies of
Texas A&M University
in partial fulfillment of the requirements for the degree of

DOCTOR OF PHILOSOPHY

Chair of Committee,	Ping Chang
Co-Chair of Committee,	Xiaopei Lin
Committee Members,	R. Saravanan
	Istvan Szunyogh
Head of Department,	Shari Yvon-Lewis

August 2018

Major Subject: Oceanography

ABSTRACT

As resolution of observations and climate models continues to improve, it has become increasingly evident that mesoscale eddies – a ubiquitous feature of the world ocean – can interact with the overlying atmosphere, potentially affecting large-scale atmospheric and oceanic circulation and climate. Improving our understanding of this ocean mesoscale eddy – atmosphere (OME-A) interaction has important implications for improving climate simulations and predictions. This dissertation contributes to this understanding by focusing on two elements of OME-A interaction.

The first element deals with the influence of ocean mesoscale eddies on rainfall. By comparing three different satellite-derived rainfall datasets, we examined the robustness of the rainfall response to ocean eddy induced mesoscale sea-surface temperature anomalies (SSTAs). The three datasets are the Tropical Rainfall Measurement Mission (TRMM) Multi-satellite Precipitation Analysis (TMPA), NOAA Climate Prediction Center (CPC) Morphing Technique (CMORPH) global precipitation and newly available Integrated Multi-satellitE Retrievals for Global Precipitation Measurement (IMERG) that is based on the latest remote sensing technology with finer spatial and temporal resolution. The results show that 1) all datasets exhibit a similar rainfall response to ocean eddies, but the amplitude of the rainfall response varies among datasets with IMERG producing the strongest and most coherent rainfall response, despite the weakest time-mean rainfall, 2) eddy-induced precipitation response is

significantly stronger in winter than in summer and over warm eddies than cold eddies, and these asymmetries in rainfall response is more robust in IMERG than in the other two datasets. Documenting and analyzing these asymmetric rainfall responses are important for understanding the potential role of ocean eddies in forcing the large-scale atmospheric circulation and climate.

The second element examines the effect of OME-A interaction on ocean eddy wind power that plays a vital role in dissipating eddy kinetic energy (EKE). By using a scaling analysis and analyzing eddy-resolving coupled climate model simulations, we not only quantify the impact of OME-A interaction on eddy wind power, but also provide a mechanistic understanding of the underlying process. Results show that the impact of OME-A feedback on eddy wind power, albeit smaller than that due to ocean current feedback, is significant and amounts to about 30-40% reduction of the value without OME-A interaction. Therefore, in the absence of OME-A interaction, eddy wind power is significantly overestimated, thus providing a too-strong sink for EKE.

DEDICATION

I dedicate this dissertation to my husband, Dan Fu and our daughter, Evelyn Fu.

ACKNOWLEDGMENTS

I would like to express my appreciation to all those who have helped me during my Ph.D. study at Texas A&M University.

The deepest appreciation goes to my advisor, Dr. Ping Chang, for all of his constant encouragement and guidance. He has walked me through all the stages of writing this dissertation. Without his support and constructive instructions, this dissertation would not have been possible. His broad knowledge, perspective insight and responsible scientific attitude help me be a better scientist and will exert a lifelong influence on me.

I would also like to express my gratitude to my Co-Chair Prof. Xiaopei Lin, who led me into the world of physical oceanography, as well as my committed members, Prof. Ramalingam Saravanan and Prof. Istvan Szunyogh, who have given me a lot of provoking suggestions during my Ph.D. study over the past few years.

I would also like to thank my colleagues at Texas A&M University for their kind helps. I appreciate the constructive conversations and suggestions from Dr. Jaison Kurian, who also helped me with the eddy identification. I want to thank Dr. Xiaohui Ma who completed the regional coupled models and taught me about the model configurations, and Dr. Zhao Jing who gave me many inspirations during our discussions. My thanks

also extend to other colleagues in our research group, my friends and the faculty in the Department of Oceanography.

I am grateful to China Scholarship Council for their financial support. I am also grateful to the Texas A&M University Supercomputing Facility and the Texas Advanced Computing Center (TACC) at the University of Texas at Austin, which provided the computing resources used in this dissertation.

Finally I would like to express my deepest thanks to my parents and parents in law for their encouragement and unconditional love. Their continuous support gave me the confidence to face towards the change and overcome the difficulties. Special thanks should go to my husband, Dan Fu, whose accompany makes my life more colorful. His understanding, patience and love mean everything to me. Knowing that I could count on him everyday makes it much easier when things were hard. Finally, I would thank our little sweetheart, Evelyn Fu, who is an incredible inspiration. Having her and her father by my side makes everyday wonderful.

CONTRIBUTORS AND FUNDING SOURCES

Contributors

This work was supervised by a dissertation committee consisting of Professor Ping Chang, Professor Xiaopei Lin of the Department of Oceanography and Professor Ramalingam Saravanan, Professor Istvan Szunyogh of the Department of Atmospheric Science.

All work for the dissertation was completed independently by the student.

Funding Sources

Graduate study was supported by a fellowship from Texas A&M University and China Scholarship Council.

NOMENCLATURE

ACC	Antarctic Circumpolar Current
AMSR-E	Advanced Microwave Scanning Radiometer-Earth Observing System
AMSU	Advanced Microwave Sounding Unit
AVISO	Archiving, Validation, and Interpretation of Satellite Oceanographic data
CAM5	Community Atmosphere Model version 5
CCMP	Cross-Calibrated Multi-Platform
CESM	Community Earth System Model
CFSR	Climate Forecast System Reanalysis
CPC	Climate Prediction Center
CRCM	Coupled Regional Climate Model
CMORPH	CPC Morphing Technique
DPR	Dual-Frequency Precipitation Radar
EKE	Eddy Kinetic Energy
GMI	GPM Microwave Imager
GPCC	Global Precipitation Climatology Centre
GPM	Global Precipitation Measurement

KEO	Kuroshio Extension Observatory
IMERG	Integrated Multi-satellitE Retrievals for GPM
IR	Infrared
MHS	Microwave Humidity Sounder
MW-IR	Merged Microwave and Infrared
NCEP-II	National Center for Environmental Prediction-II
OME-A	Ocean Mesoscale Eddy-Atmosphere
OCS	Ocean Climate Stations Project
PAM	Pressure Adjustment Mechanisms
PBL	Planetary Boundary Layer
POP2	Parallel Ocean Program version 2
ROMS	Regional Ocean Modeling System
SLA	Sea Level Anomaly
SODA	Simple Ocean Data Assimilation
SSMI	Special Sensor Microwave Imager
SSMIS	Special Sensor Microwave Imager/Sounder
SSH	Sea Surface Height
SST	Sea Surface Temperature
SSTA	Sea Surface Temperature Anomalies
SSTAs	Ocean Eddy Induced Mesoscale Sea Surface Temperature

	Anomalies
TCI	TRMM Combined Instrument
TMI	TRMM Microwave Imager
TMPA	TRMM Multi-satellite Precipitation Analysis
TRMM	Tropical Rainfall Measuring Mission
VMM	Vertical Mixing Mechanism
WRF	Weather Research Forecasting

TABLE OF CONTENTS

Page

ABSTRACT ii

DEDICATION iv

ACKNOWLEDGEMENTS v

CONTRIBUTORS AND FUNDING SOURCES vii

NOMENCLATURE viii

TABLE OF CONTENTS xi

LIST OF FIGURES xiii

CHAPTER I INTRODUCTION 1

1.1 Background 1
1.1.1 Ocean mesoscale eddies 1
1.1.2 Energy cycle of the ocean 3
1.1.3 Oceanic Mesoscale Eddy-Atmsophere interaction 5
1.1.4 Impacts Of OME-A interaction on the atmosphere 7
1.1.5 Impacts Of OME-A interaction on the ocean 9
1.1.6 Implications for improving numerical models and for climate prediction 11
1.2 Motivations and Objectives 12
1.2.1 Motivations and objectives of Chapter 2 13
1.2.2 Motivations and objectives of Chapter 3 14

CHAPTER II SATELLITE OBSERVED PRECIPITATION RESPONSE TO OCEAN MESOSCALE EDDIES 15

2.1 Introduction 15
2.2 Data and Method 15

2.2.1 Satellite Precipitation Datasets 18
2.2.2 Eddy Identification 21
2.2.3 Rainfall Composite 23
2.3 Overall Rainfall Characteristics 24
2.3.1 Satellite Observation 24
2.3.2 Validation against in situ measurement 25
2.3.3 Systematic Differences among the Three Satellite Observations 30
2.4 Response to Ocean Mesoscale Eddies 32
2.4.1 Response Differences among the Three Satellite Observations 32
2.4.2 Response during Winter and Summer 39
2.4.3 Response to Warm-Core Anticyclonic and Cold-Core Cyclonic Eddies 41
2.5 Discussion and Conclusion 46

CHAPTER III ASSESSING EFFECT OF MESOSCALE AIR-SEA INTERACTION ON OCEAN EDDY WIND POWER 50

3.1 Introduction 50
3.2 Models and Methods 55
3.2.1 High-resolution Model Simulations 55
3.2.2 Eddy Identification and Composite 60
3.3 Scaling Analysis 61
3.4 Simulated Total Wind Power *VS* Eddy Wind Power 66
3.5 Effects of OME-A Feedback on Eddy Wind Power 69
3.5.1 Eddy Wind Power Response to OME-A Feedback 69
3.5.2 Response Difference over Anticyclonic Warm Eddies *VS* Cyclonic Cold Eddies 72
3.5.3 Wind Stress Response 79
3.5.4 Response Difference between Winter and Summer 80
3.6 Summary 84

CHAPTER IV CONCLUSIONS AND FUTURE WORK 86

4.1 Conclusions 87
4.2 Future Work 91

REFERENCES 93

LIST OF FIGURES

Page

FIG. 2.1. April 2014 – Jan 2016 mean rainfall derived from daily mean precipitation data (mm day^{-1}) of a) TMPA 3B42, b) CMORPH and c) IMERG. Black dash boxes mark the regions where eddy-induced rainfall response is analyzed. 27

FIG. 2.2. 11-year mean rainfall (mm day^{-1}) computed from daily mean a) TMPA 3B42 and b) CMORPH data. Black dash boxes mark the regions where eddies are identified and tracked for analyzing eddy-induced rainfall response. 28

FIG. 2.3. Relative differences of daily mean rainfall between TMPA and KEO buoy (cyan), between IMERG and KEO buoy (orange), between CMORPH and KEO buoy (magenta) in reference to the KEO buoy mean rainfall. Satellite rainfall values are derived by averaging over various square boxes centered on the KEO buoy location whose dimension ranges from 0.1° to 5° as shown in x-axis. The dots show mean values of the relative difference and the vertical bars show 95% confidence intervals. 29

FIG. 2.4. Scatterplots of CMORPH (upper panel) and IMERG (lower panel) versus TMPA 3B42 area-averaged daily mean rain rates from April 2014 to January 2016 for Kuroshio Extension (a, e), Gulf Stream (b, f), Agulhas Current retroflection (c, g) and Brazil-Malvinas confluence (d, h). The grey diagonal line in each plot indicates the one-to-one relationship and the black line is the least square linear fit. Legends in each plot show r2 and the slope of the linear fit b. 29

FIG. 2.5. Scatterplots of 11-year CMORPH versus TMPA 3B42 area-averaged daily mean rainfall over a) Kuroshio Extension, b) Gulf Stream, c) Agulhas Current retroflection and d) Brazil-Malvinas confluence. The grey diagonal line in each plot indicates the one-to-one relationship and the black line is the least square linear fit. Legends in each plot show r2 and the slope of the linear fit b. 30

FIG. 2.6. Probability Density Function (PDF) of daily rainfall from KEO buoy (white), TMPA 3B42 (cyan), IMERG (orange) and CMORPH (magenta). The unit of x-axis is mm day^{-1} $grid^{-1}$ 31

FIG. 2.7. Composite of normalized warm-core anticyclonic eddies minus cold-core cyclonic eddies for a) SSTAs (contours and color, °C), b) precipitation

anomaly derived from TMPA 3B42 (contour and color, mm day^{-1}), c) precipitation anomaly derived from CMORPH (contour and color, mm day^{-1}), d) precipitation anomaly derived from IMERG (contour and color, mm day^{-1}) during the overlapping period (upper panel). Summer and winter composites are shown in middle and lower panel, respectively. White contour and dot in each panel mark one eddy radius and eddy center. 32

FIG. 2.8. Composite of 11-year normalized warm-core anticyclonic eddies minus cold-core cyclonic eddies for a) SSTAs (contours and color, ^{o}C), b) precipitation anomaly derived from TMPA 3B42 (contour and color, mmd^{-1}), c) precipitation anomaly derived from CMORPH (contour and color, mmd^{-1}). White contour and dot mark one eddy radius and eddy center. The composite method is the same as in Fig. 2.7. 34

FIG. 2.9. Composite of normalized warm-core anticyclonic eddies minus cold-core cyclonic eddies for a) light rain type b) moderate rain type c) heavy rain type from TMPA 3B42 (upper panel), IMERG (middle panel), and CMORPH (lower panel) during the overlapping period. The composite method is the same as in Fig. 2.7. The black contour interval is 0.1 mmd^{-1}. Note that colorbar scales are different for light, moderate and heavy rains. 36

FIG. 2.10. Composite of normalized warm-core anticyclonic eddies minus cold-core cyclonic eddies for a) the original 0.1 degree IMERG (contour and color, mm day^{-1}) b) subsampled 0.2 degree, c) 0.3 degree, and d) 0.4 degree IMERG during the overlapping period. The composite method is the same as in Fig. 2.7. 38

FIG. 2.11. Difference between winter and summer rainfall PDFs (winter minus summer) for TMPA 3B42 (cyan), IMERG (orange) and CMORPH (magenta) over extratropical eddy-active frontal zones. The unit of x-axis is mm day^{-1} $grid^{-1}$. 40

FIG. 2.12. Composite of a) SSTAs (^{o}C), b) TMPA 3B42, c) CMORPH, d) IMERG rain anomalies (mmd^{-1}) for cold-core cyclonic eddies (upper panel) and warm-core anticyclonic eddies (lower panel) during the overlapping period. .. 43

FIG. 2.13. Composite of a) SSTAs (^{o}C), b) TMPA 3B42, c) CMORPH, d) IMERG rain anomalies (mmd^{-1}) for cold-core cyclonic eddies (upper panel) and warm-core anticyclonic eddies (lower panel) during winter. 43

FIG. 2.14. Composite of a) SSTAs (^{o}C), b) TMPA 3B42, c) CMORPH, d) IMERG rain anomalies (mmd^{-1}) for cold-core cyclonic eddies (upper panel) and warm-core anticyclonic eddies (lower panel) during summer. 44

FIG. 2.15. Binned averages of IMERG rainfall anomaly over warm eddies (red scatter) and cold eddies (blue scatter). Error bar refers to standard deviation. A nonlinear fitted line (black line) shows the response strength of rainfall anomalies to SST anomalies 45

FIG. 2.16. Binned averages of IMERG rainfall anomaly over warm eddies (red scatter) and cold eddies (blue scatter) in summer (upper panel) and winter (lower panel). Error bar refers to standard deviation. A nonlinear fitted line (black line) shows the relationship between rainfall and SST anomalies across all eddies 45

FIG. 3.1. One snapshot of a) original SST; b) smoothed SST; c) SST differences between control and smoothed ensembles in CRCM. 57

FIG. 3.2. One snapshot of a) original SST; b) smoothed SST; c) differences between original and smoothed SST in CESM. Black boxes mark the regions where the feedback of OME-A interaction is analyzed. 59

FIG. 3.3. Schematic summarizing the impact of anticyclonic warm eddies (red, left) and cyclonic cold eddies (blue, right) on the overlying lower atmosphere for vertical mixing mechanism. From Frenger et al. 2013. 62

FIG. 3.4. Schematic summarizing the impact of anticyclonic warm eddies (right) and cyclonic cold eddies (left) on the overlying lower atmosphere for pressure adjustment mechanism. 62

FIG. 3.5. Wind power (mW/m^2) derived from the CESM control simulation. (a) Total wind power and (b) eddy wind power. 65

FIG. 3.6. Wind power (mW/m^2) derived from the CRCM control ensemble. (a) Total wind power and (b) eddy wind power. 67

FIG. 3.7. Coherence between surface winds and SST. Coherence between surface winds and SST in wave length space in CRCM control ensemble (blue) and the smoothed ensemble (red). Shades indicate the corresponding standard deviation. 68

FIG. 3.8. Eddy wind power (mW/m^2) difference between CESM smoothed and control simulations. 71

FIG. 3.9. Eddy wind power (mW/m^2) difference between CRCM smoothed and control ensembles. 71

FIG. 3.10. Composite of cyclonic cold eddies (Upper two panels) and anticyclonic warm eddies (lower two panels) for (a) eddy wind power (W/m^2), (b) eddy

current (m/s), (c) mesoscale wind stress (N/m^2) from the CESM smoothed simulation (first and third panels) and control simulation (second and fourth panels) over Kuroshio Extension region during winter. White contour and dot mark one eddy radius and eddy center..... 73

FIG. 3.11. Composite of cyclonic cold eddies (Upper two panels) and anticyclonic warm eddies (lower two panels) for (a) eddy wind power (W/m^2), (b) eddy current (m/s), (c) mesoscale wind stress (N/m^2) from CRCM smoothed ensemble (first and third panels) and control ensemble (second and fourth panels) over Kuroshio Extension region during winter. White contour and dot mark one eddy radius and eddy center..... 74

FIG. 3.12. Composite of cyclonic cold eddies (Upper two panels) and anticyclonic warm eddies (lower two panels) for (a) eddy wind power (W/m^2), (b) eddy current (m/s), (c) mesoscale wind stress (N/m^2) from CESM smoothed simulations (first and third panels) and control simulations (second and fourth panels) over Brazil-Malvinas Confluence during winter. White contour and dot mark one eddy radius and eddy center..... 78

FIG. 3.13. Illustration of how OME-A feedback affects mesoscale wind stress structure over an anticyclonic warm eddy in the northern hemisphere. The upper panel shows patterns without OME-A feedback, and the lower panel includes the feedback. Circles with red center indicate the anticyclonic warm eddies. Hollow arrows represent large-scale background wind speed blowing over the eddies. Dashed arrows are eddy currents. Considering currents effects only, the structure of total wind stress is shown as figure c, while including the OME-A feedback, the total wind stress is adjusted from figure c to figure g as shown by the red arrows. After applying spatial filter, patterns of mesoscale wind stress are shown in figure d and h without and with OME-A feedback. .. 79

FIG. 3.14. Mean eddy wind power (mW/m^{-2}) derived from CESM simulations during winter (a) and summer (b), and difference between smoothed and control simulations (smoothed-control) in winter (c) and summer (d)..... 81

FIG. 3.15. Comparisons of eddy wind power (W/m^2) in winter (left panel) and summer (right panel) over cyclonic cold eddies (Upper two panels) and anticyclonic warm eddies (lower two panels) in Kuroshio Extension from CRCM smoothed (the first and third panel) and control (the second and forth panel) simulations.White contour and dot mark one eddy radius and eddy center..... 83

CHAPTER I

INTRODUCTION

1.1 Background

1.1.1 Ocean mesoscale eddies

Ocean mesoscale eddies are swirls of currents with radius ranging from 25 to 250 kilometers and lifetime ranging from 10 to 100 days (Morrow and Le Traon 2012). They are divided into two groups based on their polarities: cyclonic eddies rotate counterclockwise in the northern hemisphere and clockwise in the southern hemisphere; and opposite for anticyclonic eddies. Ocean mesoscale eddies dominate the ocean kinetic energy and play an important role in mixing and transferring the momentum and water properties such as the mass, heat and salt (Zhang et al. 2014).

Ocean mesoscale eddies originate from either baroclinic instability of background currents converting the available potential energy of the mean flow into eddy energy (Gill et al. 1974), or instability of Rossby waves transferring wave energy to eddies as waves break (LaCasce and Pedlosky 2004). Standard deviation map of sea surface height (SSH) is often used to gauge mesoscale eddy activities in the global ocean, because of geostrophic constraint readily applied to these eddies. Large (small) SSH standard deviation regions are indicative of strong (weak) eddy activities. Some exceptions apply to the eastern subtropics of the south Pacific and North Atlantic, where eddies are

abundant but SSH standard deviation is small, and to the eastern North Pacific near tropics, where Rossby waves are dominant instead of ocean eddies (Chelton et al. 2007).

Ocean mesoscale eddies propagate nearly due westward with small distinct meridional deflections for cyclonic eddies (poleward) and anticylonic eddies (equatorward) at the speed nearly equaling to the long baroclinic Rossby wave phase speed (Chelton et al. 2011) except in regions of strong currents or strong bathymetric steering where eddies are advected by ocean circulation such as in the Antarctic Circumpolar Current (ACC) (Morrow and Le Traon 2012).

Ocean eddies normally have different water masses with distinct temperature and salinity from their surrounding environments. As eddies break off from an oceanic meandering jet of large temperature gradients, they trap warm or cold water inside of themselves depending on their polarity. For example, along the Gulf Stream, water is much warmer in the south than that in the north, the rightward (leftward) spin-off creates a counterclockwise (clockwise) cyclonic (anticyclonic) eddy with cold (warm) water inside. As such, typically anticyclonic eddies have warm sea surface temperature (SST) anomalies (SSTA) comparing to the surrounding water, while cyclonic eddies have cold SSTA. As a result, ocean mesoscale eddies make a significant contribution to SST variability along western boundary current regimes, such as the Kuroshio Extension and Gulf Stream (O'Neill et al. 2010, Ma et al. 2015), where eddies are energetic and background temperature gradient is strong.

1.1.2 Energy cycle of the ocean

The atmosphere works like a heat engine, in which warm air rises from the surface at low latitudes and cold air sinks from the upper atmosphere in subtropics, converting the radiation energy into kinetic energy. However, unlike the atmosphere, the ocean is not an efficient heat engine and its large-scale circulation is mainly driven by the momentum flux from the atmosphere. Due to the complex and multi-scale nature of the ocean circulation, pathways of the energy transfer in the ocean interior, exchange with the atmosphere, and dissipation are multifaceted. Understanding the oceanic energy cycle is critically important for understanding both the general circulation and its perturbations, such as eddies, in the ocean.

There is an abundance of literatures exploring the energy cycle of the ocean (e.g. von Storch et al. 2012; Chen, 2013). Winds, tides and other forms of external forcing, such as the heat and freshwater transport, seafloor thermal heating and so on, supply energy to the ocean (Ferrari and Wunsch, 2010). This energy uptake is to maintain a general circulation system of the ocean. Within this circulation system, energy can either be converted in the direction from the mean flows to the time-varying perturbations through the barotropic, baroclinic and mixing instability processes (e.g. Gill et al. 1974; Pedlosky, 1987; von Storch et al. 2012), or in the opposite direction through other processes like the rectification and topography steering (e.g. McWilliams et al. 1978; Witter and Chelton, 1998). The potential energy of the ocean is mainly constrained within the large-scale mean flows (Gill et al. 1974), while the kinetic energy is dominated

by time-varying mesoscale eddies. Waves and eddies act as energy reservoirs and redistribute the energy to a different location through their advection or propagation (e.g. Flierl 1977). Furthermore, energy can be transferred through various spatial scales or vertical modes through energy cascading processes (Salmon 1978; Scott and Wang, 2005).

Lorenz's seminal work on the energy cycle of atmospheric circulation (Lorenz, 1955) lays the foundation for our understanding the energy cycle of ocean circulation. In the Lorenz energy cycle, eddy-mean flow interactions play a critical role. Due to the limitation of ocean observations, diagnostic analyses of ocean eddy energy budget are mostly performed using eddy-resolving ocean general circulation models (e.g. von Storch et al. 2012). Winds provide a dominant energy source to the ocean by working on the ocean surface currents. According to the Lorenz energy cycle, available potential energy of the mean flow can be converted into eddy available potential energy and then into eddy kinetic energy. von Storch et al. (2012) use a 1/10 degree STORM/NCEP simulation to estimate the Lorenz energy cycle. They show that most of the kinetic energy in the ocean is dissipated through the dissipation of eddy kinetic energy, and for both the mean kinetic energy and the mean potential energy, the generation term is, to a first approximation, balanced by the dissipation term. As such, they conclude that the eddy-mean flow interaction is less important to maintain large-scale ocean circulation compared to the atmosphere. However, recent studies (e.g., Ma et al. 2016, Renault et al., 2016) demonstrate that in certain frontal regions, such as the Kuroshio Extension Region

and Gulf Stream Extension Region, mesoscale eddies can play a role in modulating the oceanic large-scale circulation through their interactions with the atmosphere, which will be further discussed in the following section.

1.1.3 Oceanic Mesoscale Eddy-Atmsophere interaction

Studying interactions between the ocean and atmosphere is of particular importance to the understanding of both atmosphere and ocean circulations (Chelton and Xie 2010). Winds blow over the ocean providing momentum to drive the ocean circulation and, at the same time, also cool the ocean through turbulent heat fluxes. Meanwhile the ocean provides heat and moisture fluxes to the atmosphere. Evaporation transports water vapor into the marine boundary layer, which in turn can affect atmospheric circulations through moist diabatic processes (Chelton and Xie 2010).

Up to a decade ago, strong ocean-atmosphere interactions were believed to primarily occur at large scales in the tropics. However, recent progress in satellite observations of SST and surface winds with high resolution of 50km or less reveals that interactions between the ocean and atmosphere is scale-dependent. On atmospheric synoptic and larger scales (>1000km), extratropical ocean-atmosphere interactions are passive, in which SST is primarily responding to large-scale latent and sensible heat flux changes, resulting in a negative correlation between SST and heat fluxes (Barsugli and Battisti, 1998). On the contrary, at the oceanic mesoscales (10-1000km) the atmosphere is forced by the ocean and there is an active coupling between the ocean and atmosphere. This

active coupling leads to a positive correlation between SST and surface wind (Chelton et al. 2004; Xie 2004; Small et al. 2008; Chelton and Xie 2010; O'Neill et al. 2010; 2012). And both the wind speed and the wind stress are found approximately linearly related to mesoscale SSTs despite the nonlinear relationship between themselves (O'Neil et al. 2012). The positive correlation between wind and mesoscale SST is particularly prevalent over the major ocean fronts such as the Gulf Stream, Kuroshio, Agulhas Return Current and Brazil-Malvinas Confluence, where the SST variations are strong (Chelton et al. 2004; Park et al. 2006; O'Neill et al. 2005; Tokinaga et al. 2005; Bryan et al. 2010; O'Neill et al. 2010; 2012).

Recent studies (Frenger et al. 2013; Ma et al. 2015a; Byrne et al. 2015) further identified the imprints of ocean eddies in wind speed field directly, and showed that atmospheric response to eddy-induced SST is not limited to surface wind speed but also quantifiable in satellite-derived cloud fraction, cloud liquid water, water vapor and rainfall. Over the anticyclonic (cyclonic) warm-core (cold-core) eddies, surface wind speed increases (decreases), water content and cloud fraction improves (declines), and rainfall enhances (reduces). Ma et al. (2016) identify the eddy imprints in the turbulent heat flux field. The linear regression between SST anomalies and turbulent heat flux anomalies across the ocean eddies based on satellite observed SST and reanalysis turbulent heat flux shows 40-56 Wm^{-2} increase of turbulent heat flux into the atmosphere per SST increase.

1.1.4 Impacts Of OME-A interaction on the atmosphere

There is no doubt that this ocean mesoscale eddy-atmosphere (OME-A) interaction is important in modifying turbulence within the marine boundary layer. However to what extent it can affect beyond the boundary layer remains unclear. Minobe et al. (2008, 2010) reveal that the influence of the Gulf Stream extends throughout the entire troposphere. The pressure adjustment to the warm flank of the Gulf Stream leads to the surface wind convergence, which anchors the rainfall band and drives the upward motion and even a deep convection. This implies the importance of mesoscale SST fronts in shaping the regional climate. However, a recent study by O' Neil et al. (2017) provides evidences that the Gulf Stream convergence zone may be attributed to the frequent storm systems propagating along the storm track aligning with the Gulf Stream, instead of the SST gradients, indicating the deep convection revealed in Minobe et al. (2008, 2010) may not be forced by overlying SST. Frenger et al. (2013) consider that the effect of OME-A interaction is restricted within the marine boundary layer based on the fact that eddy-induced atmospheric responses in winds, cloud and rainfall fields are relatively small comparing to their mean state, and thus it is difficult for eddies to exert a significant influence on atmospheric circulations above the marine boundary layer (Chelton 2013). This leads the question where OME-A can have any significant influence on weather and climate variability (Chelton 2013). However, Ma et al. (2015a) present some evidence that the atmospheric response to ocean eddies over the Kuroshio Extension can extend beyond the boundary layer. Using high-resolution National Centers

for Environmental Prediction Climate Forecast System Reanalysis (CFSR) data, they are able to analyze the vertical structures of atmospheric response. Their results show the influence of OME-A interaction is not just confined within the marine boundary layer. Over warm eddies, the boundary layer becomes deeper and positive vertical velocity anomalies can penetrate into the free atmosphere. There is a positive correlation between mesoscale SST and convective rainfall anomalies that points to the possibility of ocean eddies affecting free troposphere.

Although the issue of whether individual ocean eddies can produce deep convective rainfall remains to be unsettled and deserves further investigations, recent studies (O' Reilly and Czaja 2015; O' Reilly et al. 2017; Ma et al. 2015, 2017) reveal that ocean eddies have the potential to affect large-scale atmospheric circulations. O' Reilly and Czaja (2015) show that the strength of the north Pacific storm track is affected by the SST gradient associated with the meandering Kuroshio Extension front. When the Kuroshio Extension front is stable (meandering), cross-frontal SST gradient becomes strong (weak), transient eddies transport more heat into the western (eastern) Pacific region leading to an increase (decrease) in the low-level baroclinicity. O' Reilly et al. (2017) further demonstrate that the Gulf Stream SST affects the wintertime north Atlantic jet with a northern position during the period of high eddy heat flux. Ma et al. (2015, 2017) shows that Kuroshio eddies can produce a large-scale moisture change within the marine boundary layer, which in turn can change winter cyclongenesis through moist baroclinic instability or diabatic Rossby wave processes. As a result, even if individual

eddies do not produce deep convective response in the atmosphere, they may collectively exert an influence on large-scale atmospheric circulations by affecting lower atmosphere and marine boundary layer moisture budget, which in turn affects cyclogenesis and storm tracks. In conclusion, even though there is no concise on whether or not individual eddies can influence beyond the marine boundary layer and produce deep convective response, mesoscale SSTs still have the potential to modulate the large-scale atmospheric circulations. Thus, understanding eddies' influence on the atmosphere is important for understanding the weather and climate variability.

1.1.5 Impacts of OME-A interaction on the ocean

It is broadly accepted that OME-A interactions can feed back on the ocean eddies themselves and the associated ocean circulation. This feedback can take in both thermodynamical and dynamical form. In the former, changes in wind speed and cloud fraction caused by eddy-induced SST in turn dampen the temperature anomalies within the eddy interior and thus attenuate ocean eddies (Frenger et al. 2013; Chelton 2013). In the latter, eddy-induced wind changes generate small-scale perturbations in wind curl and divergence fields with the magnitude comparable to the large-scale wind forcing to the ocean, affecting eddy circulations (Chelton et al. 2004, 2007; O'Neil et al. 2005, 2010). Satellite observation analyses show that eddy-induced wind stress curl and divergence are linearly related to perturbations in crosswind and downwind SST gradients, respectively (Chelton et al. 2004, 2007; O'Neil et al. 2005, 2010). Finally, wind stresses can also be

influenced by ocean eddies. Although the change in wind stresses caused by OME-A interaction is relatively small compared to the associated change induced by eddy currents, it can affect vertical velocities in eddy interior (Chelton 2013) and the eddy energetics (Jin et al. 2009). A dipole structure of vertical velocity has been observed within an eddy, upwelling on one side and downwelling on the opposite side. And eddy kinetic energy is shown to decrease by about 25% due to OME-A feedback in a numerical model simulation (Jin et al. 2009).

In addition to the feedback onto ocean eddies, Ma et al. (2016) show that OME-A feedback can make a significant contribution in controlling and regulating the western boundary currents. Conventional ocean circulation theories describe western boundary currents as solely determined by ocean internal dynamics without taking into consideration ocean-atmosphere interactions. However, as shown in chapter 1.1.3, OME-A acts to remove eddy potential energy into the atmosphere through turbulent heat fluxes. Using eddy-resolving coupled climate model simulations, Ma et al. (2016) demonstrate that suppressing OME-A feedback can lead to a weakening in the Kuroshio Extension Jet strength by about 20~40%. This is because in the absence of OME-A interaction, destruction of eddy potential energy is weakened by about 70%, resulting in a reduction of eddy potential energy production. As a result, the Kuroshio Extension Jet that provides available potential energy to ocean eddies must be weakened accordingly. Understanding this process has major implications for improving climate model biases in the western boundary current regimes.

1.1.6 Implications for improving numerical models and for climate predictions

The significance of OME-A interaction in ocean and atmosphere circulations implies that proper representation of this interaction in climate models can help reducing model biases. Furthermore, the long persistence of ocean eddies may also provide a source of predictability of intraseasonal climate variability through OME-A interaction.

Most current generation climate models are not eddy-resolving due to high computational cost for running at eddy-resolving resolutions (~10 km). The coarse-resolution models underestimate the coupling between mesoscale SST and wind speed, wind stress (Chelton and Xie 2010) and heat fluxes (Griffies et al. 2015). Current climate models have difficulties in accurately simulating the strength and the position of the oceanic fronts associated with western boundary currents and ocean eddies (Kwon et al. 2010). The weak fronts in these models lead to ocean temperature bias. Previous studies (e.g. Small et al. 2014) show that improving spatial resolution of ocean models can only partially fix the bias of ocean fronts. Although the value of simulated eddy kinetic energy in high-resolution eddy-resolved models is comparable to the observed, its distribution remains different, particularly the extension of high eddy kinetic energy regions along major oceanic fronts in western boundary current regimes are generally underestimated (Maltrud and McClean, 2005). Since these oceanic fronts are critical in driving atmosphere circulations and anchoring the storm tracks, an accurate representation of the oceanic fronts is important. Eddy-induced turbulent heat fluxes are shown to be an important energy sink for eddy potential energy budget, balancing energy

production from the mean flow. Ma et al. (2016) show that including the effect of OME-A feedback can strengthen the Kuroshio Extension Jet in eddy-resolving coupled ocean-atmosphere model simulations. As such, resolving ocean mesoscale eddies and their interactions with the atmosphere can lead to more realistic representation of ocean fronts and currents, such as the Kuroshio and Gulf Stream, which may have impacts on model forecast skills of weather and climate variability on subseasonal-to-decadal time scales.

1.2 Motivations and Objectives

Motivated by previous studies, the objectives of this dissertation research is to further advance our understanding of OME-A interactions by focusing on two sets of questions:

1) To what extent can ocean mesoscale eddies affect precipitation? Can the newly available satellite rainfall measurements improve the robustness of observed rainfall response to mesoscale eddies? Do these observed rainfall responses provide support to previous modeling results that ocean mesoscale eddies are important in maintaining moisture budget in the marine boundary layer?

2) How important are eddy-induced SST anomalies in affecting wind work input into the ocean eddies? How does the SST feedback on the wind work affect the previous estimate of the eddy wind work due to ocean current feedback? What the underlying mechanism for the SST feedback on the eddy wind work?

1.2.1 Motivations and objectives of Chapter 2

Chapter 2 will be devoted to address the first set of questions. As discussed in section 1.1, atmospheric response to ocean mesoscale eddies is not limited to the surface winds, but also detectable in cloud fraction, water vapor, rainfall, turbulent heat flux and boundary layer height. Among these various forms of atmospheric response to ocean eddies, the rainfall response is the most difficult to quantify and subject to considerable uncertainty (e.g. Arkin and Xie 1994; Joyce et al. 2004; Ebert et al. 2007). Thus, examining and comparing eddy-induced rainfall from multiple satellite-based rainfall products are highly desirable. Because precipitation is an integrated measure of convective processes in the atmosphere and provides an important metric for validating global and regional climate models, it motivates us to develop an accurate quantification of rainfall response to ocean mesoscale SST forcing.

In Chapter 2, the robustness of the rainfall response will be examined by comparing three different satellite derived rainfall datasets: the Tropical Rainfall Measurement Mission (TRMM) Multi-satellite Precipitation Analysis (TMPA), NOAA Climate Prediction Center (CPC) Morphing Technique (CMORPH) global precipitation and newly available Integrated Multi-satellitE Retrievals for Global Precipitation Measurement (IMERG) that is based on the latest remote sensing technology with finer spatial and temporal resolution. We will attempt to address the first set of questions by comparing the rainfall responses from these three observational datasets. This will allow

us to gain further understanding of the role of ocean eddies in forcing atmospheric circulation and climate at both local and basin-scales.

1.2.2 Motivations and objectives of Chapter 3

Chapter 3 will be devoted to address the second set of questions. As mentioned before, mesoscale eddies dominate the ocean kinetic energy, and OME-A interaction is shown to be fundamental for the dynamics of energetic western boundary currents. However, physical processes governing eddy energy budget have not been well studied. Although previous studies have examined the influence of OME-A interaction on wind speed and wind stress, our present understanding of how the OME-A interaction affects the eddy wind power, which is an important energy sink for eddy kinetic energy, is limited.

In Chapter 3, we will focus on eddy wind power. In particular, we will explore how eddy wind power is affected by SST feedback on surface winds through a scaling analysis and a set of high-resolution coupled model simulations. We will attempt to address the second set of questions by analyzing and comparing high-resolution coupled model simulations with and without OME-A interaction.

CHAPTER II

SATELLITE OBSERVED PRECIPITATION RESPONSE TO OCEAN MESOSCALE EDDIES[*]

2.1 Introduction

Ocean mesoscale eddies can make a significant contribution to SST variability along western boundary current regimes, such as the Kuroshio Extension (e.g. Ma et al. 2016), where eddies are energetic and frontal-mesoscale air-sea interactions are intense. Over the past decade, noteworthy progress in satellite measurements has produced a suite of high-resolution observations that allow for the identification of active coupling between ocean mesoscale eddies and atmosphere (OME-A) (Chelton et al. 2004; Xie 2004; Small et al. 2008; Bryan et al. 2010; Chelton and Xie 2010; O'Neill et al. 2010; 2012; Frenger et al. 2013; Ma et al. 2016). One clear manifestation of this ocean-atmosphere coupling is the remarkable positive correlation between mesoscale SST and wind speed over major ocean fronts, such as the Gulf Stream, Kuroshio, Agulhas Return Current and Brazil-Malvinas Confluence (Chelton et al. 2004; Park et al. 2006; O'Neill et al. 2005; Tokinaga et al. 2005; Bryan et al. 2010; O'Neill et al. 2010; 2012). Recent studies (Frenger et al. 2013; Ma et al. 2015a; Byrne et al. 2015) further show that atmospheric

[*] Reprinted from Satellite Observed Precipitation Response to Ocean Mesoscale Eddies by Liu et al., 2018, Journal of Climate. DOI: 10.1175/JCLI-D-17-0668.1. Copyright [2018] by ©American Meteorological Society. Used with permission.

response to eddy-induced SST is not limited to surface wind speed but also quantifiable in satellite-derived cloud fraction, cloud liquid water, water vapor and rainfall.

However, it is well known that satellite-based measurements, particularly rainfall estimates, are subject to considerable uncertainty (e.g. Arkin and Xie 1994; Joyce et al. 2004; Ebert et al. 2007). The previously identified eddy-induced precipitation response is based on rainfall products using single-sensor algorithms. For example, Frenger et al. (2013) and Byrne et al. (2015) used the rainfall measurement from the Advanced Microwave Scanning Radiometer-Earth Observing System (AMSR-E) (microwave radiometer) to identify eddy-induced rainfall response in the Southern Oceans. Ma et al. (2015a) applied the Tropical Rainfall Measurement Mission (TRMM) Microwave Imager (TMI) rain rate to study rainfall response to eddy-induced SST variability along the Kuroshio Extension region. To the best of our knowledge, there are no published studies that have attempted to examine and compare eddy-induced rainfall using multiple satellite-based rainfall products, although many efforts have been made to compare satellite-derived precipitation estimates and their algorithms (e.g. Adler et al. 2001; Ebert et al. 2007).

Different satellite-measured products have different measurement accuracy, sampling frequency and associated algorithms that can lead to different biases and measurement errors as well as sampling uncertainties (e.g. Arkin and Xie 1994; Alder et al. 2001; Joyce et al. 2004). Due to the limited *in situ* rainfall measurements over the open ocean, validating global satellite rainfall products over the oceans remains a

challenge (Adler et al. 2001). Kidd et al. (2003), however, show that precipitation estimates using a multi-sensor algorithm are generally more accurate than using a single sensor technique. The newly available Integrated Multi-satellitE Retrievals for Global Precipitation Measurement (IMERG) is based on a multi-sensor algorithm. It also has much improved spatial and temporal resolution over the previous products. Therefore, it is logical to hypothesize that IMERG is more suited for quantifying rainfall response to ocean eddies, which is characterized by small spatial scales and weak amplitude. The prime objective of this study is to test this hypothesis by comparing eddy-induced rainfall responses derived from IMERG and from other previous satellite-based rainfall measurements.

Understanding the effects of ocean mesoscale eddies on precipitation is vital to the understanding of frontal-mesoscale air-sea interaction, because precipitation is an integrated measure of convective processes in the atmosphere and provides an important metric for validating global and regional climate models. In this study, following Frenger et al. (2013), we will perform composite analysis of precipitation derived from three different rainfall datasets, including Tropical Rainfall Measurement Mission (TRMM) Multi-satellite Precipitation Analysis (TMPA) 3B42 dataset (Huffman et al. 2007; 2010), NOAA Climate Prediction Center (CPC) Morphing Technique (CMORPH) global precipitation dataset (Joyce et al. 2004) and IMERG (Hou et al. 2014; Huffman et al. 2015b, c, d). The comparative analysis will be focused on eddy-active regions over the global ocean, encompassing the Kuroshio Extension, the Gulf Stream, the Agulhas

Current Retroflection and the Brazil-Malvinas Confluence (4 boxes in Fig. 2.1). The very same regions were also chosen by O'Neill et al. (2010; 2012) to analyze mesoscale air-sea interactions. We identify these four areas as the eddy-active regions based on the standard deviation maps of Sea Level Anomaly (SLA) (not shown). In addition to the comparison of general characteristics of eddy-induced rainfall response among these three different rainfall datasets, we will examine how the rainfall response differs between summer and winter and whether the response is symmetric between cold and warm eddies.

The Chapter 2 is organized as follows. Section 2.2 describes the datasets and analysis methods used in the study. Section 2.3 and 2.4 present the results and discussions. Section 2.5 gives a summary of the major findings and discusses their implications.

2.2 Data and Method

2.2.1. Satellite Precipitation Datasets

As introduced above, three satellite-derived precipitation datasets are used in this study: the Tropical Rainfall Measurement Mission (TRMM) Multi-satellite Precipitation Analysis (TMPA), NOAA Climate Prediction Center (CPC) Morphing Technique (CMORPH) and newly available Integrated Multi-satellitE Retrievals for Global Precipitation Measurement (IMERG). TMPA provides a quasi-global precipitation estimate consisting of both real-time (RT) and post-real-time (i.e., research) products

with different temporal resolutions: 3 hourly (3B42), daily (3B42 derived) and monthly (3B43). Since ocean eddies are identified using the daily merged Maps of SLA, from Archiving, Validation, and Interpretation of Satellite Oceanographic data (AVISO) (Picot et al. 2003) (described later in Section 2.2.2), here the TMPA 3B42 daily product, which is a multisatellite-gauge combination, is used. It is derived based on the TRMM Combined Instrument (TCI) calibration dataset that integrates microwave measurements from TRMM Microwave Imager (TMI), Advanced Microwave Scanning Radiometer for Earth Observing Systems (AMSR-E), Special Sensor Microwave Imager (SSMI), Special Sensor Microwave Imager/Sounder (SSMIS), Advanced Microwave Sounding Unit (AMSU), Microwave Humidity Sounder (MHS) with microwave-adjusted merged geo-infrared (IR) estimates and monthly accumulated rain gauge analysis from Global Precipitation Climatology Centre (GPCC) (Huffman et al. 2007; 2010; 2015a). The daily mean 3B42 product has a spatial resolution of 0.25^{o} x 0.25^{o} over 50^{o}N-50^{o}S from 1998 to present.

The CMORPH dataset is derived using a morphing technique in which, instead of simply averaging microwave measurements or blending microwave and IR estimates, half-hourly low-orbiter satellite microwave derived rainfall estimates are propagated by motion vectors estimated from IR-derived cloud properties (Joyce et al. 2004). Similar to TMPA 3B42, CMORPH is based on the passive microwave measurements from SSMI aboard the United States DMSP F-13, -14, and -15 satellites, AMSU aboard United States NOAA-15 and -16 satellites and TMI aboard TRMM spacecraft. It has a temporal

resolution of 3 hours and spatial resolution of 0.25^{o}x0.25^{o} over 60^{o}N to 60^{o}S and is available from January 1998 to present.

Finally, the new IMERG product unifies precipitation from a satellite constellation with the Global Precipitation Measurement (GPM) mission – a TRMM follow-on mission with significantly improved spatial resolution and coverage (Hou et al. 2014). The core observatory satellite of GPM consists of a Dual-Frequency Precipitation Radar (DPR) and GPM Microwave Imager (GMI). The dual-band precipitation radar on board the GPM satellite provides a better estimate of the sizes of precipitation particles and a wider range of precipitation rates than the single-band radar on board the TRMM satellite. The number of microwave channels is also significantly increased from five in the TMI to thirteen in the GMI, resulting in better resolution and more reliable calibration. As a result, GPM rainfall dataset has not only a finer spatial resolution of 0.1^{o}x0.1^{o}, but also a wider range of precipitation types, including light-intensity rainfall and snowfall, than TRMM rainfall. IMERG uses more passive microwave sensors than TMPA (Huffman et al. 2015b, c, d) leading to significant changes in passive microwave rainfall estimates (Liu 2016). IMERG algorithm (Huffman et al. 2015b, c, d) integrates multisatellite retrievals from TMPA, CMORPH and Precipitation Estimation from Remotely Sensed Information using Artificial Neural Networks-Cloud Classification System (PERSIANN-CCS). And the rain gauge analysis used is the same with TMPA from Global Precipitation Climatology Centre (GPCC). It contains monthly and half-hourly datasets from final run (latency ~2.5month after the month), early run (5 hours after

observation time) and late run (15 hours after observation time). Here Day 1 IMERG final run product derived from multi-satellites and gauges is used to compare with TMPA 3B42 and CMORPH. It is available from 12th March 2014 to the present with a half-hour temporal resolution.

We choose the overlapping time span of these three satellite-derived datasets from April 2014 to January 2016 to perform the comparative analysis. To test whether such a short period can provide statistically reliable results, we first analyzed and compared precipitation from TMPA 3B42 and CMORPH for the long period (in the Appendix) from April 2003 to March 2014 and the short period between April 2014 and January 2016. These analyses and comparisons were also carried out separately for summer and winter. The results show that the rainfall responses derived from TMPA 3B42 and CMOPRH and their differences are very similar between the long and short period. This gives us the confidence that the short overlapping period is suitable for analyzing and comparing three different rainfall datasets.

2.2.2 Eddy Identification

The daily merged Maps of SLA, from Archiving, Validation, and Interpretation of Satellite Oceanographic data (AVISO) (Picot et al. 2003) on a uniform 0.25°x0.25° grid from April 2003 to January 2016, were used to identify ocean mesoscale eddies. Following Kurian et al. (2011), we tracked eddies of effective radius, defined as the radius of a circle with the same area of the outmost closed SLA contour, between 45km

and 150km in the four eddy-active regions indicated in Fig. 2.1, i.e., the Kuroshio Extension, the Gulf Stream, the Agulhas Current Retroflection and the Brazil-Malvinas Confluence, based on closed SLA contours from daily maps. To minimize the uncertainties in the eddy detection process, we compared the detection results against visual identification before performing composite analysis. The identified eddies are primarily isolated ones. However, this still does not exclude the possibility that a small amount of identified eddies are bonus eddies that are filaments and transient meanders. Daily 9 km merged Microwave and Infrared (MW-IR) OI SST during the same period was used to compute SST anomalies (SSTAs) corresponding to each identified eddy. Here the eddy SSTA is defined as area-averaged SST over 1.5 eddy-radius area minus averaged SST value over an annulus between 2.5 and 1.5 eddy-radii. Using SSTA and SLA, identified eddies were grouped into warm-core anticyclonic and cold-core cyclonic rings. Since active coupling between the atmosphere and eddies occurs through SST, an SST threshold was applied to select a subset of the eddies that retain sufficiently strong SST anomalies to have an effect on the atmosphere: for each identified eddy we first computed the difference between the maximum and minimum SST within a 300km x 300km box aligned with the eddy center and then selected those eddies where the SST difference is larger than 2°C. With such restrict eddy detection criterion, a total of ~1,126,600 eddy snapshots were identified from the daily SLA and SST maps in the four eddy-active regions, and a subset of ~165,000 snapshots that coincide with the rainfall

observation periods were used in the composite analysis of eddy-induced rainfall response.

2.2.3 Rainfall Composite

The composite analysis follows closely that of Frenger et al. (2013). Here we highlight a few key aspects of the analysis. For each identified eddy snapshot corresponding daily precipitation within a box of 500km x 500km aligned to the eddy center was generated. Since eddies vary considerably in size, we normalized each identified eddy and its rainfall response by eddy's radius, R. To minimize the influence from background field, we computed SST and rainfall response anomalies for each eddy by subtracting a background value surrounding the eddy from its SST and rainfall response. As noted above, the background value for SST was computed by averaging SST over an annulus of inner radius of 1.5 R and outer radius of 2.5R as the SST anomaly associated with ocean eddies normally extends to 1.5 radii. For rainfall, the same annulus of inner radius of 1.5R and outer radius of 2.5R was used to compute the background value as rainfall response over each individual eddy is noisier and not always restricted within one eddy radius. We then rotated each eddy to a common westerly background wind direction, which is defined by the direction of the area mean wind over 14 radii of the eddy, in order to distinguish the downstream and upstream responses (Frenger et al. 2013). Finally, SST and rainfall anomaly composites were made over all warm and cold eddies. Both ERA-interim daily winds at 10 meter and the

Cross-Calibrated Multi-Platform (CCMP) Version 2 gridded daily surface winds were used to calculate the background wind direction. Because these wind products are only used to calculate the averaged wind direction over a large background area for rotating the variables, the results show little differences between them. The rainfall responses using TMPA 3B42 and CMORPH during the 11-year period from April 2003 to March 2014 were first analyzed based on the composite of ~ 961,600 identified eddy daily snapshots in the four ocean frontal regions. These results were compared to the responses for the short period from April 2014 to January 2016, which contains roughly 165,000 eddy daily snapshots, to test the robustness of the finding before further comparisons were made to IMERG rainfall response.

2.3 Overall Rainfall Characteristics

2.3.1 Satellite Observation

All three rainfall products exhibit an overall similar pattern of global mean precipitation (Fig. 2.1) characterized by the enhanced rainfall bands over the tropics and along major ocean frontal zones in the extratropics. In general, over the ocean, TMPA 3B42 and CMORPH mean rainfalls are in more agreement than that of IMERG, which is not surprising because TMPA 3B42 and CMORPH share, more or less, the same source of raw passive microwave measurements. However, there are some major discrepancies even between TMPA 3B42 and CMORPH. For example, CMORPH tends to have higher rainfall values over Kuroshio Extension and Brazil-Malvinas Confluence than TMPA

3B42, but lower values over the Gulf Stream. These differences do not depend on the analysis period. In fact, the same differences are found between TMPA 3B42 and CMORPH in the 11-year mean precipitation (Fig. 2.2). Among the three rainfall datasets, IMERG gives the lowest mean rainfall value (Fig. 2.1c) over the major oceanic precipitation regions, such as the tropics and the frontal zones. This finding is consistent with Liu (2016) who attributed the lower rainfall estimates in IMERG to changes in the passive microwave algorithms. IMERG employs more passive microwave sensors compared to TMPA, which can lead to significant changes in passive microwave rainfall estimates (Huffman et al. 2015c). Further analyses of monthly microwave and IR data indeed show that the significant differences between IMERG and TMPA are mainly caused by the different microwave products (Liu, 2016). Among our four target areas, the most significant reduced rainfall estimates in IMERG occur over the Gulf Stream region, which can also be seen from Liu (2016). The lower rainfall estimate in IMERG holds for both annual mean and monthly mean patterns (not shown).

2.3.2 Validation against in situ measurement

Recent studies (Tang et al. 2016; Prakash et al. 2016; He et al. 2016; Xu et al. 2017) suggest that IMERG is superior to TMPA in estimating precipitation over mainland China, India, the upper Mekong River basin and southern Tibetan Plateau based on *in situ* rain gauge measurements. However, due to the lack of *in situ* measurements, it is difficult to validate satellite rainfall observations over the open ocean, especially in extratropical

ocean frontal regions. The only one buoy we could find that was located in an extratropical ocean frontal region and also overlapped the three satellite rainfall products was the NOAA's Ocean Climate Stations Project (OCS) Kuroshio Extension Observatory (KEO) surface mooring, which is located at 32.3^{o}N, 144.6^{o}E. We validated the satellite rainfall products against this *in situ* measurement. The validation method follows Serra et al. (2003). We used the averaged values of satellite measured rainfall over a varying area ranging from 0.1^{o} x 0.1^{o} to 5^{o} x 5^{o} square box centered on the KEO location to calculate rainfall statistics. Our analysis shows that the differences between KEO measurements and IMERG daily data are the smallest among the three satellite rainfall datasets (Fig. 2.3), which gives us the confidence that IMERG is more accurate in estimating mean precipitation over this region. The discrepancies in mean rainfall estimates raise an interesting and important question not addressed by previous studies: Do the lower mean rainfall values in IMERG translate to weaker rainfall response to ocean eddies in IMERG than in the other datasets? We address this key question of our study in the section 2.4.

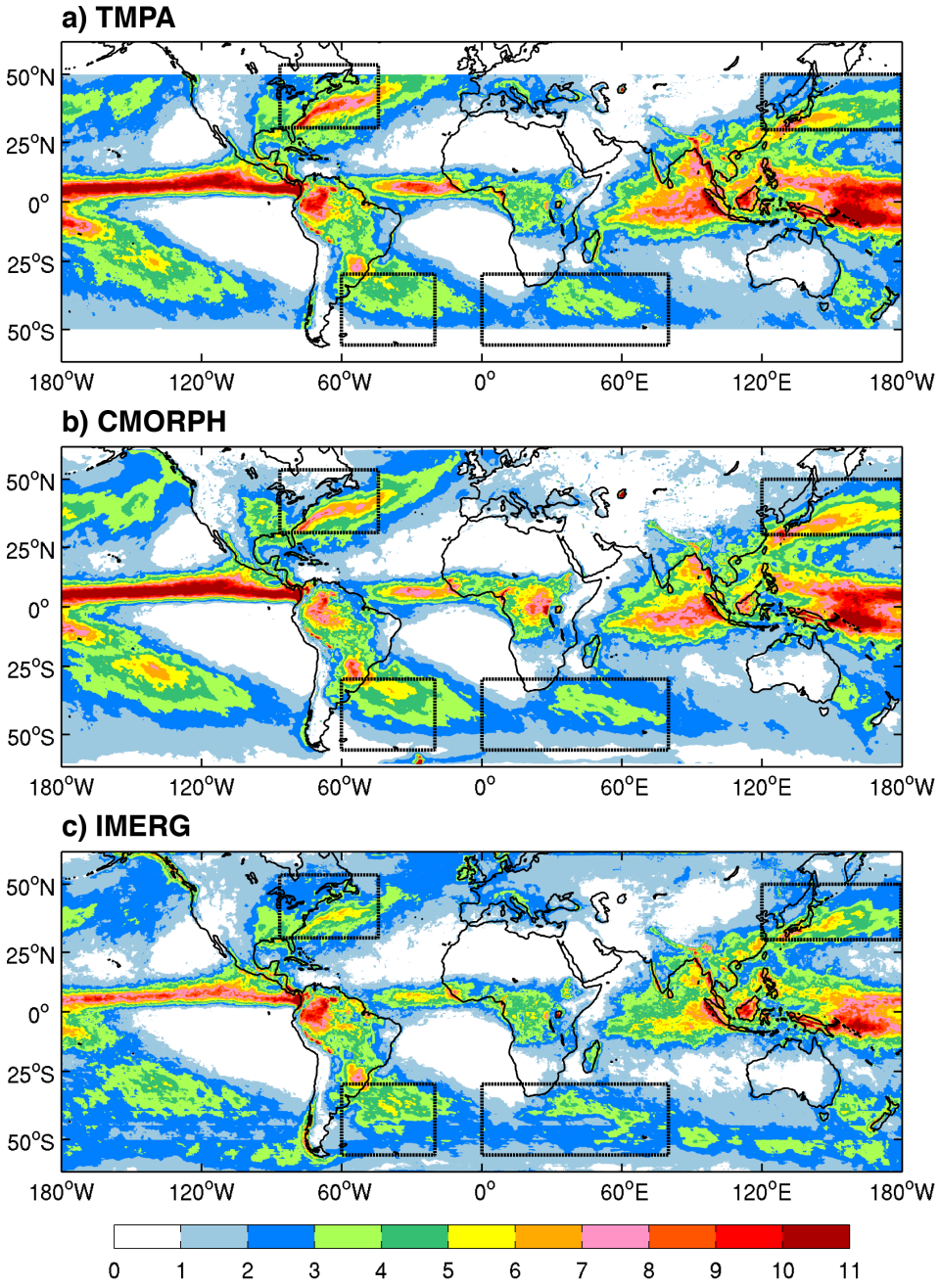

FIG. 2.1. April 2014 – Jan 2016 mean rainfall derived from daily mean precipitation data (mm day^{-1}) of a) TMPA 3B42, b) CMORPH and c) IMERG. Black dash boxes mark the regions where eddy-induced rainfall response is analyzed.

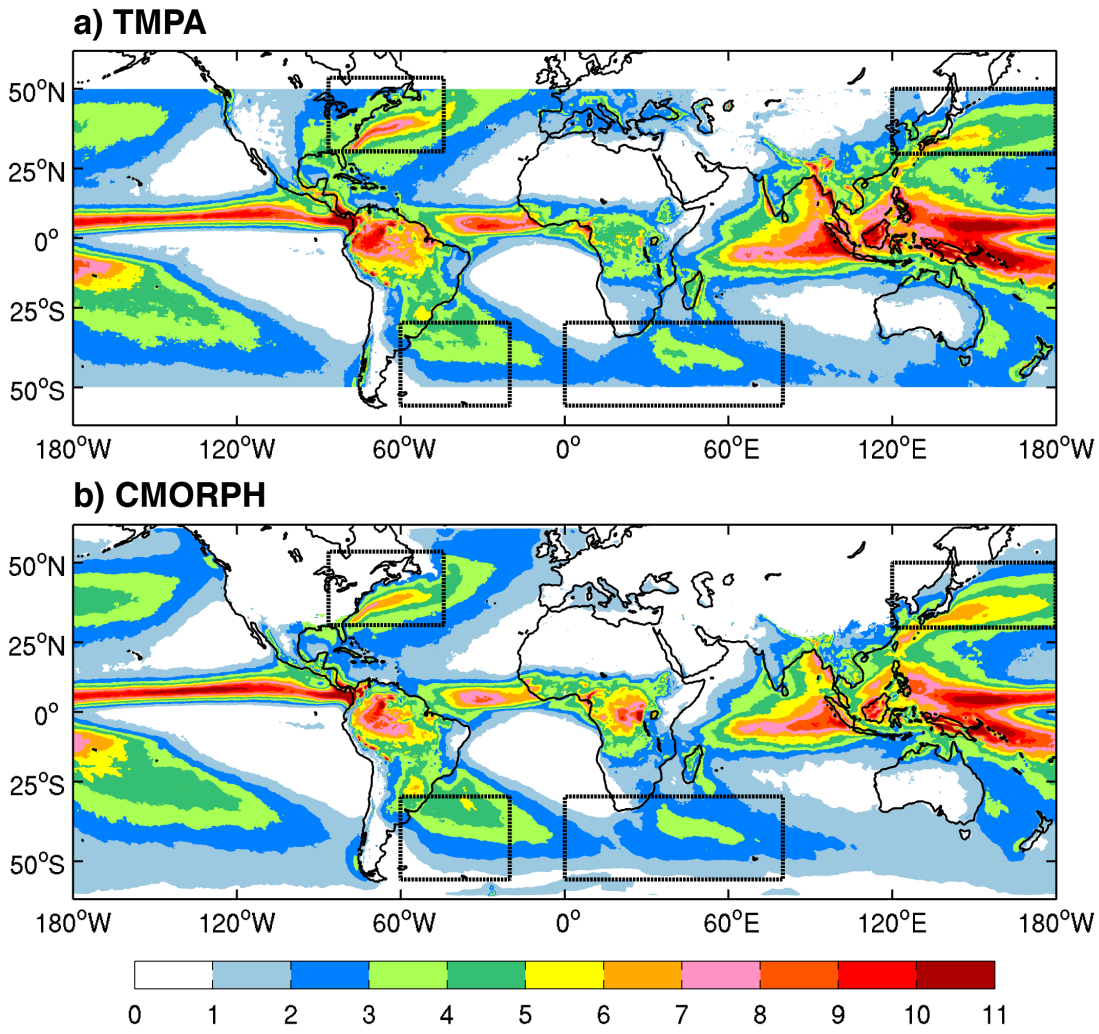

FIG. 2.2. 11-year mean rainfall (mm day^{-1}) computed from daily mean a) TMPA 3B42 and b) CMORPH data. Black dash boxes mark the regions where eddies are identified and tracked for analyzing eddy-induced rainfall response.

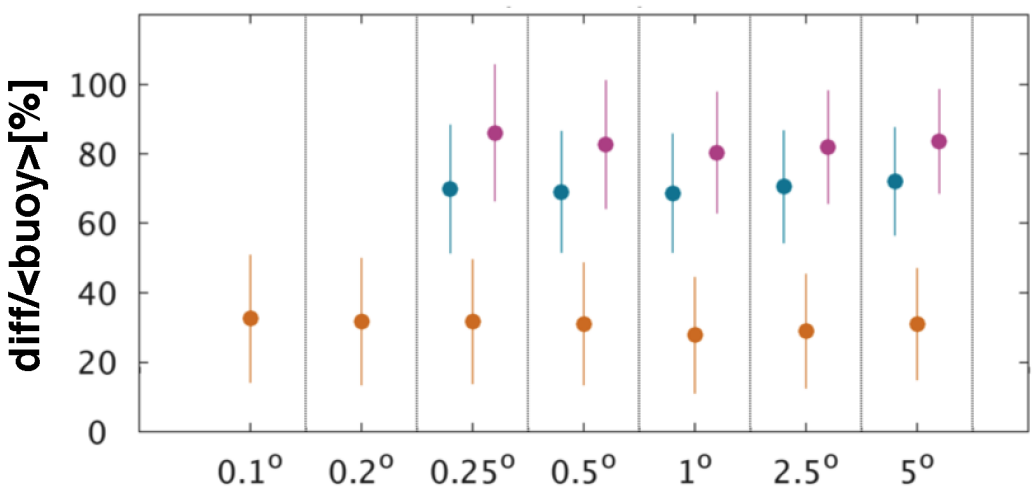

FIG. 2.3. Relative differences of daily mean rainfall between TMPA and KEO buoy (cyan), between IMERG and KEO buoy (orange), between CMORPH and KEO buoy (magenta) in reference to the KEO buoy mean rainfall. Satellite rainfall values are derived by averaging over various square boxes centered on the KEO buoy location whose dimension ranges from 0.1° to 5° as shown in x-axis. The dots show mean values of the relative difference and the vertical bars show 95% confidence intervals.

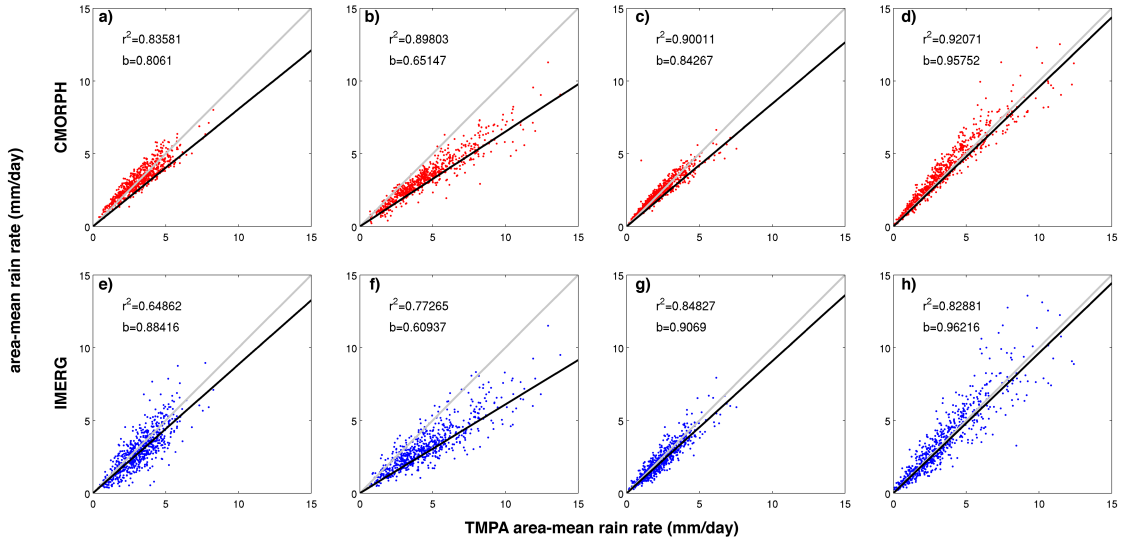

FIG. 2.4. Scatterplots of CMORPH (upper panel) and IMERG (lower panel) versus TMPA 3B42 area-averaged daily mean rain rates from April 2014 to January 2016 for Kuroshio Extension (a, e), Gulf Stream (b, f), Agulhas Current retroflection (c, g) and Brazil-Malvinas confluence (d, h). The grey diagonal line in each plot indicates the one-to-one relationship and the black line is the least square linear fit. Legends in each plot show r2 and the slope of the linear fit b.

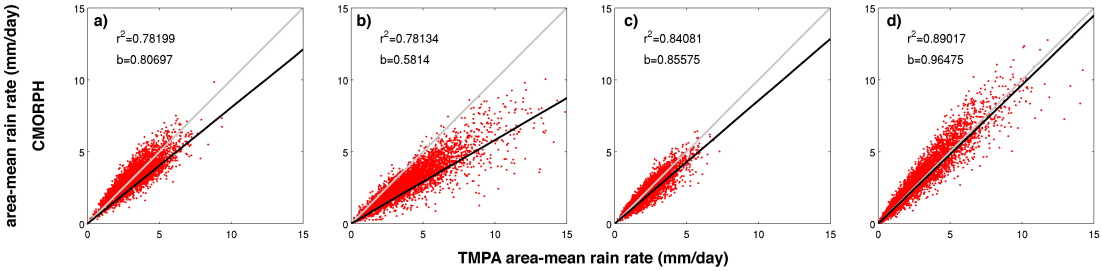

FIG. 2.5. Scatterplots of 11-year CMORPH versus TMPA 3B42 area-averaged daily mean rainfall over a) Kuroshio Extension, b) Gulf Stream, c) Agulhas Current retroflection and d) Brazil-Malvinas confluence. The grey diagonal line in each plot indicates the one-to-one relationship and the black line is the least square linear fit. Legends in each plot show r2 and the slope of the linear fit b.

2.3.3 Systematic Differences among the Three Satellite Observations

Although lower mean values always prevail in IMERG than TMPA over the ocean, the systematic differences between TMPA and IMERG vary from region to region. As shown in Fig. 2.4, more significant differences occur over the Kuroshio Extension and Gulf Stream, and relatively small discrepancies occur over the Agulhas Current Retroflection and Brazil-Malvinas Confluence. Regression analysis yields regression coefficients of 0.81 and 0.65 between CMORPH and TMPA 3B42 over the Kuroshio Extension and Gulf Stream regions, respectively, while the corresponding coefficients between IMERG and TMPA 3B42 are 0.88 and 0.61, indicating that the rainfall rate in TMPA 3B42 is systematically higher than that in CMORPH and IMERG in these two regions. Over the Agulhas Current Retroflection and Brazil-Malvinas Confluence, the rainfall rate is also systematically higher in TMPA 3B42 than CMORPH and IMERG but the difference is less than 16%. These systematic differences between CMORPH and

TMPA 3B42 over the four target regions remain unchanged for the 11-year area-mean daily precipitation (Fig. 2.5), again pointing to the robustness of the results regardless of the time span considered. A comparison of rainfall probability density function (PDF) shows that TMPA tends to estimate more extreme rainfall than IMERG and CMORPH globally (not shown). Similar results hold for each individual frontal zone (not shown). At the KEO location, PDF analysis (Fig. 2.6) shows that TMPA and CMORPH rainfall estimates are biased low at low rain rates and high at high rain rates, while IMERG estimates always retain a better agreement with KEO measurements, indicating that the IMERG is more accurate in estimating not only the mean rainfall, but also the rainfall distribution.

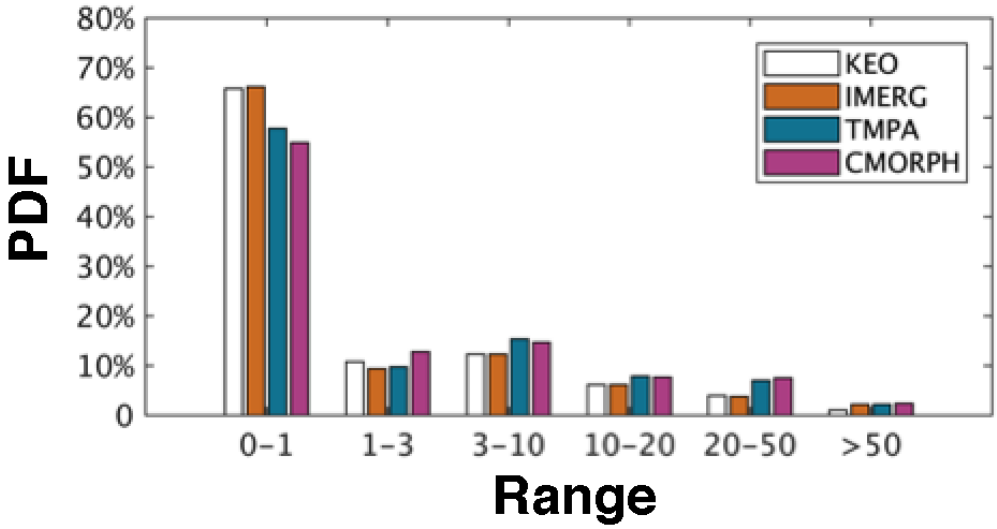

FIG. 2.6. Probability Density Function (PDF) of daily rainfall from KEO buoy (white), TMPA 3B42 (cyan), IMERG (orange) and CMORPH (magenta). The unit of x-axis is mm day^{-1} $grid^{-1}$.

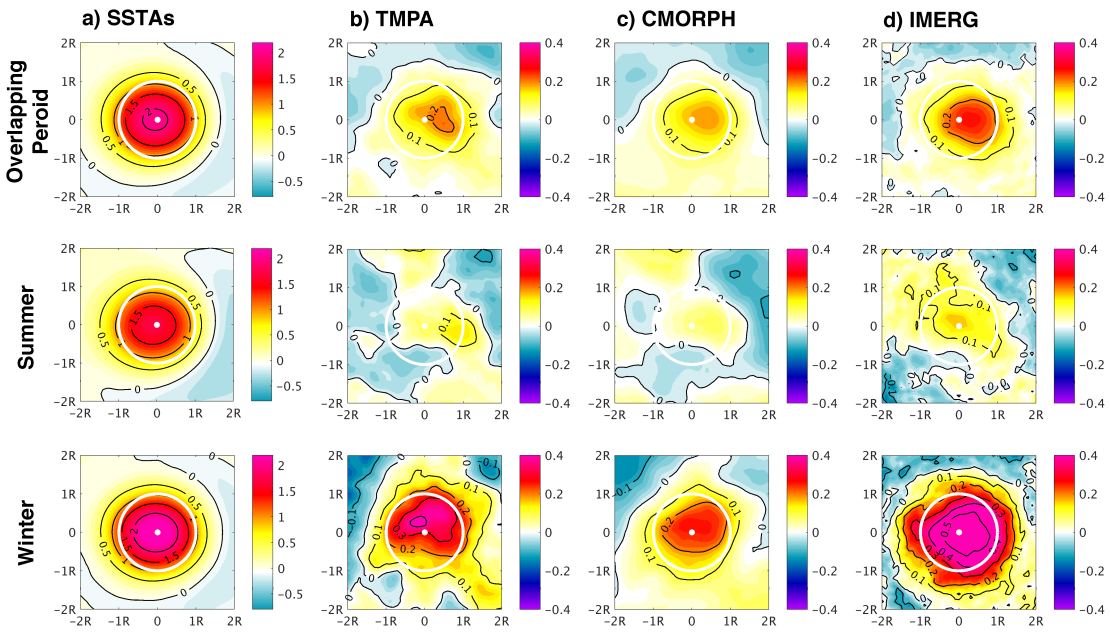

FIG. 2.7. Composite of normalized warm-core anticyclonic eddies minus cold-core cyclonic eddies for a) SSTAs (contours and color, °C), b) precipitation anomaly derived from TMPA 3B42 (contour and color, mm day^{-1}), c) precipitation anomaly derived from CMORPH (contour and color, mm day^{-1}), d) precipitation anomaly derived from IMERG (contour and color, mm day^{-1}) during the overlapping period (upper panel). Summer and winter composites are shown in middle and lower panel, respectively. White contour and dot in each panel mark one eddy radius and eddy center.

2.4 Response to Ocean Mesoscale Eddies

2.4.1 Response Differences among the Three Satellite Observations

Because of the concern that IMERG record is rather short and the sample size may not be sufficiently large to distinguish the difference of rainfall responses among different rainfall datasets, we use warm-core anticyclonic eddies minus cold-core cyclonic eddies composite to enhance the signal of rainfall response to ocean eddies by combining the sample sizes of both warm and cold eddies and to reduce background rainfall influence. However, the conclusions of the study will not change if the composite is done separately

for warm and cold eddies, as will be shown below. The upper panel of Fig. 2.7 shows composite SST and rainfall differences over all the detected anticyclonic warm eddy snapshots (~79,700) minus the composite of all the cyclonic cold eddy snapshots (~85,500) from April 2014 to Jan 2016. The composite SST is monopolar with structure similar to the composite SSH. As noted by Gaube et al. (2015), whether eddy SST has a monopolar or dipolar structure depends on eddy amplitude. For small-amplitude eddies, SST tends to have a dipolar structure because of advection of background SST by eddy currents. However, as eddy strength increases, the composite SST emerges more towards a monopole due to the increase of the rotational velocity and nonlinearity. In our target regions, large-amplitude eddies dominate mesoscale SSH variability, and therefore SST over ocean eddies tends to be monopolar rather than dipolar. Additionally, Gaube et al. (2015) show that to better illustrate the dipole SST structure, the composite needs to be calculated using a rotated coordinate that is along the orientation of the large-scale SST gradient. Otherwise, the dipole structure will be blurred due to the temporal and geographical variability in the SST gradient direction (Gaube et al. 2015). In our study, the composite is computed in a rotated coordinate determined by the large-scale winds, rather than SST gradient, to distinguish the up- and down-stream atmospheric response. All these differences can contribute to the monopolar structure of the composite SST in our study, which is consistent with other previous studies using similar rotated coordinate and in the same eddy active regions (Park et al. 2006; Ma et al. 2015a; Frenger et al. 2013). The composite warm-cold eddy SST difference shows a maximum value of about

1.8°C near the eddy center (Fig. 2.7a) and there is a corresponding anomalous positive rainfall composite in all three datasets. Remarkably, even though IMERG gives the weakest mean rainfall value in the regions, it reveals the strongest and most coherent rainfall response to ocean eddies (Fig. 2.7b-d). This result holds for each individual target region. Between the two low-resolution rainfall datasets, CMORPH gives even weaker rainfall response to eddy-induced SSTAs than TMPA – a result that again shows little dependence on the time span of the analysis (Fig. 2.8). Taken together, these findings clearly indicate that there is no relationship between mean rainfall and eddy-induced rainfall response.

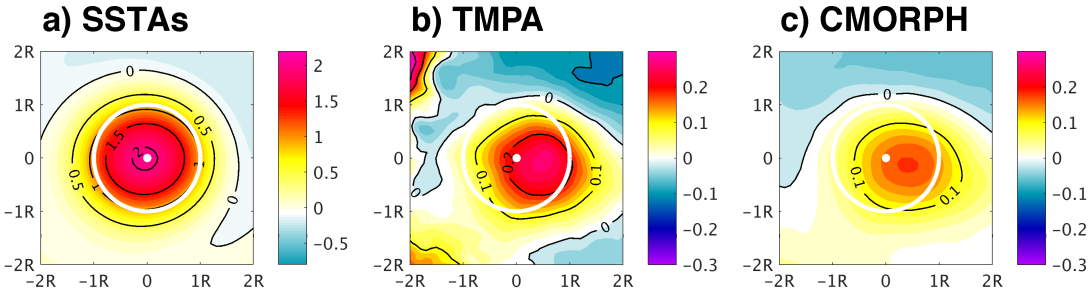

FIG. 2.8. Composite of 11-year normalized warm-core anticyclonic eddies minus cold-core cyclonic eddies for a) SSTAs (contours and color, °C), b) precipitation anomaly derived from TMPA 3B42 (contour and color, mmd^{-1}), c) precipitation anomaly derived from CMORPH (contour and color, mmd^{-1}). White contour and dot mark one eddy radius and eddy center. The composite method is the same as in Fig. 2.7.

The different rainfall responses to ocean eddies revealed by the three satellite-derived rainfall products can be caused by a number of factors, such as differences in sampling resolutions, sensor technologies and retrieval algorithms, as well as analysis techniques to combine the IR data with microwave data, and so on. The

weakest response in CMORPH may be caused by its morphing technique described in section 2.2.1. As noted by Joyce et al. (2004), CMORPH can fail to detect rainfall if it forms and dissipates over areas between the paths of passive microwave instrumentations. Therefore, if eddies are located in between the overpasses of passive microwave instrumentations, it is likely that rainfall responses are underestimated by CMORPH. TMPA and IMERG, on the other hand, are based on similar method of combining the IR data with microwave data. Some key differences between them include: 1) IMERG observes a wider range of rain type from light to heavy rainfall, thanks to the DPR on board the GPM satellite, 2) IMERG retains a much higher resolution data than TMPA because of the larger number of microwave channels in the GMI. Either one or both of these factors can lead to the differences in the inferred rainfall response to ocean eddies.

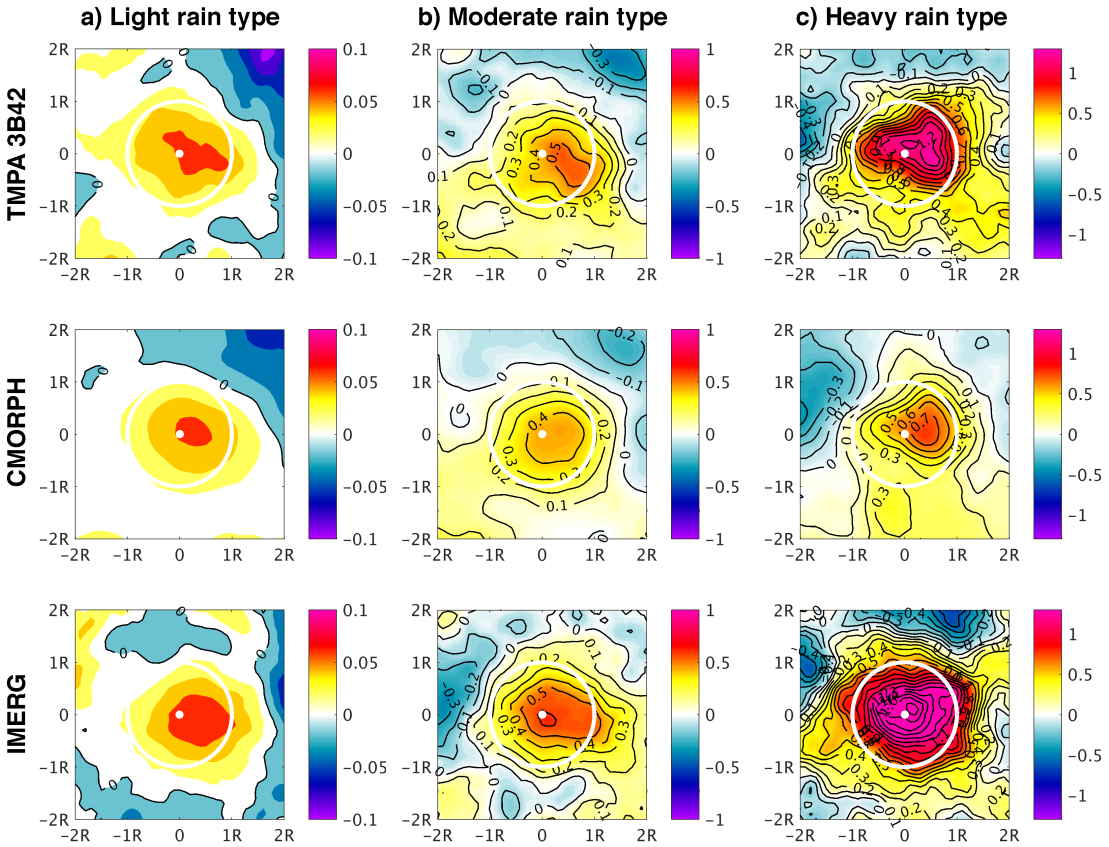

FIG. 2.9. Composite of normalized warm-core anticyclonic eddies minus cold-core cyclonic eddies for a) light rain type b) moderate rain type c) heavy rain type from TMPA 3B42 (upper panel), IMERG (middle panel), and CMORPH (lower panel) during the overlapping period. The composite method is the same as in Fig. 2.7. The black contour interval is 0.1 mmd^{-1}. Note that colorbar scales are different for light, moderate and heavy rains.

We further analyzed and compared the rainfall response of the three satellite datasets according to different rainfall types. The definition of rain types is based on averaged rainfall values over a box of 300km x 300km aligned to the eddy center. We define the value that is smaller than 3 mm day^{-1} as light rain, between 3 mm day^{-1} and 10 mm day^{-1} as moderate rain and larger than 10 mm day^{-1} as heavy rain. The result (Fig. 2.9) shows that for all three datasets the amplitude of the rainfall anomaly composite increases as

rain rate increases, consistent with the notion that OME-A interactions intensify during extratropical winter storm development over active ocean eddy regions, giving rise to stronger rainfall response to ocean eddies. Compared to TMPA and CMORPH, IMERG shows across-the-board increase in rainfall response for all rainfall types.

We computed the percentage occurrence of light, moderate and heavy rainfall over ocean eddies, which is ~75%, ~16% and ~9% for IMERG, ~72%, ~16% and ~12% for TMPA, and ~73%, ~17% and ~10% for CMORPH, respectively. The contribution of different rain types to the rainfall responses strength over ocean eddies, which is assessed based on the rainfall differences over warm eddies minus cold eddies, is ~7%, ~28% and 65% for IMERG, ~5%, ~22% and ~73% for TMPA, and ~6%, ~26% and ~68% for CMORPH, respectively. In all three datasets, heavy rainfall makes the most significant contribution to the rainfall responses over ocean eddies, even though its percentage occurrence is the lowest. As described above, between IMERG and other datasets, eddy-induced rainfall response strengths are discrepant. To address the question of which rainfall type contributes most significantly, we further computed the percentage contribution of each rainfall type to the corresponding total rainfall response discrepancies among these three datasets. Between IMERG and TMPA, the percentage contribution of light, moderate and heavy rainfall difference to the total rainfall response discrepancy between them is roughly ~ 23%, ~26% and ~51%, while these numbers are ~ 20%, ~29% and ~52% between IMERG and CMORPH. Therefore, the largest

contribution to the discrepancies in rainfall response to ocean eddies between IMERG and other two datasets appears to come from the heavy rain type.

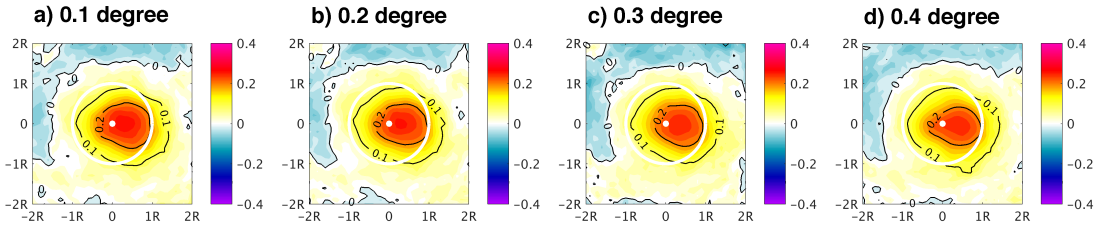

FIG. 2.10. Composite of normalized warm-core anticyclonic eddies minus cold-core cyclonic eddies for a) the original 0.1 degree IMERG (contour and color, mm day^{-1}) b) subsampled 0.2 degree, c) 0.3 degree, and d) 0.4 degree IMERG during the overlapping period. The composite method is the same as in Fig. 2.7.

We also conducted a sensitivity test to examine whether the rainfall response difference can be simply explained by the data resolution difference between IMERG and other datasets. To do so, we subsampled IMERG 0.1^{o} data onto coarser grid of 0.2^{o}, 0.3^{o} and 0.4^{o} and then repeated the rainfall response analyses. The results (Fig. 2.10) show that the response strength does decrease as spatial resolution decreases, but the changes are not nearly as large as those between IMERG and the other datasets. These results suggest that difference in data resolution alone cannot explain the difference in rainfall response to ocean eddies between IMERG and other datasets. It is more likely that the improvements in sensor technologies and retrieval algorithms play a key role in the stronger and more coherent rainfall response in IMERG than in other rainfall datasets. Further analysis and comparison of orbital products, which are beyond the scope of this

study, can provide a better understanding of the rainfall response among different datasets.

2.4.2 Response during Winter and Summer

We compare summer and winter warm-cold eddy rainfall differences composites among the three rainfall datasets during one-year period from April 2014 to March 2015. Summer is defined for the months from May to September (MJJAS) for the northern hemisphere and from November to March (NDJFM) for the southern hemisphere, while winter is defined as NDJFM for the northern hemisphere and MJJAS for the southern hemisphere, respectively. Consistent with the previous finding (Minobe et al. 2010), the global rainfall patterns from all datasets exhibit larger total rainfall amount in summer than in winter. However, rainfall response PDFs show that moderate to heavy rains (>3mm per day per grid) occur more often during winter than summer, particularly over the eddy-active frontal zones (Fig. 2.11). This is expected because most of the heavy rainfall is attributed to extratropical precipitating cyclones (Hawcroft et al. 2012) that are more intense and frequent during winter and interact strongly with underlying frontal and mesoscale SST over the ocean frontal zones.

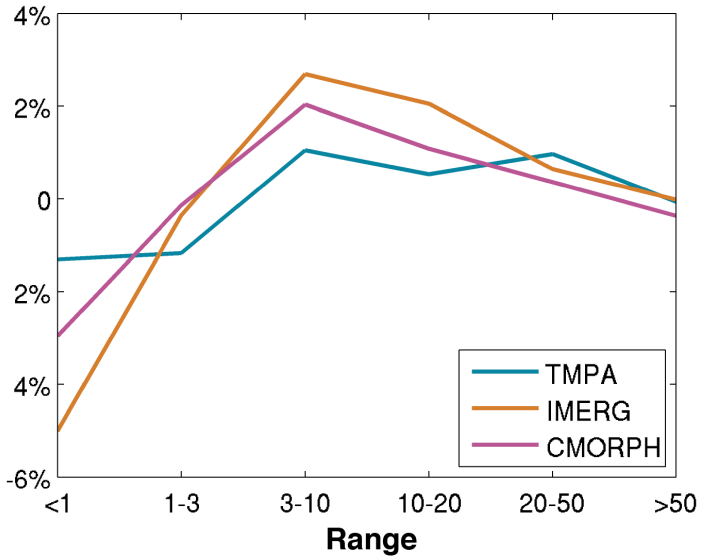

FIG. 2.11. Difference between winter and summer rainfall PDFs (winter minus summer) for TMPA 3B42 (cyan), IMERG (orange) and CMORPH (magenta) over extratropical eddy-active frontal zones. The unit of x-axis is mm day^{-1} $grid^{-1}$.

We next examined and compared rainfall responses to ocean eddies between winter and summer. The SST and precipitation difference composite maps between warm and cold eddies over the four ocean frontal zones during summer and winter are shown in the middle and lower panel of Fig. 2.7. Among the different rainfall products, the seasonal asymmetry in eddy-induced rainfall is most prominent in IMERG and least prominent in CMORPH. But common to all datasets, there is a well-defined asymmetry in rainfall response between winter and summer with stronger and more coherent response in winter than in summer. This is consistent with the notion that OME-A feedback is more active in winter than in summer (e.g. Putrasahan et al. 2013).

Part of this seasonal asymmetry in rainfall response may be related to the asymmetry in ocean-eddy induced SSTAs between summer and winter. As shown in Fig. 2.7, the winter SSTAs composite that has maximum value of ~2.1^{o}C and averaged value over one eddy radius of ~1.2^{o}C is larger than the summer composite that has maximum value of ~1.5^{o}C and averaged value over one eddy radius of ~0.9^{o}C. However, the asymmetry in the rainfall response appears to be stronger than that in the SST. To eliminate the effect of SST difference between summer and winter, we calculated the area-averaged rainfall anomaly and SSTAs for each eddy and derived the regression coefficient between them. In winter, the SST-rainfall regression coefficient is ~ 0.51mmd^{-1}/^{o}C for IMERG, ~0.34 mmd^{-1}/^{o}C for TMPA and ~ 0.27mmd^{-1}/^{o}C for CMOPRH, while in summer, the coefficient is ~ 0.26mmd^{-1}/^{o}C, ~0.24mmd^{-1}/^{o}C and ~ 0.22mmd^{-1}/^{o}C, respectively. This indicates that the rainfall response is inherently more sensitive to eddy-induced SST forcing in winter than in summer. Putrasahan et al. (2013) suggest that the seasonal sensitivity of the atmosphere to SST anomaly is associated with the vertical atmospheric stability. During winter, large averaged air-sea temperature difference contributes to a more unstable condition of the atmosphere, causing the atmosphere to be more sensitive to mesoscale SST forcing.

2.4.3 Response to Warm-Core Anticyclonic and Cold-Core Cyclonic Eddies

Convective processes in the atmosphere are highly nonlinear, and thus rainfall response to warm-core anticyclonic and cold-core cyclonic eddies may exhibit different

strength and sensitivity. We examine this issue by comparing rainfall responses to all warm and cold eddies in the four ocean frontal zones using three rainfall products. Fig. 2.12 compares the warm- vs. cold-eddy induced rainfall anomaly composite during the overlapping period. IMERG shows the most pronounced asymmetry in which rainfall anomaly is considerably stronger over warm eddies than cold eddies. Less clear asymmetry is revealed by the other two rainfall datasets, although more enhanced rainfall anomaly over warm eddies than reduced rainfall anomaly over cold eddies can still be identified. This finding is further confirmed by analyzing rainfall-SST relationship for all warm and cold eddies. Using similar regression analysis to that described in Section 2.4.2, regression coefficients between the area-averaged rainfall anomaly and SSTAs were calculated. The result shows that for IMERG the SST-rainfall regression coefficient over warm eddies is nearly twice the value (~ 0.49mmd^{-1}/^{o}C) of that (~0.26 mmd^{-1}/^{o}C) over cold eddies. For TMPA and CMORPH, the difference between the regression coefficients are smaller: the corresponding values are ~0.34mmd^{-1}/^{o}C (~0.23 mmd^{-1}/^{o}C) and ~0.23 mmd^{-1}/^{o}C (~0.20 mmd^{-1}/^{o}C) over the warm and cold eddies from TMPA (CMORPH). Note that the regression coefficients are sensitive to the definition of the anomaly, but the relative strength of the response to warm and cold eddies remains similar. These results indicate that the rainfall response is inherently more sensitive to eddy-induced warm SST anomalies. Separate analyses for warm- vs. cold-eddy induced rainfall anomaly composite in winter (Fig. 2.13) and summer (Fig. 2.14) are also performed. A seasonal asymmetry in rainfall response with stronger and more coherent response in winter than

in summer is observed for both warm and the cold eddies. However, warm eddies always tend to produce stronger rainfall response than cold eddies. Furthermore, this asymmetry in rainfall response between warm eddies and cold eddies is most prominent in IMERG no matter during summer or winter, compared to the other two datasets.

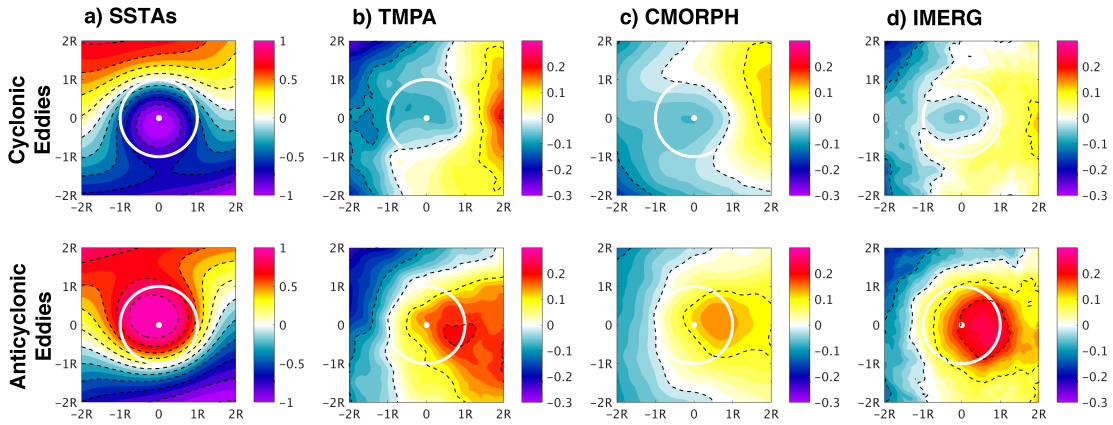

FIG. 2.12. Composite of a) SSTAs (^{o}C), b) TMPA 3B42, c) CMORPH, d) IMERG rain anomalies (mmd^{-1}) for cold-core cyclonic eddies (upper panel) and warm-core anticyclonic eddies (lower panel) during the overlapping period.

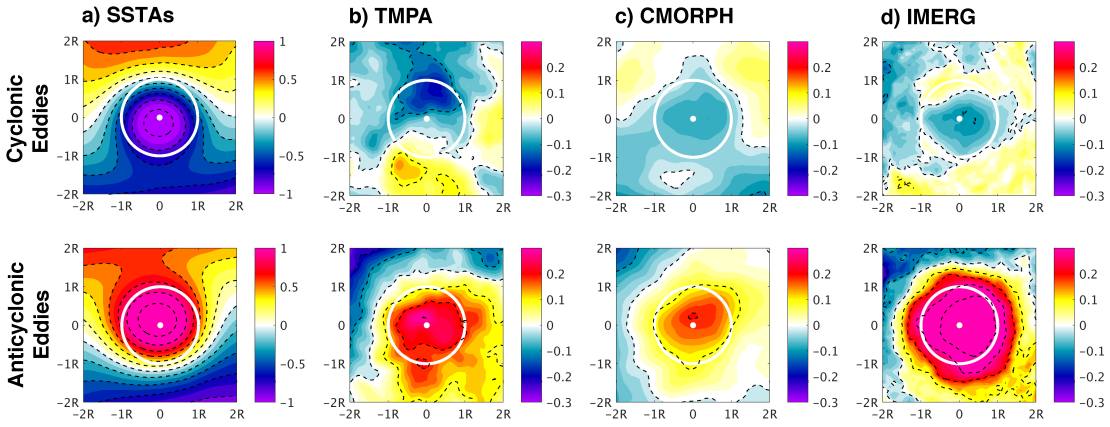

FIG. 2.13. Composite of a) SSTAs (^{o}C), b) TMPA 3B42, c) CMORPH, d) IMERG rain anomalies (mmd^{-1}) for cold-core cyclonic eddies (upper panel) and warm-core anticyclonic eddies (lower panel) during winter.

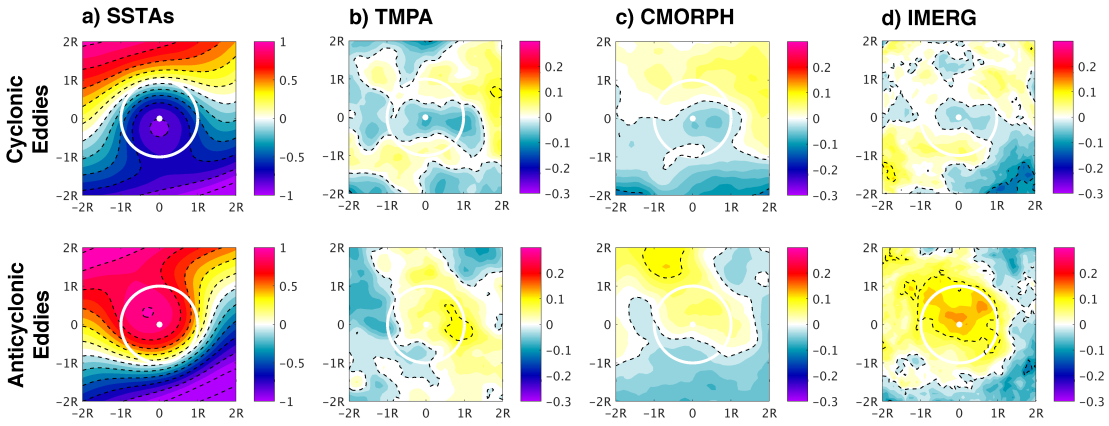

FIG. 2.14. Composite of a) SSTAs (^{o}C), b) TMPA 3B42, c) CMORPH, d) IMERG rain anomalies (mmd^{-1}) for cold-core cyclonic eddies (upper panel) and warm-core anticyclonic eddies (lower panel) during summer.

To further reveal the nonlinear relationship between eddy-induced SSTAs and rainfall response, a nonlinear function is fit to the scatter plot between SSTAs and rainfall anomalies across all eddies using IMERG product (Fig. 2.15). An increasing slope from cold to warm eddies is clearly observed, indicating that rainfall response is stronger over warm eddies than cold eddies. This is consistent with the composite and linear regression analyses performed separately for warm and cold eddies. Similar nonlinear regression analyses are performed for summer and winter, respectively (Fig. 2.16). Again in agreement with the other analyses of the study, the regression slope is larger in winter than in summer. These results reinforce the evidence that rainfall has stronger response to eddy-induced SSTs in winter and the nonlinearity between SSTAs and rainfall is stronger in winter than in summer.

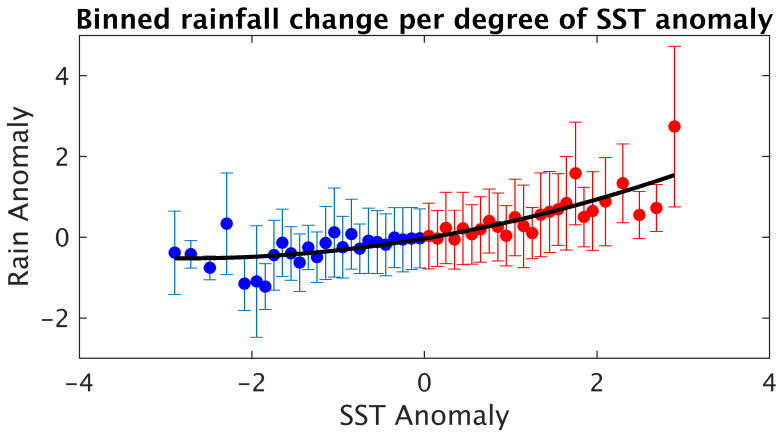

FIG. 2.15. Binned averages of IMERG rainfall anomaly over warm eddies (red scatter) and cold eddies (blue scatter). Error bar refers to standard deviation. A nonlinear fitted line (black line) shows the response strength of rainfall anomalies to SST anomalies.

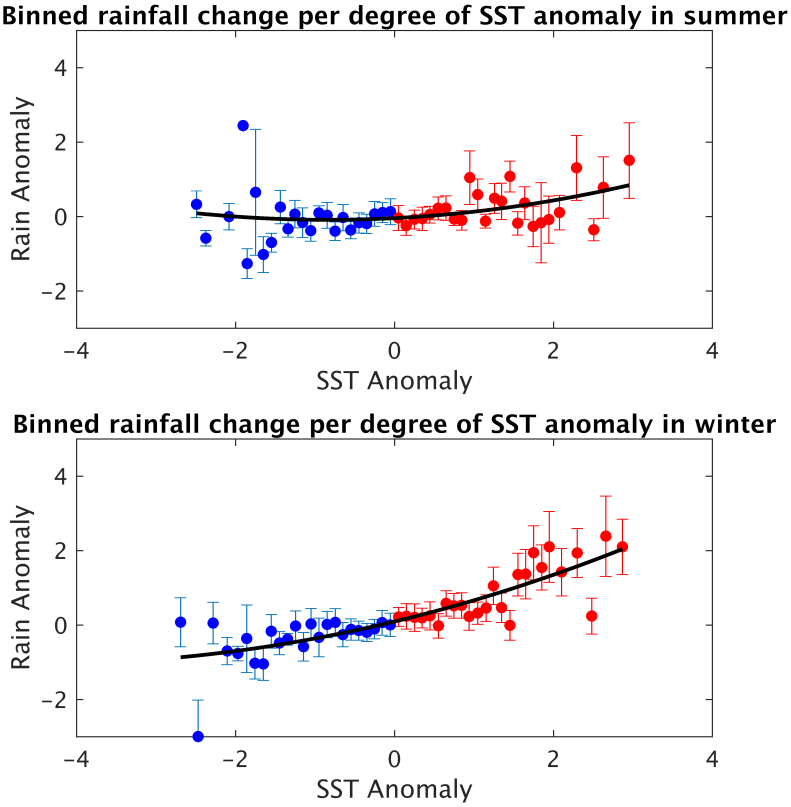

FIG. 2.16. Binned averages of IMERG rainfall anomaly over warm eddies (red scatter) and cold eddies (blue scatter) in summer (upper panel) and winter (lower panel). Error bar refers to standard deviation. A nonlinear fitted line (black line) shows the relationship between rainfall and SST anomalies across all eddies.

Documenting and understanding this asymmetry in rainfall response are important, because it has a direct bearing on the question whether ocean mesoscale eddies can have a rectified effect on the atmosphere. On average, numbers of ocean eddies are roughly evenly divided between warm anticyclones and cold cyclones. Since positive rainfall anomalies over warm eddies are generally stronger than negative rainfall anomalies over cold eddies, it suggests that eddy-induced mesoscale SST anomalies along ocean frontal zones may make a net contribution to total rainfall integrated over these regions. With the assumptions that the number of warm and cold eddies is the same and that they have about the same amplitude distributions of SSTAs values, the net contribution of the ocean eddies to the overlying rainfall is estimated to be roughly $0.23 mmd^{-1}/^{o}C$ (based on IMERG). Understanding this net effect of ocean eddies on the atmosphere may be a key to understanding the role of mesoscale SST in forcing large-scale atmospheric circulation, as demonstrated by some recent modeling studies (e.g. Ma et al. 2015b).

2.5 Discussion and Conclusion

We analyze and compare observed oceanic precipitation and its response to ocean-eddy induced mesoscale SST using three different satellite-based rainfall datasets, TMPA, IMERG and CMORPH, over the common period from April 2014 to January 2016. In spite of the short record length, we are able to obtain statistically robust findings using composite analyses over 165,000 ocean mesoscale eddy snapshots that are identified and traced using satellite altimetry in four most eddy-energetic regions of the

ocean. The finding shows agreement among the datasets that the atmosphere does respond to mesoscale SST forcing, producing more (less) rainfall over warm (cold) eddies. However, the response strength varies considerably from dataset to dataset with the newly available high-resolution IMERG rainfall dataset revealing the strongest and most coherent response, despite the fact that the mean rainfall is the weakest in IMERG. It suggests that mean rainfall strength has little direct bearing on rainfall response to ocean eddies. Further analyses suggest that improvements in passive microwave sensors and algorithms together with the significantly enhanced resolution in IMERG collectively contribute to the more robust rainfall response in IMERG than the other two datasets. However, a detailed analysis and comparison of orbital products are required to understand the causes of these differences.

With the more robust rainfall response in IMERG, we are able to detect a distinct seasonal asymmetry in rainfall response to mesoscale SST forcing with a stronger response during winter than summer. This asymmetry can only be partly explained by the larger SSTAs in winter. The atmosphere is more sensitive to SST forcing during winter because the frequent passage of winter storms over the warmer ocean along the fronts reduces vertical stability of the atmosphere, enhancing OME-A feedback. This seasonal dependence underscores the importance of the interaction between atmospheric synoptic storms and ocean mesoscale eddies during winter.

Another important asymmetry that is better revealed by the higher resolution IMERG is in the rainfall response to warm *vs*. cold eddies; the former is more effective in

producing positive rainfall anomalies than the latter producing negative rainfall anomalies. This is important because it suggests that atmospheric response to ocean eddies is nonlinear, which can result in a non-zero net effect of ocean eddy forcing on the atmosphere at scales that are much larger than individual ocean eddy scales. In particular, the asymmetric rainfall response suggests that ocean eddy forcing may have a net impact on large-scale moisture budget within the PBL and the lower atmosphere, which can potentially affect winter cyclogenesis through moist baroclinic instability or diabatic Rossby wave processes as shown in Ma et al. (2015b, 2017). Because satellite rainfall observations alone do not provide a way to analyze the vertical structure of atmospheric response, it is beyond the scope of this study to examine whether individual eddies can produce deep convective rainfall responses in midlatitudes. However, even if such responses are absent, we submit that eddies may still exert an influence on large-scale atmospheric circulation by affecting lower atmosphere and marine boundary layer moisture budget, which in turn may affect cyclogenesis and storm tracks. As such, we emphasize the importance of understanding the asymmetry of rainfall response to warm vs. cold eddies and call for further investigations to understand the underlying mechanisms responsible for the asymmetric rainfall response to ocean eddies.

Finally, it is important to point out that satellite remotely sensed measurements are presently the only means of systematically observing rainfall over the extratropical oceans. However, the lack of *in situ* rainfall measurements over the extratropical oceans poses a great challenge for directly validating the satellite rainfall measurements, which

makes it all the more important to compare different satellite rainfall products. In this study, we also validated the statistical robustness of the results by comparing the analyses between the 11-year period that covers the entire record length of TMPA and CMORPH and the short overlapping period shared by the three datasets. The results show that the findings do not depend on the time span of the analyses. Further studies of orbital products are necessary to understand the causes of the difference among these satellite rainfall products and determine absolute errors in each of these products.

We have attempted to validate the satellite rainfall measurements against buoy rainfall measurements over the open ocean. Since our interest is in the extratropical ocean frontal region, we found only one buoy rainfall measurement located in the Kuroshio Extension region that overlaps with the three satellite rainfall products. Our comparative analyses show that IMERG is superior in estimating both the mean value and the distribution of rain rate as compared to the other two satellite-derived products. Therefore, based on all the analysis results and our understanding of OME-A interaction, we conclude that IMERG gives the most reliable estimate of rainfall response to ocean eddies. We believe that this high-resolution rainfall product will be highly valuable for validating high-resolution climate model simulations and advancing our understanding of OME-A interaction.

CHAPTER III

ASSESSING EFFECT OF MESOSCALE AIR-SEA INTERACTION ON OCEAN EDDY WIND POWER

3.1 Introduction

Wind stress provides a dominant energy source to the ocean (Lueck and Reid 1984; Ferrari and Wunsch 2009) and directly transfers atmospheric kinetic energy into the ocean by working on ocean surface currents. Based on a rough budget analysis using historical observations, Lueck and Reid (1984) estimate that the net transfer of energy is within the range of 7-36TW. A recent estimate by Ferrari and Wunsch (2009) using satellite observations gives a higher value of 65TW for the global work done by the winds. However, most of this wind energy input (about 90%) is constrained and dissipated within the surface mixing layer (Lueck and Reid 1984; Ferrari and Wunsch 2009), and only a small fraction, which is produced through near inertial oscillations and geostrophic currents, can penetrate into ocean interior, providing an important energy source for deep ocean general circulations and resupplying the potential energy loss caused by meridional overturning and eddy-generation processes (Wunsch and Ferrari 2004).

Besides the winds, other sources of energy supply to the ocean include heat transport and freshwater exchange, seafloor thermal heating, tides, and so on (Wunsch and Ferrari 2004). Although the amount of heat exchange between the ocean and atmosphere is large,

the ocean general circulation is not an efficient heat engine, and its kinetic energy comes primarily from the small fraction of wind power on geostrophic currents with tidal flows as a secondary energy supply (Wunsch and Ferrari 2004). As such, studying the wind power input on geostrophic currents, even though it is only a small fraction of the total wind power, is vital to the understanding of ocean general circulations.

Prior to the satellite era, only a few efforts (Fofonoff 1981; Oort et al. 1994) were made to estimate the wind power from ship drift observations and wind climatology. These estimates were very crude due to the limited spatial and temporal coverage of the observations. In recent years, advancements in satellite observations have made it possible to measure global sea surface height that allows a global estimate of geostrophic currents with much improved spatial resolution. Combining with the satellite measured winds, a more accurate calculation of the wind power on geostrophic flow is now possible. The global wind power on geostrophic currents is estimated within the range of 0.7TW to 1.1TW (Wunsch 1998; Scott 1999a; Scott 1999b; Von Storch et al. 2007). However, these estimates are based on a rather smooth wind stress fields, in which small-scale wind stress power is underestimated (Hughes and Wilson 2008).

It has been well established that neglecting the wind stress dependence on ocean surface currents can cause a systematic high bias in previous estimates of wind power on geostrophic currents (Duhaut and Straub 2006; Dawe and Thompson 2006; Zhai and Greatbatch 2007; Hughes and Wilson 2008; Scott and Xu 2008). Wind power is defined as:

$$P = \boldsymbol{\tau} \cdot \boldsymbol{u_0}, \quad (1)$$

where P denotes wind power, $\boldsymbol{\tau}$ wind stress vector, $\boldsymbol{u_0}$ ocean surface current vector.

Wind stress is estimated based on a bulk formulation:

$$\boldsymbol{\tau}_a = \rho_a c_d |\mathbf{U_{10}} - \boldsymbol{u_0}|(\mathbf{U_{10}} - \boldsymbol{u_0}), \quad (2)$$

where ρ_a is air density, $\mathbf{U}_{10}$ wind vector at 10 m above the sea surface, $\mathbf{u}_o$ ocean surface currents, and c_d drag coefficient that itself is a function of U_{10} and air-sea temperature difference. According to this equation, wind stress is determined by the relative motion between $\mathbf{U}_{10}$ and $\mathbf{u}_o$. Since over the most part of the ocean, the value of $\mathbf{U}_{10}$ is at least one order of magnitude larger than $\mathbf{u}_o$, the wind stress calculation is often simplified as

$$\boldsymbol{\tau}_a = \rho_a c_d |\mathbf{U_{10}}|\mathbf{U_{10}} \ , \quad (3)$$

in which wind stress $\boldsymbol{\tau}_a$ is only a function of 10m wind speed. Although the simplification in (3) causes relatively small changes in wind stress field itself, it can lead to considerable (~10-50%) overestimates of the wind power (Duhaut and Straub 2006; Dawe and Thompson 2006; Zhai and Greatbatch 2007; Hughes and Wilson 2008; Scott and Xu 2008). Thus, including the impact of surface currents on wind stress can lead to significant improvements in ocean model simulations (Pacanowski 1987; Luo et al. 2005).

The reason that the dependence of wind stress on surface currents acts to reduce wind power is nicely explained by Duhaut and Straub (2006). They show that if

$u_o / U_{10} << 1$, then the difference between the wind powers calculated from $\boldsymbol{\tau}$ and $\boldsymbol{\tau}_a$ is given by

$$\Delta P_1 = \boldsymbol{\tau} \cdot \mathbf{u}_0 - \boldsymbol{\tau}_\mathbf{a} \cdot \mathbf{u_0} \approx -\rho_a c_d |\mathbf{U_{10}}|(|\mathbf{u_0}|^2 + |\mathbf{u_0} \cdot \mathbf{n}|^2), \qquad (4)$$

where $\mathbf{n}$ is a unit vector pointing to the wind direction. As evident from (4), ΔP_1 is negative definite, indicating that the correction of $\boldsymbol{\tau}$ due to $\mathbf{u}_0$ always reduces the wind power. Moreover, (4) suggests the wind power reduction scales as kinetic energy of ocean surface currents. Previous numerical model studies estimate that after including surface current effects, ocean eddy kinetic energy is reduced by 10%-50% (e.g., Zhai and Greatbatch 2007; Eden and Dietze 2009; Seo et al. 2016; Renault et al. 2016). A rough estimate by Hughes and Wilson (2008) suggests that 75% of the wind power difference resulting from ignoring the surface currents effects may be related to eddy kinetic energy. Although the dependence of wind stress on surface currents seems to play a major role in determining wind power on ocean eddies, the relative importance of this effect to other influence factors, such as eddy-induced SST effects on winds, has not been well established.

Over past decades, due to progress in satellite remote sensing technology, high-resolution observations of surface winds and ocean surface variables, such as SST and sea-surface height, have become available, allowing for the identification of active coupling between ocean meso-scale eddies and atmosphere (OME-A) (Chelton et al. 2004; Xie 2004; Small et al. 2008; Chelton and Xie 2010). This active coupling is fundamental to the dynamics of the energetic western boundary currents (Ma et al. 2016).

From the coupled climate model simulations, without considering this OME-A feedback, the Kuroshio extension jet is weakened by ~20-40%, and EKE at wavelengths shorter than 100km increases by ~30% (Ma et al. 2016). These changes imply suppressing OME-A feedback can change the eddy energy balance. The remarkable positive correlation between meso-scale SST and wind speed over major oceanic fronts (Chelton et al. 2004; Park et al. 2006; Xie et al. 2002; O'Neil et al. 2005; Tokinaga et al. 2005; Frenger et al. 2013; Ma et al. 2015 and Byrne et al. 2015) raises a strong possibility that OME-A feedback can affect wind power over eddies. Thus, revealing the response of eddy wind power, which plays as a vital role in EKE budget, to the OME-A feedback can help us understand the physical processes governing eddy energy even to the dynamics governing the oceanic frontal regimes.

Although some previous studies estimate that the contribution of OME-A feedback to wind power may be negligibly small (e.g., Hughes and Wilson 2008), no studies have fully quantified this effect until very recently. Novel studies using a high-resolution regional coupled model by Seo et al. (2016; 2017) attempt to assess the relative impact of surface currents *vs*. OME-A feedback on eddy kinetic energy in the California Current System and in the Arabian Sea. The results show that the dependence of wind stress on surface currents significantly reduces EKE, while OME-A feedback has relatively smaller impact, even though eddy wind power tends to be more negative leading to stronger sink of EKE when the OME-A feedback is excluded. In contrast, a study by Byrne et al. (2016) indicates that in the South Atlantic OME-A interaction overweights

the damping effect on ocean eddies caused by the dependence of wind stress on surface currents. These contradictory studies motivate us to carry out a comprehensive global analysis on the potential importance of OME-A feedback in wind power compared to the effect of ocean surface currents.

To the best of the author's knowledge, no studies exist to quantify the influence of OME-A feedback on wind power and to reveal the importance of OME-A feedback in wind power compared to the effect of ocean surface currents globally. Therefore, the objective of this study is to conduct a systematic investigation to explore wind power on ocean eddies over the global oceans using a scaling analysis and the coupled numerical model simulations, and to understand whether and why OME-A interaction can affect wind power on ocean eddies.

3.2 Models and Methods

3.2.1 High-resolution Model Simulations

Both high-resolution regional and global climate model simulations were used in this study. For regional model simulations, we used the twin ensembles of coupled regional climate model (CRCM) simulations conducted in the North Pacific domain [3.6°N to 66°N, 99°E to 270°E] as described in Ma et al. (2016). The CRCM consists of Weather Research and Forecasting (WRF) model and Regional Ocean Modeling System (ROMS) at 9 km horizontal resolution. Each of the twin CRCM ensembles consists of 6 winter-season (ONDJFM) simulations, initialized on October 1, 2002, 2003, 2004, 2005,

2006, 2007, with lateral boundary conditions derived from 6-hour National Center for Environmental Prediction-II (NCEP-II) reanalysis for WRF and 5-day average the Simple Ocean Data Assimilation (SODA) ocean/sea ice reanalysis output for ROMS (Ma et al. 2016). The only difference between the two ensembles lies in the SST at each coupling step (Fig. 3.1). In the smoothed ensemble (Fig. 3.1a), SST is subject to a spatial low-pass filter before passed to the atmosphere to remove OME-A feedback, while in the control ensemble (Fig. 3.1b), no filter is used. As a result, in the smoothed ensemble the atmosphere cannot feel ocean mesoscale eddies (Fig. 3.1c). A comparison between the twin ensembles allows us to assess the impact of OME-A feedback on wind power on Kuroshio eddies in the North Pacific during winter.

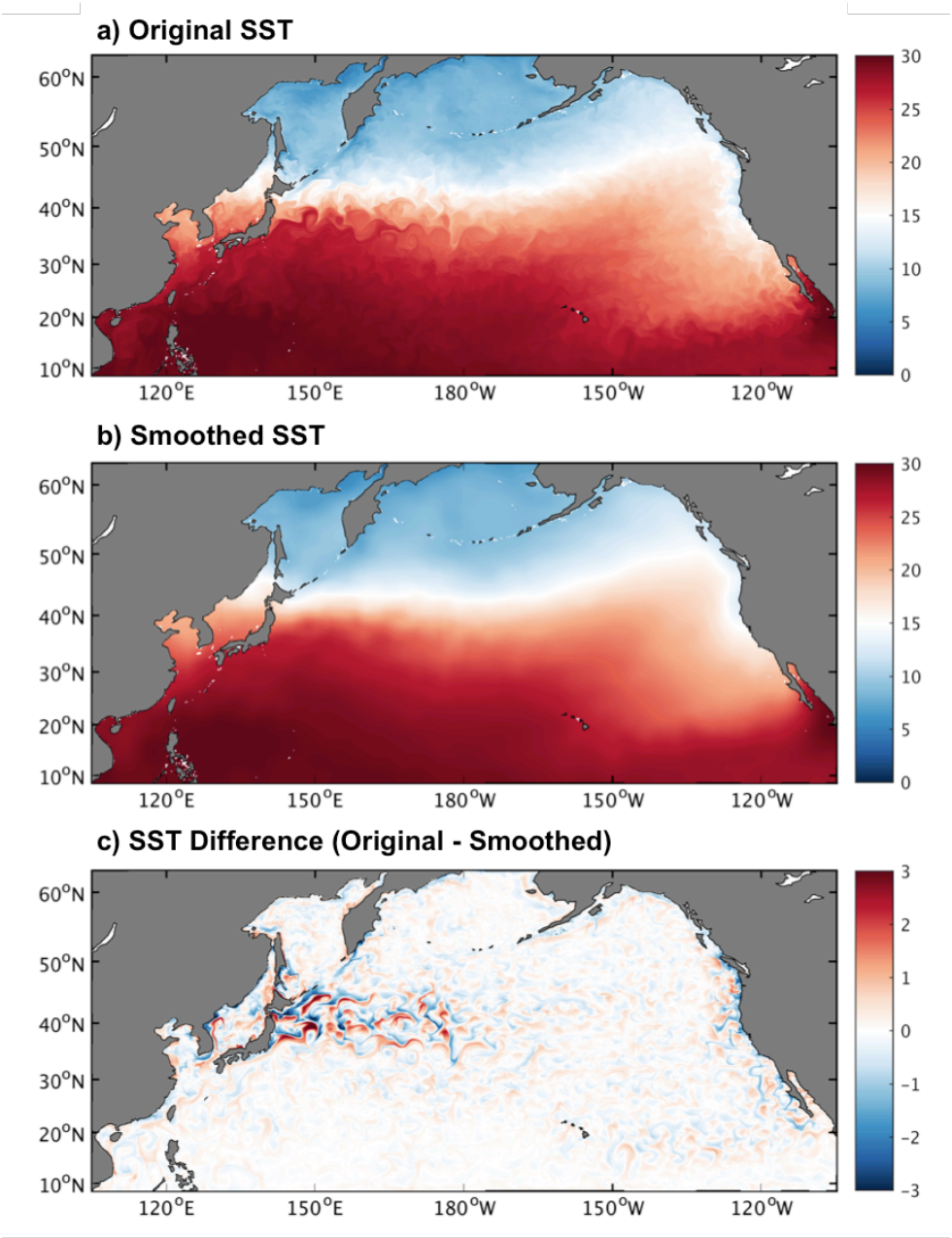

FIG. 3.1. One snapshot of a) original SST; b) smoothed SST; c) SST differences between control and smoothed ensembles in CRCM.

For global model simulations, we used the eddy-resolving Community Earth System Model (CESM) simulations conducted by NCAR. The version of the CESM used for these simulations were configured with a 0.25° Community Atmosphere Model version 5

(CAM5) and a 0.1° Parallel Ocean Program version 2 (POP2) (Small et al. 2014). A set of twin simulations – one control and one smoothed run similar to the CRCM twin ensembles – has been conducted for 11 years (Fig. 3.2). A comparison between these runs allows us to examine the effect of OME-A feedback on ocean eddy wind power in different seasons and different regions of the oceans. The analysis will focus on the eddy-active regions over the global ocean, where the SST perturbations are large (4 boxes in Fig. 3.2), including the Kuroshio Extension, the Gulf Stream, the Agulhas Current Retroflection and the Brazil-Malvinas Confluence. The very same regions were used in Chapter 2 to analyze rainfall response to eddy-induced SST.

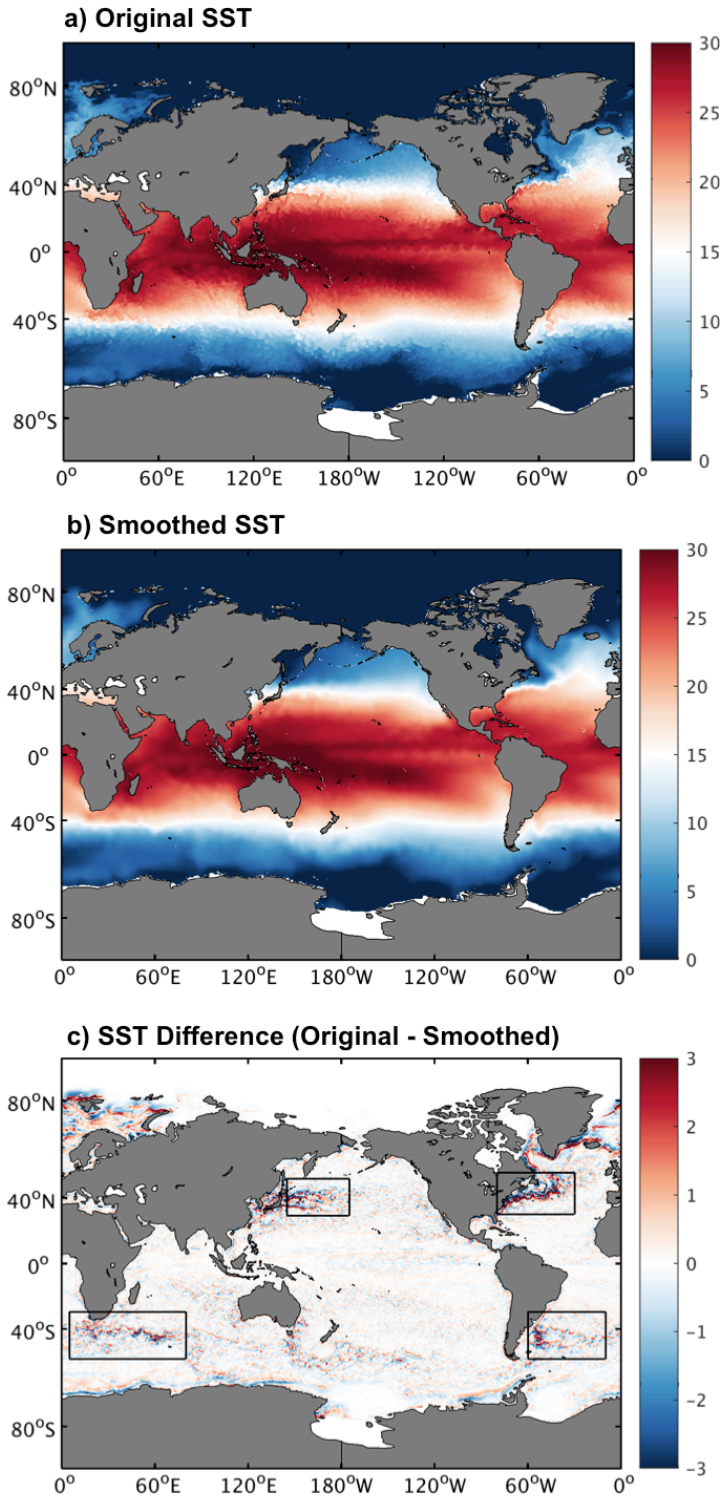

FIG. 3.2. One snapshot of a) original SST; b) smoothed SST; c) differences between original and smoothed SST in CESM. Black boxes mark the regions where the feedback of OME-A interaction is analyzed.

3.2.2 Eddy Identification and Composite

Following Kurian et al. (2011), we applied the same detecting algorithm as described in Chapter 2.2.2 to identify cyclonic and anticyclonic eddies using Sea Level Anomaly (SLA) from CRCM and CESM. SST anomaly (SSTA) corresponding to each of identified eddies, which is defined as area-averaged SST over 1.5 eddy-radius area minus averaged SST value over an annulus between 2.5 and 1.5 eddy-radii, is computed to group the eddies into anticyclonic eddies and cyclonic warm eddies. The same SST threshold as described in Chapter 2.2.2 was applied to select the eddies that retain sufficiently strong SST anomalies to have an effect on the atmosphere. Finally a total of ~37,000 eddy snapshots were identified in CRCM over the Kuroshio extension, and ~2,153,000 eddy snapshots were identified in CESM over our four target regions, where influence of OME-A interactions on eddy wind power is strong.

The composite analysis follows closely to that described in Chapter 2.2.3. For identified eddy snapshots, since eddy sizes vary considerably, we normalized the relevant variables, such as wind stress, currents, and wind power on each identified eddy by its radius. Different from Chapter 2, we did not subtract a background value surrounding each eddy to minimize the influence of background field, since the sampling size is much larger in this case than the previous case, and the eddy imprints of wind and currents are much easier to detect than rainfall. We then rotate each eddy to a common westerly background wind direction, which is defined by the direction of the area mean winds over a 14 eddy-radius area aligned with eddy center. Finally, composite maps of wind stress,

current, and wind power were made over all the anticylonic warm and cyclonic cold eddies. Note that for vectors, such as eddy currents and wind stress, the x and y components need to be projected into the new coordinate, where the new x axis is in the same direction with the large-scale background wind, before making the composite.

3.3 Scaling Analysis

A large body of literatures now exist on robust surface wind response to ocean eddy-induced SSTs. An increase (decrease) in wind speeds over warm (cold) eddies is well observed (e.g., Chelton et al. 2004; Chelton and Xie 2010; Frenger et al. 2013). This response has been explained by two different mechanisms - Vertical Mixing Mechanism (VMM) (Fig. 3.3) and Pressure Adjustment Mechanisms (PAM) (Fig. 3.4). VMM argues that warm (cold) sea surface temperature reduces (enhances) the stability of the overlying atmosphere, promoting (reducing) the downward transfer of momentum from free atmosphere to planetary boundary layer through vertical mixing, which leads to the increased (decreased) surface wind speed (Wallace et al. 1989, O'Neil et al. 2010). On the other hand, PAM reasons that low (high) surface pressure anomalies induced by warm (cold) SST anomalies account for an increased (decreased) surface wind speed. Because different physical processes are involved in VMM and PAM, the surface wind response is different between these two mechanisms. In VMM, maximum wind speed anomalies tend to coincide with eddy center where maximum SST anomalies locate,

whereas in PAM, the wind anomalies tend to form along eddy edge where maximum SST gradient occurs.

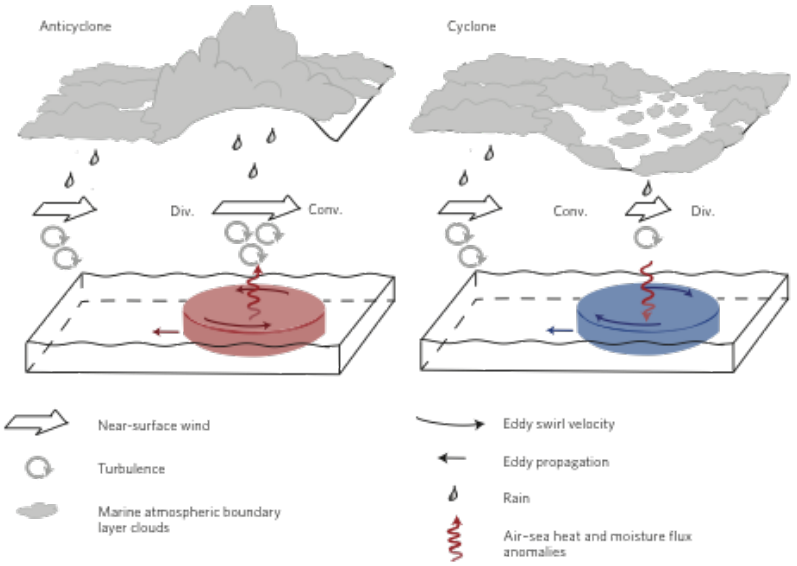

FIG. 3.3. Schematic summarizing the impact of anticyclonic warm eddies (red, left) and cyclonic cold eddies (blue, right) on the overlying lower atmosphere for vertical mixing mechanism. From Frenger et al. 2013.

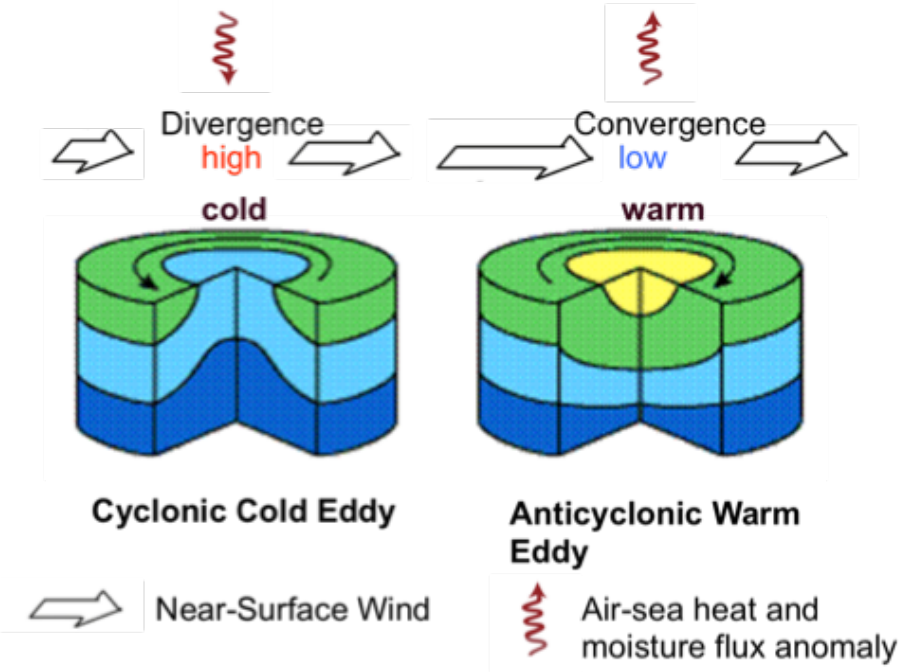

FIG. 3.4. Schematic summarizing the impact of anticyclonic warm eddies (right) and cyclonic cold eddies (left) on the overlying lower atmosphere for pressure adjustment mechanism.

No matter which mechanism is dominant, assuming that the eddy-SST induced wind speed anomaly is u_t, when an absolute background wind, $\mathbf{U_{10}}$, blows over a warm (cold) eddy, the total wind can be expressed as $\mathbf{U}=(|\mathbf{U_{10}}|+u_t)\mathbf{n}= \mathbf{U_{10}}+ u_t\mathbf{n}$. Then the wind stress, $\boldsymbol{\tau}_{new}$, accounting for both effects of ocean surface currents and eddy-SST induced surface wind changes can be computed as

$$\boldsymbol{\tau}_{new} = \rho_a c_d|\mathbf{U}-\mathbf{u_0}|(\mathbf{U}-\mathbf{u_0})$$

$$= \rho_a c_d|\mathbf{U_{10}}+u_t\boldsymbol{n}-\mathbf{u_0}|(\mathbf{U_{10}}+u_t\boldsymbol{n}-\mathbf{u_0})$$

$$\approx \rho_a c_d(|\mathbf{U_{10}}|+u_t-\mathbf{u_0}\mathbf{n})(\mathbf{U_{10}}+u_t\boldsymbol{n}-\mathbf{u_0}). \quad (5)$$

Assuming $|\mathbf{U_{10}}| \gg |\mathbf{u_o}| \sim u_t$, using (3) and (5), one can derive the wind stress difference between $\boldsymbol{\tau}_{new}$ and $\boldsymbol{\tau}_{\mathbf{a}}$:

$$\Delta\boldsymbol{\tau} = \boldsymbol{\tau}_{new} - \boldsymbol{\tau}_{\mathbf{a}} \approx -\rho_a c_d|\mathbf{U_{10}}|\mathbf{u_0} - \rho_a c_d(\mathbf{u_0}\cdot\mathbf{n})\mathbf{U_{10}} + 2\rho_a c_d|\mathbf{U_{10}}|u_t\mathbf{n}. \quad (6)$$

Thus, the difference between the wind power computed using the absolute wind stress $\boldsymbol{\tau}_a$ and that using the wind stress $\boldsymbol{\tau}_{new}$ accounting for both effects of ocean surface currents and eddy-SST induced surface wind changes is given by

$$\Delta P = \mathbf{u_0}\cdot\Delta\boldsymbol{\tau} \approx \Delta P_1 + 2\rho_a c_d|\mathbf{U_{10}}||\mathbf{u_o}|(\mathbf{n}\cdot\mathbf{i})u_t = \Delta P_1 + \Delta P_2, \quad (7)$$

where ΔP_1 is the wind power difference caused by ocean surface current impact alone given by (4), $\boldsymbol{n}$ and $\boldsymbol{i}$ are unit vectors representing the wind direction and surface current direction, respectively, and u_t is the wind speed anomaly caused by eddy-induced SST anomaly. The second term ΔP_2 on the right-hand-side of (7) is the wind power change caused by OME-A feedback, which is not simply determined by

eddy-SST induced wind speed anomaly, but also by ocean surface current $|u_0|$. In fact, if $|u_0|$ is zero, ΔP_2 is zero.

Since $|\mathbf{u_o}| \sim u_t$, $\frac{\Delta P_1}{\Delta P_2} = \frac{|\mathbf{u_0}|^2 + |\mathbf{u_0} \cdot \mathbf{n}|^2}{2|\mathbf{u_0}| u_t (\mathbf{n} \cdot \mathbf{i})}$ ~1, indicating that at a given location the wind power differences induced by ocean surface currents and OME-A feedback are on the same order and have comparable values. However, this does not necessarily mean that they are of the same importance when integrated over eddies or over a large region. This is because unlike ΔP_1, ΔP_2 is not sign-definite. The area-integrated magnitude of ΔP_2 is determined by the relationship among $|\mathbf{U_{10}}|$, u_t and $|\mathbf{u_o}|$. In the case of a constant background wind blowing over a symmetric eddy, if the maximum SST anomalies locate at eddy center, the net effect of OME-A feedback on wind power over an eddy, which is obtained by integrating ΔP_2 over the eddy, can be shown to be zero. However, in reality, the assumption of constant $|\mathbf{U_{10}}|$ over eddies and symmetric u_t and $|\mathbf{u_o}|$ distributions is difficult to satisfy simultaneously. Therefore, averaged ΔP_2 over eddies will not be zero, but its magnitude is likely to be smaller than that of ΔP_1, because of the sign-indefinite nature of ΔP_2. Therefore, OME-A feedback can have a sizable impact on ocean eddy wind power, although the amplitude of the impact is likely smaller than that due to ocean surface current effects on wind power. We will validate this scaling argument using the coupled model simulations in the section 3.4.

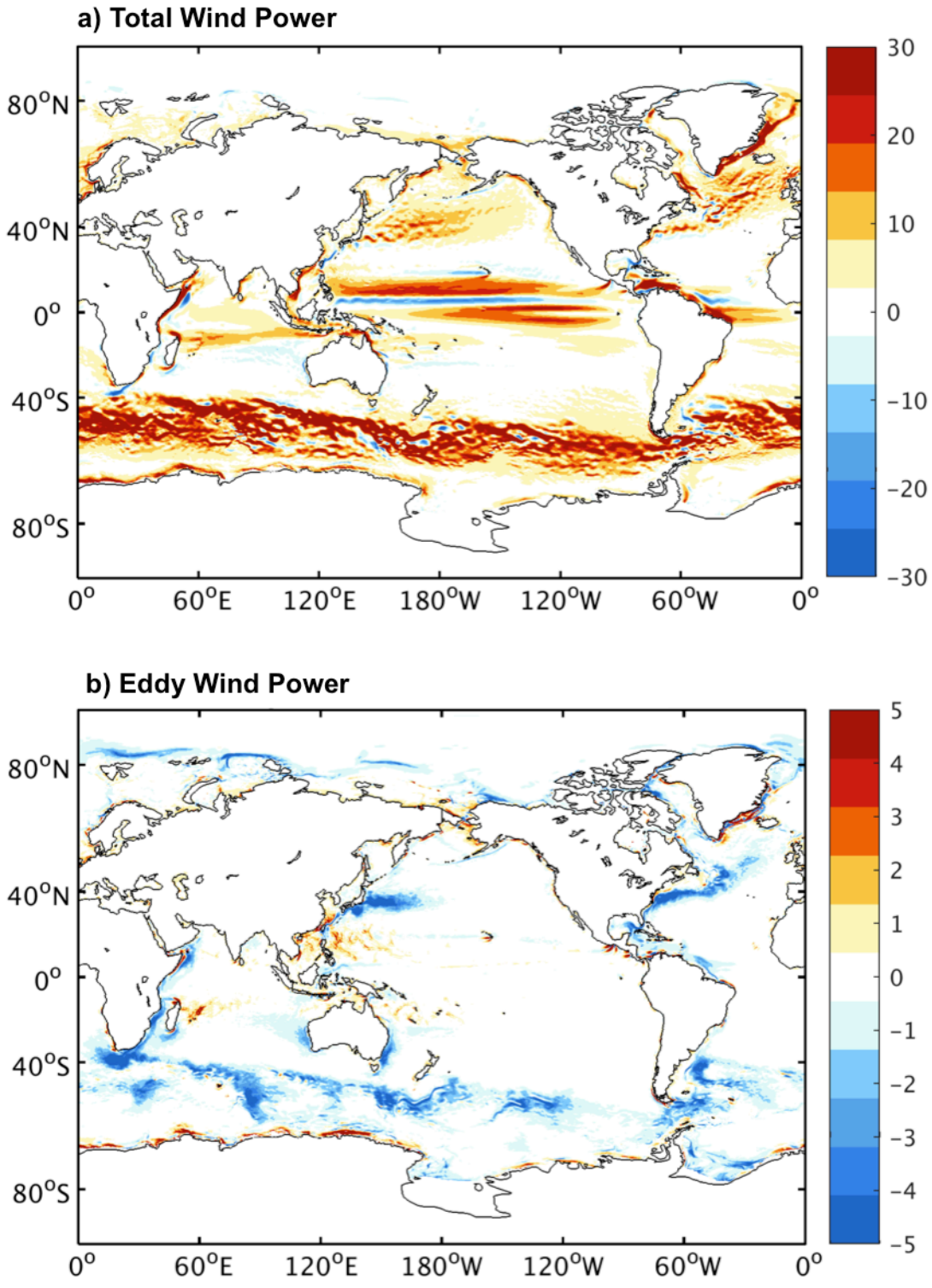

FIG. 3.5. Wind power (mW/m^2) derived from the CESM control simulation. (a) Total wind power and (b) eddy wind power.

3.4 Simulated Total Wind Power *VS* Eddy Wind Power

Fig. 3.5a displays the total wind power calculated from CESM control run averaged over the 11-year simulation period. Both the value and the pattern are in an agreement with previous estimates (e.g. Scott and Xu 2009) derived from altimeter and scatterometer data, demonstrating that the eddy-resolving CESM simulation is capable of reproducing the observed wind power. It shows positive values globally except for the equatorial countercurrents region, where the currents flow in the opposite direction with the trade wind. This pattern indicates that over most parts of the global ocean wind energy is transferred into the ocean from the atmosphere to drive large-scale ocean circulations. The CRCM control run exhibits a similar pattern with positive values over most parts of the North Pacific in winter (Fig. 3.6), suggesting that CRCM is also capable of reproducing realistically the observed wind power.

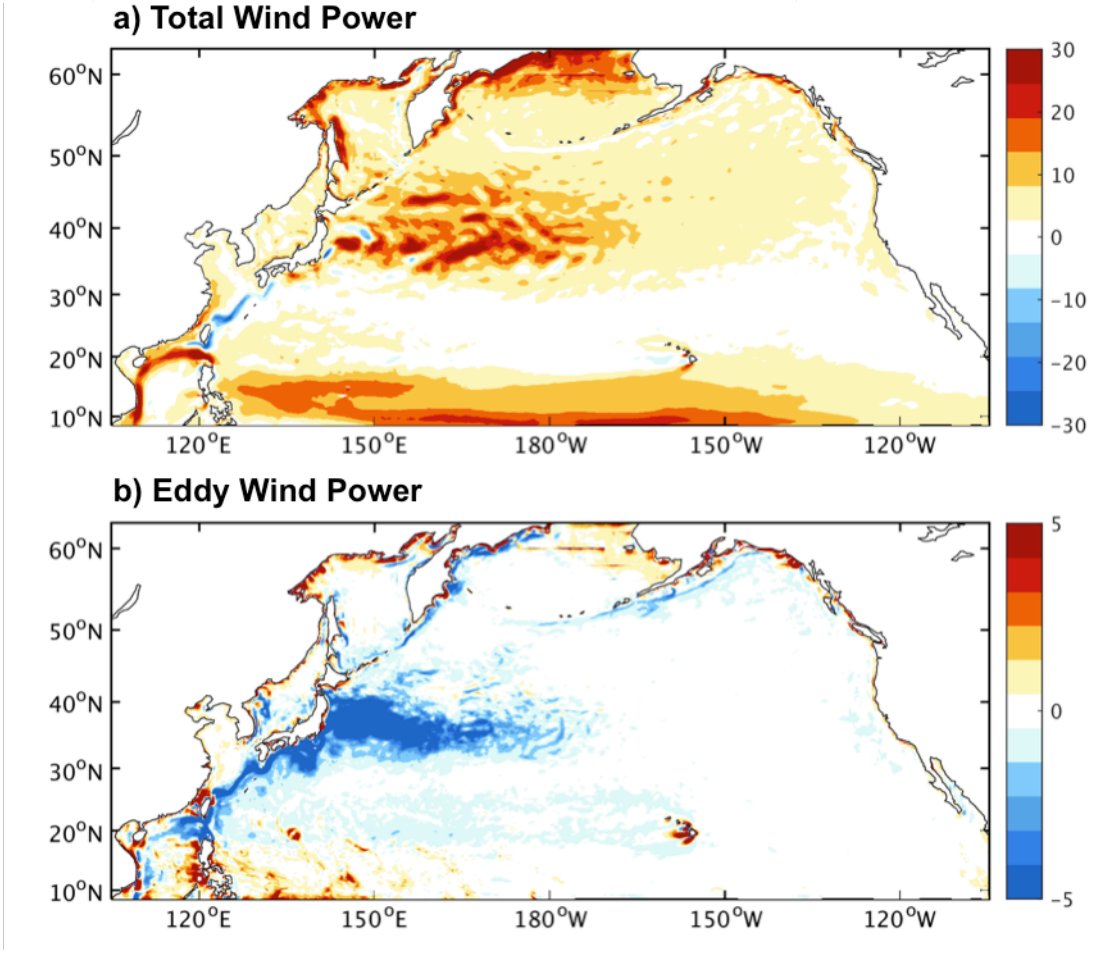

FIG. 3.6. Wind power (mW/m^2) derived from the CRCM control ensemble. (a) Total wind power and (b) eddy wind power.

Figure 3.7 shows the coherence between wind speed and SST in wave length space (x-axis) using the CRCM control and smoothed ensemble. The correlation changes its sign from negative to positive at around 1000 km length scale. SST and wind speed are positively correlated within length scales between 50km to 500km in the CRCM control ensemble, but become decorrelated in the smoothed ensemble when OME-A feedback is suppressed. At scales larger than 1000km, wind speed and SST are negatively correlated. The CESM simulations show similar coherence. This is consistent with the previous

discussion in Chapter 1 that interaction between the ocean and atmosphere is scale-dependent.

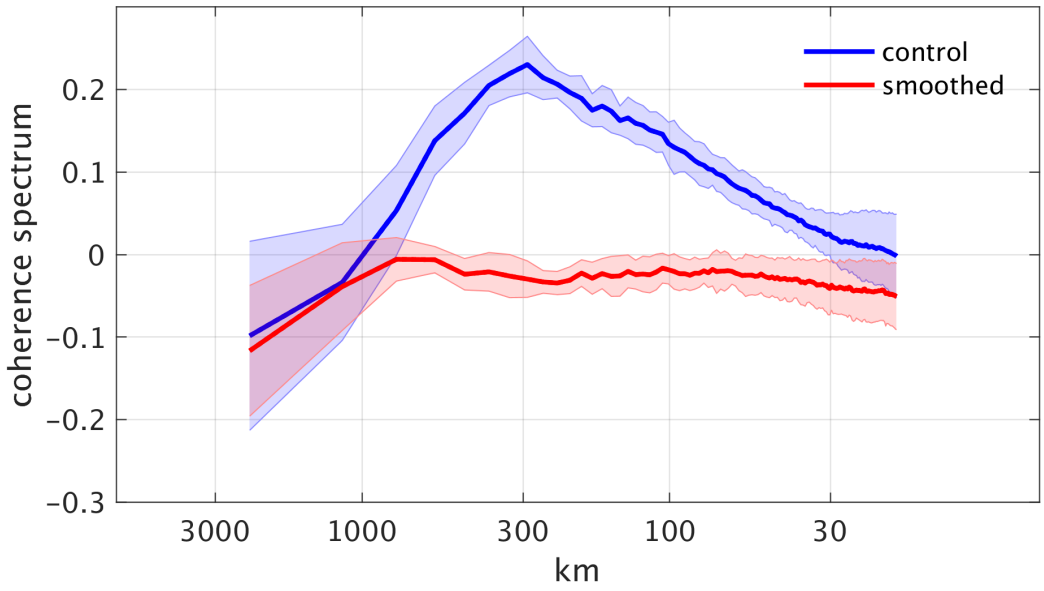

FIG. 3.7 Coherence between surface winds and SST. Coherence between surface winds and SST in wave length space in CRCM control ensemble (blue) and the smoothed ensemble (red). Shades indicate the corresponding standard deviation.

Thus, to estimate eddy wind power, we applied a spatial high-pass filter (with a cutoff wave length of 1000km) to the simulated wind stress and currents and then computed the wind power using the high-pass filtered wind stress and currents. The results from CESM (Fig. 3.5b) show, in contrast to total wind power that is dominated by the large-scale wind power, eddy wind power has negative values almost everywhere especially over the western boundary current regions and in the Southern oceans. This is consistent with the calculation from altimeter and scatterometer data by Xu et al. (2016) and confirms the previous finding by Zhai and Greatbatch (2007) and Hughes and Wilson

(2008). The pattern of eddy wind power looks similar to the reduction of wind power estimates by using wind stress $\boldsymbol{\tau}$ to replace $\boldsymbol{\tau}_a$ (e.g. Zhai and Greatbatch 2007; Hughes and Wilson 2008; Zhai et al. 2012). This suggests that the eddy wind power is largely due to the influence of eddy circulation on wind stress. And the negative value is in a good agreement with the negative definite ΔP_1 in equation (2) (Duhaut and Straub 2006), indicating that eddy wind power works to transfer the EKE out of the ocean. In the western boundary current regions and in the southern ocean, both the ocean eddies and the atmospheric storms are active (Xu et al. 2016), i.e. $|\boldsymbol{u_0}|$ and $|\mathbf{U_{10}}|$ are large, leading to a large magnitude of negative ΔP_1 based on equation (2). As a result, eddy wind power is especially strong in these regions. Again, CRCM shows similar pattern over the north Pacific and the negative values prevail along the Kuroshio and its extension in winter.

3.5 Effects of OME-A Feedback on Eddy Wind Power

3.5.1 Eddy Wind Power Response to OME-A Feedback

To examine the effect of OME-A feedback on eddy wind power, we calculated the eddy wind power difference between CRCM smoothed and control ensembles, and between CESM smoothed and control simulations. Recall that in the smoothed ensembles, the atmosphere models do not feel eddy-induced SSTs and thus the winds have no imprints of ocean eddies. As a result, the smooth ensembles only contain eddy current feedback but no OME-A feedback that considers the eddy-induced SST effects on the

atmosphere. In contrast, the control ensembles include both feedbacks. Therefore, the difference between the smoothed and control ensembles allows us to quantify the importance of OME-A feedback in eddy wind power. In CESM (Fig. 3.8), negative differences prevail over most parts of the ocean implying that the sink effect of eddy wind power is stronger in the smoothed run, that is OME-A feedback tends to reduce the damping effect of wind power on ocean eddies. This difference is especially significant over the western boundary current regions and the southern ocean where the OME-A interactions are intense (Small et al. 2008) and eddy wind power is strong. Note that there is a dipole-like pattern in the difference map, negative in the north and positive in the south, over the Kuroshio current and Gulf stream, which is caused by the northward shift of mean current in the smoothed simulations (Ma et al. 2016). Comparison of eddy wind power between CRCM smoothed and control ensembles further confirms the finding that OME-A feedback decreases the sink of eddy wind power (Fig. 3.9). The decrease of the global integral of eddy wind power in the control run compared to the smoothed run can reach to ~48% in CESM, while in CRCM the integrated eddy wind power over the domain is reduced by ~31% in the control run.

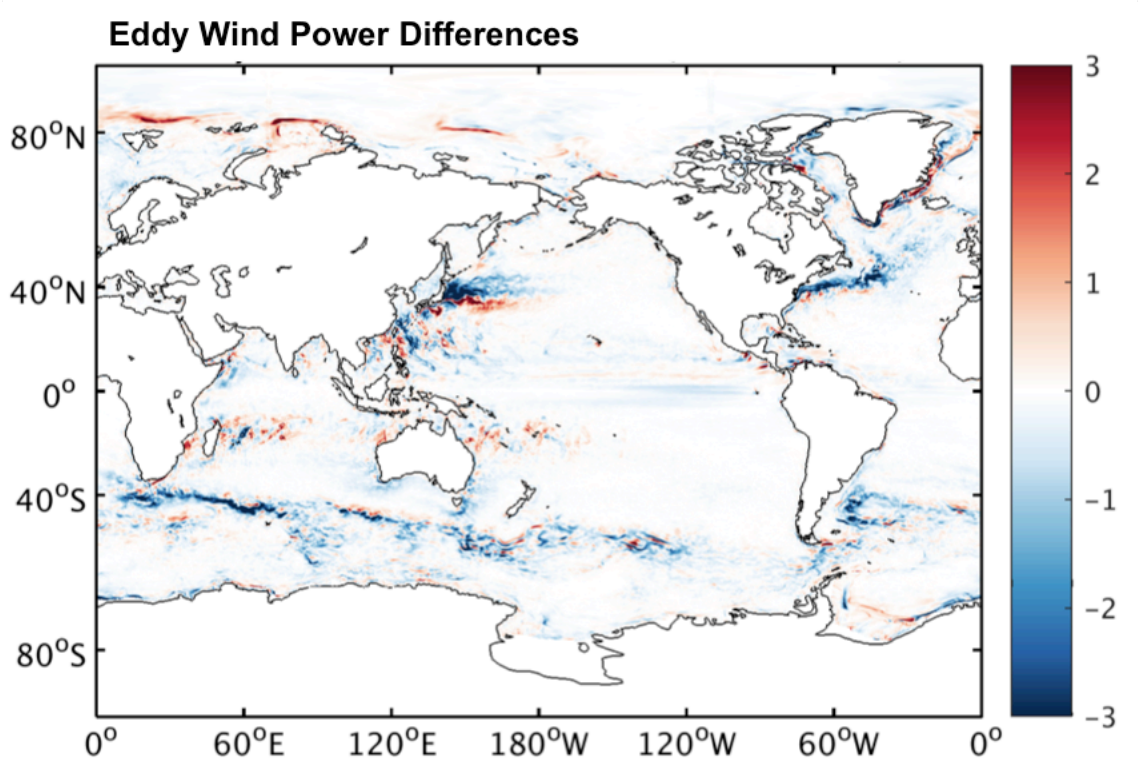

FIG. 3.8 Eddy wind power (mW/m^2) difference between CESM smoothed and control simulations.

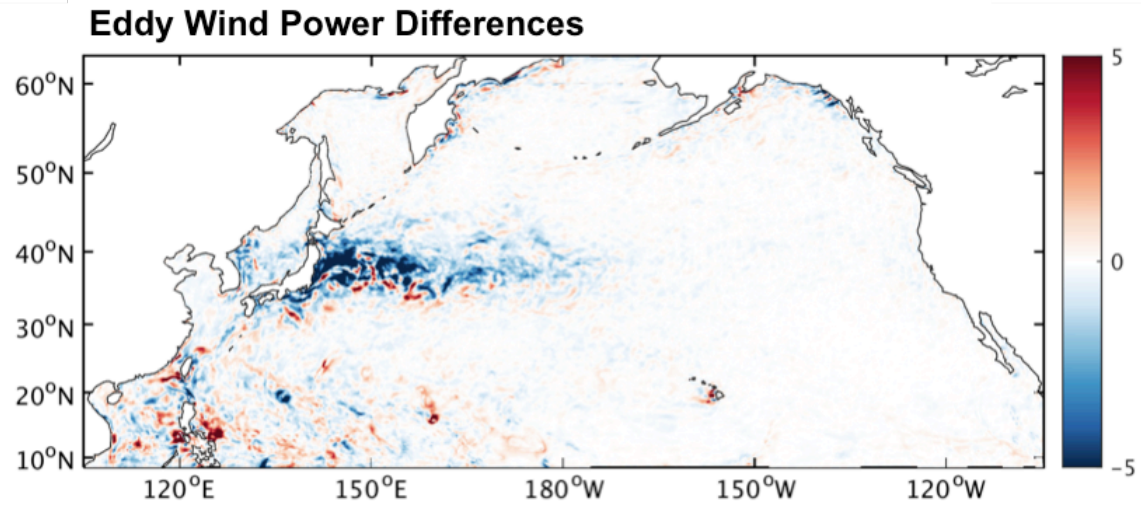

FIG. 3.9 Eddy wind power (mW/m^2) difference between CRCM smoothed and control ensembles.

3.5.2 Response Difference over Anticyclonic Warm Eddies VS Cyclonic Cold Eddies

As mentioned earlier, over anticyclonic warm (cyclonic cold) eddies, wind speed is increased (decreased) (e.g. Frenger et al. 2013). If eddies are strictly symmetric, the impact of OME-A feedback on wind power over a large domain will be largely cancelled out, assuming that the magnitude of wind speed response over warm and cold eddies is the same. However, eddies in reality are not symmetric and, based on our previous analyses, the atmospheric response to warm and cold eddies is also not symmetric. Thus, a none-zero net effect of OME-A feedback on eddy wind power is expected. In the following, we attempt to quantify this effect by analyzing wind power response to eddy-induced SST over individual eddies.

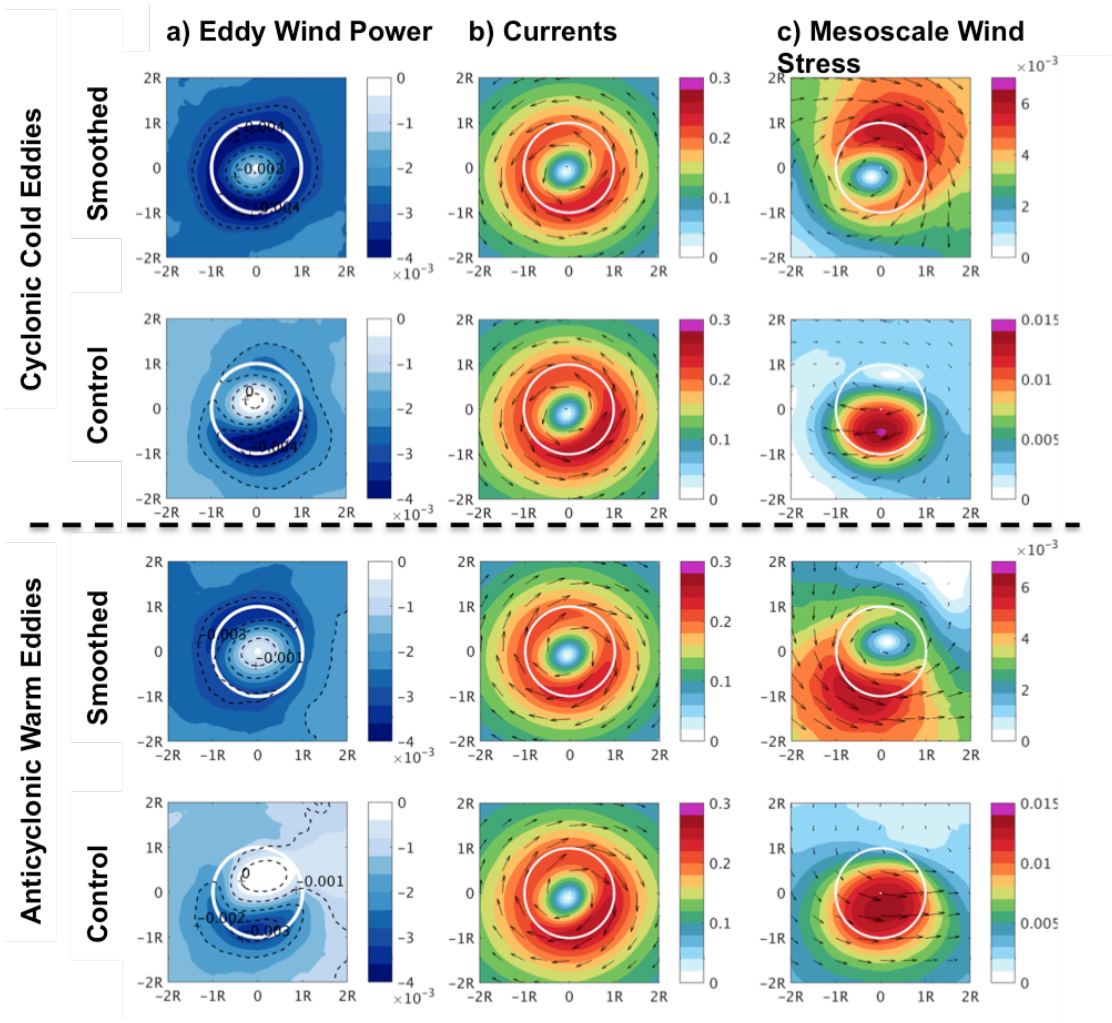

FIG. 3.10 Composite of cyclonic cold eddies (Upper two panels) and anticyclonic warm eddies (lower two panels) for (a) eddy wind power (W/m^2), (b) eddy current (m/s), (c) mesoscale wind stress (N/m^2) from the CESM smoothed simulation (first and third panels) and control simulation (second and fourth panels) over Kuroshio Extension region during winter. White contour and dot mark one eddy radius and eddy center.

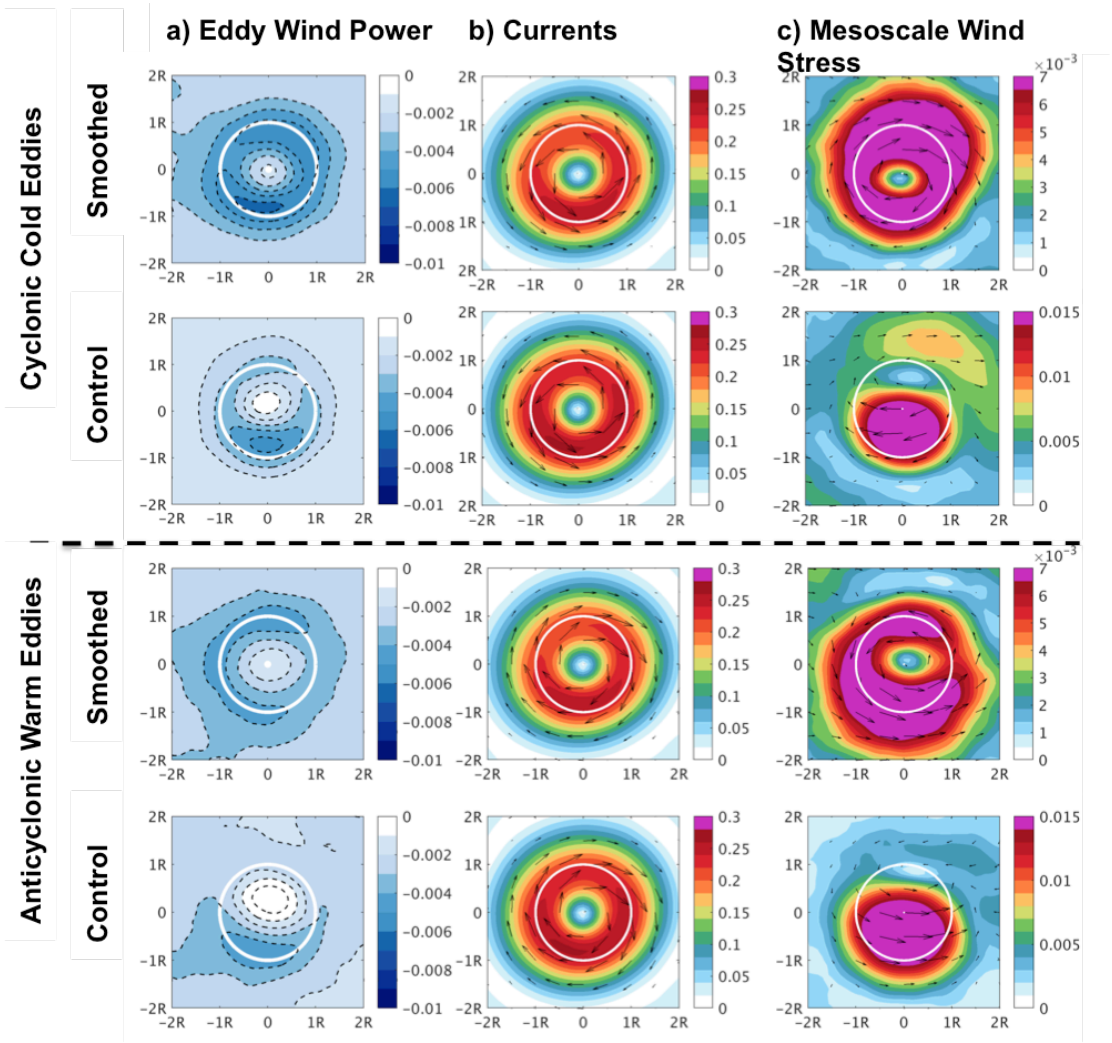

FIG. 3.11 Composite of cyclonic cold eddies (Upper two panels) and anticyclonic warm eddies (lower two panels) for (a) eddy wind power (W/m^2), (b) eddy current (m/s), (c) mesoscale wind stress (N/m^2) from CRCM smoothed ensemble (first and third panels) and control ensemble (second and fourth panels) over Kuroshio Extension region during winter. White contour and dot mark one eddy radius and eddy center.

Since the dominant mechanism of OME-A interactions may be different, eddy wind power over warm and cold eddies in winter and summer (in section 3.5.4) are analyzed separately. The composites of eddy wind power over the detected cyclonic cold and anticyclonic warm eddies in Kuroshio Extension during winter from CESM (Fig. 3.10)

and CRCM (Fig. 3.11) are first examined. Eddy wind power always retains negative values, indicating that it sinks energy from ocean eddies, which is consistent with the previous analysis. In the smoothed simulations, it has a nearly symmetric structure with the smallest negative value occurring near the eddy center and the largest negative values locate around the one eddy radius edge. In the smoothed run, composited wind stress structure over eddies is only affected by eddy currents whose maximum locates near the one eddy radius edge, and thus the largest magnitude for the wind stress also occurs near the one-radius edge. Since wind power is the product of eddy currents and wind stress, it is no surprise that the maximum value of the negative eddy wind power occurs in the same region. However, in the control simulations, eddy wind power becomes more asymmetric. On the northern side of the eddy, its negative values become weaker. This can be explained as follows. In both control and smoothed simulations, little differences are found in eddy currents and the most differences occur in the simulated wind stress over eddies. In the control simulations composite wind stress maximum moves from the eddy edges towards the eddy center compared to the one in the smoothed runs. This change in the wind stress is consistent with the atmospheric response to eddy-induced SST, which will be explained in details in the next section. Since eddy current velocity is close to zero in the center, when the wind stress is multiplied with the eddy current velocity to obtain the wind power, the large magnitude of the wind stress near the eddy center does not contribute to the wind power. As a result, the wind power on the northern portion of the composite eddy is significantly reduced, leading to the smaller overall

integrated value in the control simulations. This is the case for both anticyclonic warm eddies and cyclonic cold eddies. Comparisons between smoothed and control simulations show that OME-A feedback always tends to reduce the eddy wind power, but the reduction appears to be more pronounced for anticyclonic warm eddies than cyclonic cold eddies. We expand these analyses to other oceanic frontal regions, including the Gulf Stream, the Brazil-Malvinas Confluence and the Agulhas Current Retroflection using the CESM control and smoothed simulations. Composite maps of eddy wind power, eddy currents and mesoscale wind stress in the Gulf Stream are all similar to those in the Kuroshio Extension, and thus are not shown here. But in the southern hemisphere, because anticyclonic (cyclonic) eddies rotate counterclockwise (clockwise), both the composite wind stress and eddy currents flow in the opposite direction to the ones in the northern hemisphere. As an example, we show the composite analysis of eddies in the Brazil-Malvinas Confluence (Fig. 3.12). Similar to the composites in the northern hemisphere, eddy wind power has negative values and has reduced values when including the OME-A feedback, except that the large reduction now occurs in the southern portion of the composite eddy.

We further computed the averaged wind power over eddies and compared them between control and smoothed simulations. In the absence of OME-A feedback, averaged eddy wind power over a 2 eddy-radius box decreases by 27% over cyclonic cold eddies, but by 40% over anticyclonic warm eddies in Kuroshio Extension region during winter from CESM. These analyses are repeated for other three target regions. In the Gulf

Stream region, averaged eddy wind power reduces by 31% over cold eddies and 43% over warm eddies. And the corresponding values are 32% (41%) and 45% (57%) over the warm and cold eddies respectively in the Agulhas Return Current (Brazil-Malvinas Confluence). These results indicate that the wind power response is inherently more sensitive to warm SSTAs than cold SSTAs. CRCM confirms this asymmetric wind power response to warm and cold eddies. From CRCM, the reduction of averaged eddy wind power is about 16% over cold eddies and about 25% over warm eddies over the Kuroshio Extension during winter.

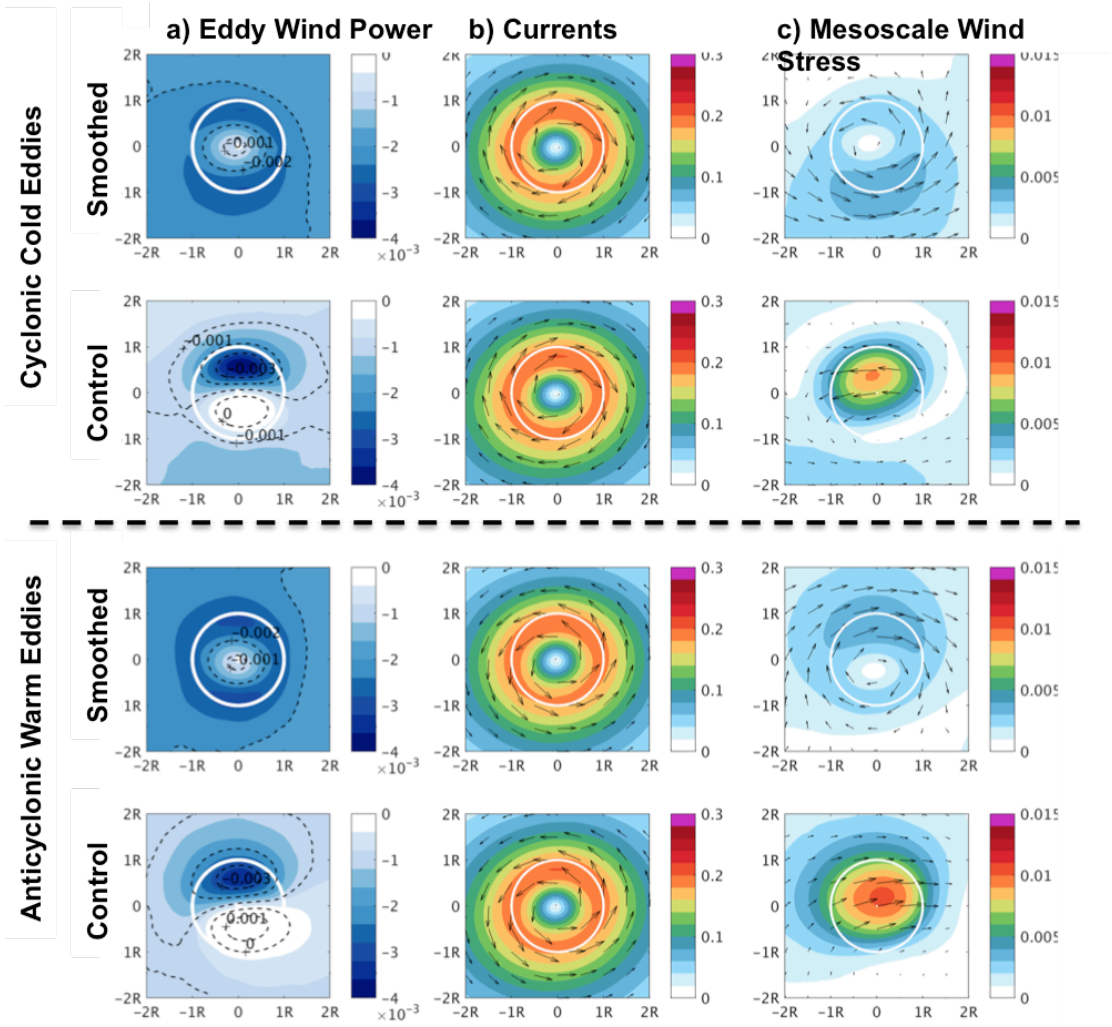

FIG. 3.12 Composite of cyclonic cold eddies (Upper two panels) and anticyclonic warm eddies (lower two panels) for (a) eddy wind power (W/m^2), (b) eddy current (m/s), (c) mesoscale wind stress (N/m^2) from CESM smoothed simulations (first and third panels) and control simulations (second and fourth panels) over Brazil-Malvinas Confluence during winter. White contour and dot mark one eddy radius and eddy center.

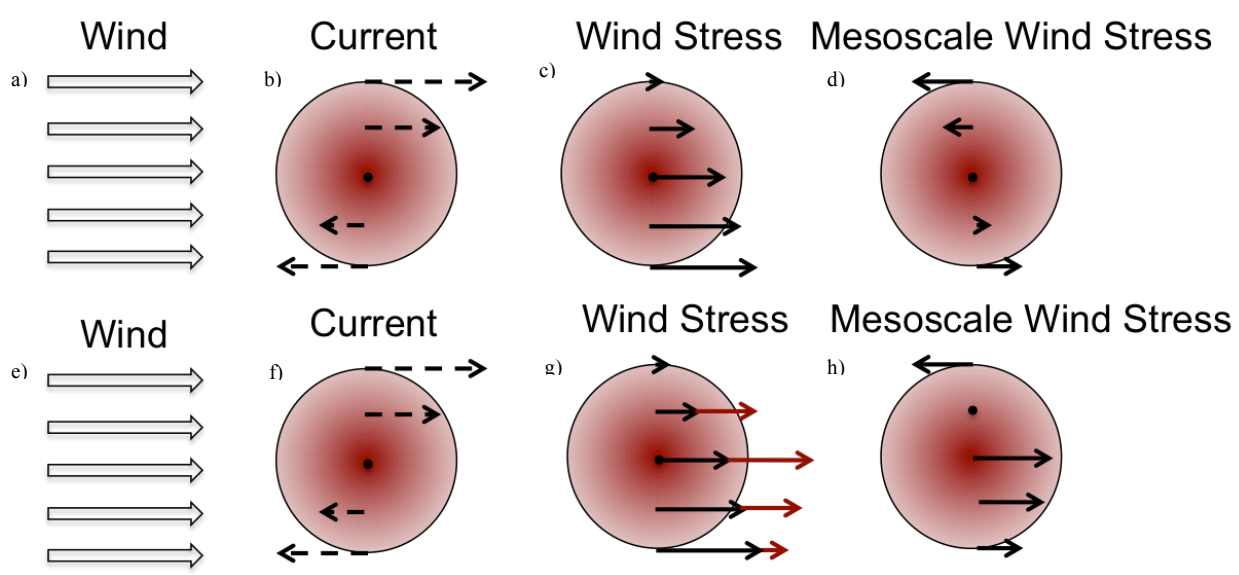

FIG. 3.13. Illustration of how OME-A feedback affects mesoscale wind stress structure over an anticyclonic warm eddy in the northern hemisphere. The upper panel shows patterns without OME-A feedback, and the lower panel includes the feedback. Circles with red center indicate the anticyclonic warm eddies. Hollow arrows represent large-scale background wind speed blowing over the eddies. Dashed arrows are eddy currents. Considering currents effects only, the structure of total wind stress is shown as figure c, while including the OME-A feedback, the total wind stress is adjusted from figure c to figure g as shown by the red arrows. After applying spatial filter, patterns of mesoscale wind stress are shown in figure d and h without and with OME-A feedback.

3.5.3 Wind Stress Response

As mentioned earlier, the reduction in eddy wind power caused by OME-A feedback is mainly caused by the change in mesoscale wind stress, which is illustrated in Figure 3.13. Taking anticyclonic warm eddies as an example. In the smoothed simulations, total wind stress is determined by the relative motion between wind speed and ocean surface currents. On the northern side of the eddies, wind speed blows in the same direction as eddy current leading to a smaller wind stress, while on the southern side of the eddies, wind blows in the opposite direction with eddy current leading to a larger wind stress.

The smaller stress to the north exerts a weaker friction on the winds, so that the winds can further increase, which in turn increase the stress. Therefore, there is feedback between the winds and current. Similar feedback occurs in the southern side. Upon removing the large scale background wind stress (Fig. 3.13a), the resultant mesoscale wind stress (Fig. 3.13d) always opposes the eddy current (Fig. 3.13b), which leads to the negative eddy wind power with maximum values occurring in the eddy edge where both the magnitudes of mesoscale wind stress and eddy current velocity are the largest, and the minimum values occurring near the eddy center. In the control simulations, besides the ocean current effect, wind stress can also be affected by the eddy-induced SSTs. Over warm eddies, wind speed increases near eddy center leading to an enhanced total wind stress there. After removing the large-scale background wind stress (Fig. 3.13e), the maximum mesoscale wind stress occurs near the eddy center (Fig. 3.13h). This change in wind stress structure leads to the decrease of eddy wind power when including the OME-A interactions.

3.5.4 Response Difference between Winter and Summer

Satellite observations suggest that during winter when OME-A interactions are strongest (e.g. Putrasahan et al. 2013), VMM tends to dominate (Frenger et al. 2013), but during summer PAM becomes more dominant (Ma et al. 2016). This difference in surface wind response to eddy-induced SSTs leads to different impact of OME-A feedback on ocean eddy wind power between winter and summer. As explained earlier,

when VMM dominants, maximum eddy-SST induced wind anomaly tends to locate near eddy center where the eddy currents velocity is zero, rather than along eddy edge when PAM dominants. This raises the possibility that the strength of OME-A feedback on wind power is weaker during summer than winter The extent to which these seasonal variations of OME-A feedback can have an impact on wind power has not been fully investigated.

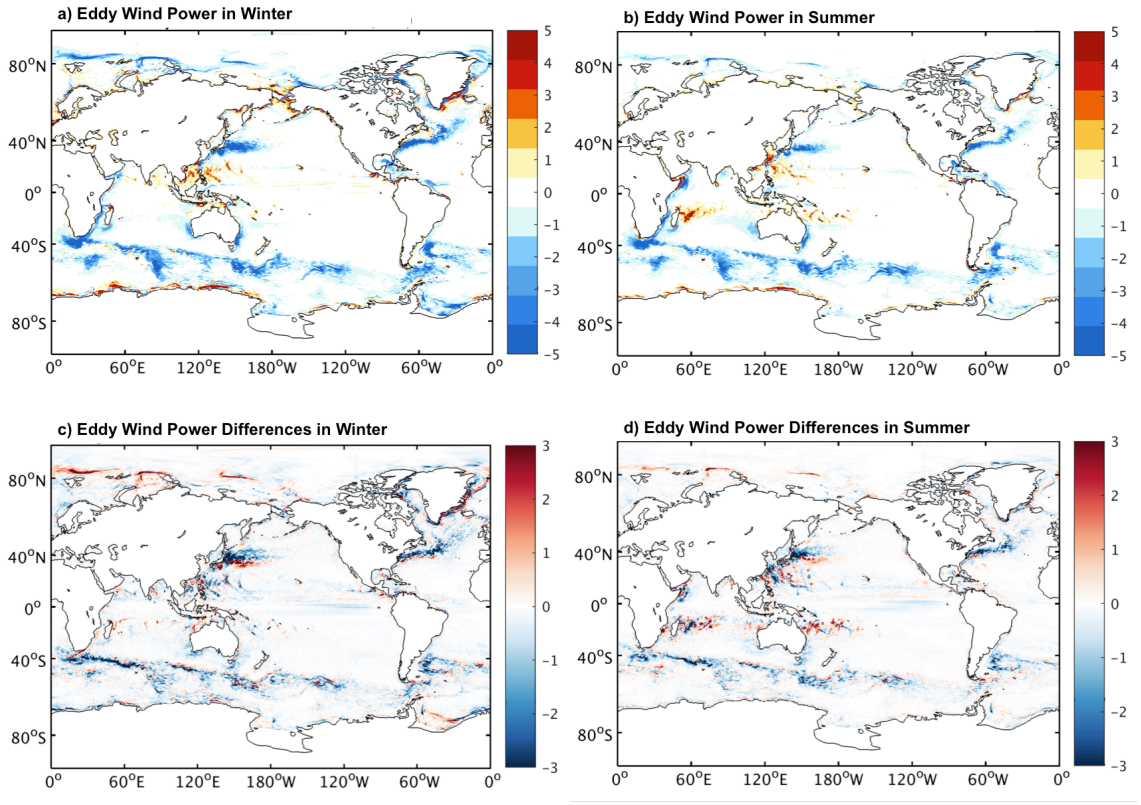

FIG. 3.14. Mean eddy wind power (mW/m^{-2}) derived from CESM simulations during winter (a) and summer (b), and difference between smoothed and control simulations (smoothed-control) in winter (c) and summer (d).

Here, we studied the influence of OME-A feedback on eddy wind power in summer and winter separately using CESM simulations. The winter season is defined for the

months from November to March (NDJFM) for the northern hemisphere and from May to September (MJJAS) for the southern hemisphere, and the summer season is defined for the months from May to September (MJJAS) for the northern hemisphere and from November to March (NDJFM) for the southern hemisphere. From the control simulations, eddy wind power always acts to damp the ocean eddies, but is much stronger in winter than summer (Figure 3.14a, b). And in comparison with the control simulations, the sink effect of eddy wind power in the smoothed simulations is more overestimated in winter than summer (Figure 3.14c, d), suggesting the effects of OME-A feedback on wind power is stronger in winter than summer. In the northern hemisphere, the reduction of eddy wind power in the control simulations compared to smoothed simulations is ~50% in winter and ~40% in summer, while in the southern hemisphere, it is ~30% in winter and ~24% in summer.

To better understand this seasonal variation, investigations into individual eddies in summer are performed. Figure 3.15 shows the comparisons of eddy wind power between summer and winter in Kuroshio Extension. Consistent with Figure 3.14, eddy wind power sinks the eddy energy in winter and summer, and during winter the sink is stronger than summer. In summer, after including the OME-A feedback, the area averaged eddy wind power within the 2-eddy-radius box reduces by about 28% (29%) over anticyclonic eddies and by about 27% (26%) over cyclonic eddies over Kuroshio Extension (Gulf Stream). And over Gulf Stream, the corresponding values are 31% (32%) and 23% (27%) over the Brazil-Malvinas Confluence (Agulhas Return Current). The reduction effects are

always smaller in summer than in winter. The composite maps of eddy currents and mesoscale wind stress show similar structures as in winter (not shown).

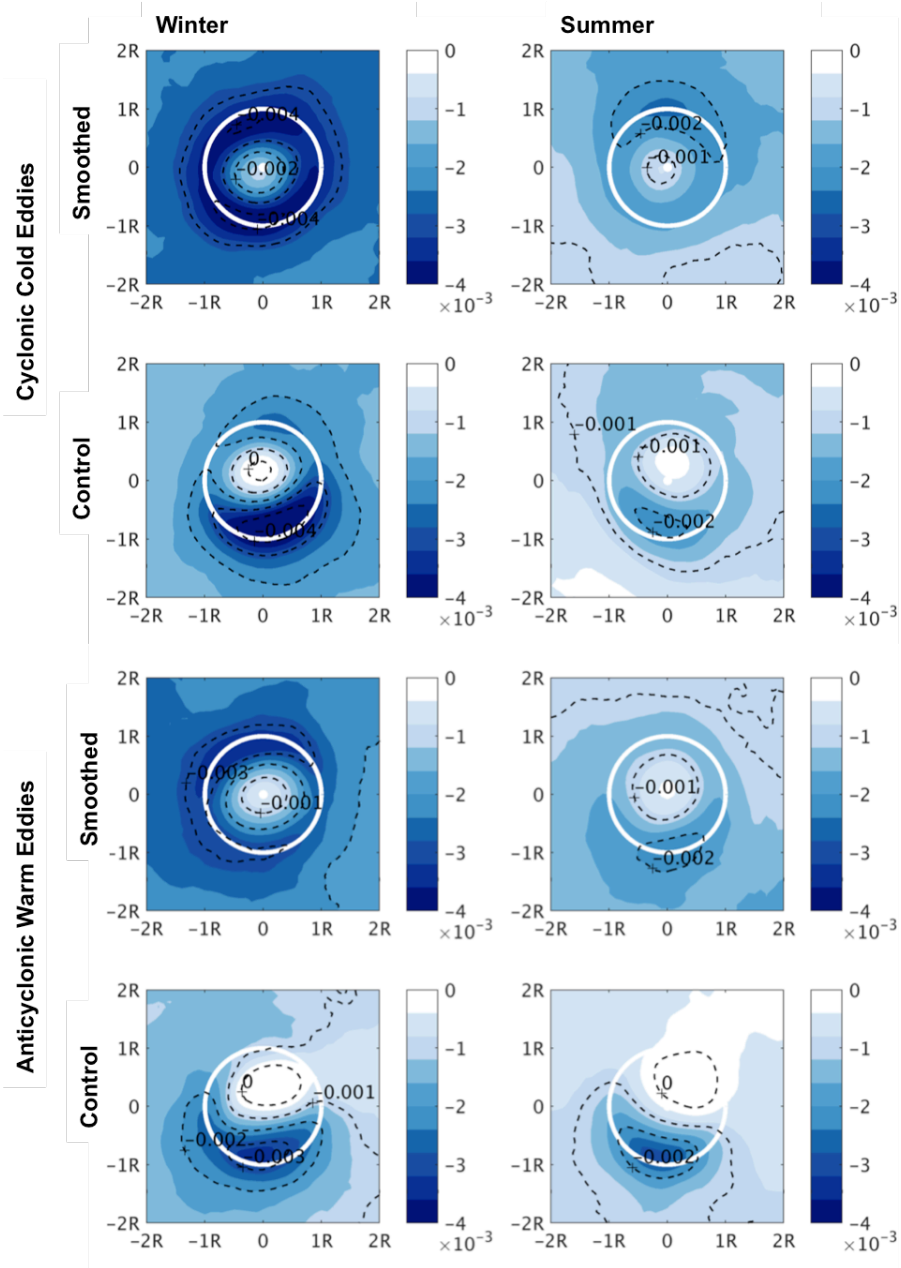

FIG. 3.15 Comparisons of eddy wind power (W/m^2) in winter (left panel) and summer (right panel) over cyclonic cold eddies (Upper two panels) and anticyclonic warm eddies (lower two panels) in Kuroshio Extension from CRCM smoothed (the first and third panel) and control (the second and forth panel) simulations.White contour and dot mark one eddy radius and eddy center.

3.6 Summary

For large-scale ocean circulation, wind stress acts as an energy source to transfer atmospheric kinetic energy into the ocean by working on the ocean currents. However, at ocean mesoscales, wind power changes its sign from positive to negative, and works to sink the EKE. We refer this negative wind power as to the eddy wind power. It is largely caused by the relative motion between winds and ocean eddy circulation, which has been referred to as the ocean current feedback (Renault et al. 2016), but we demonstrate that it can also be influenced by OME-A feedback especially in the western boundary currents regions and in the southern oceans where eddies are energetic. Both the scaling analysis and the coupled climate model simulations demonstrate the impact of OME-A feedback is smaller than the effect of ocean currents, but is still important in influencing the sink effect of the eddy wind power. Without considering OME-A feedback, eddy wind power is shown to be overestimated, suggesting that the previous estimate of sink of EKE by wind power may be too large. And this result holds in both summer and winter and for both anticyclonic warm eddies and cyclonic cold eddies. From the model simulations, OME-A feedback on wind power is stronger in winter than in summer for both the northern and southern hemisphere. Interestingly, there appears to be an asymmetry between strength of eddy wind power response to warm *vs*. cold eddies; the impact of OME-A feedback on eddy wind power is more effective for the former than the latter. This is in line with the notion that OME-A interactions are stronger over warm eddies than cold eddies due to nonlinear process with the atmospheric planetary boundary layer.

The mechanism for OME-A feedback to affect eddy wind power is explored in this study. Increased (decreased) wind speed over warm (cold) eddies modify the wind stress over eddies. Including OME-A feedback causes the maximum values of mesoscale wind stress to move from the eddy edge towards the eddy center where the eddy current velocity is near zero. Since the production of eddy current and wind stress is close to zero near the eddy center the large value of wind stress makes no contribution to the wind power. As a result, the integrated eddy wind power over the eddies tends to be always smaller when the OME-A interaction is included.

This study quantifies the relative importance between the ocean current feedback and the OME-A feedback impact in eddy wind power and advances our understanding of the OME-A feedback on eddy energetics. This improved understanding of physical processes governing eddy energetics will lead to improvements in ocean and climate models.

CHAPTER IV

CONCLUSIONS AND FUTURE WORK

In this dissertation, OME-A interaction over extratropical oceanic frontal zones, encompassing the Gulf Stream, Kuroshio, Agulhas Return Current and Brazil-Malvinas Confluence, where energetic ocean eddies reside, are studied from two perspectives.

First, using three multi-sensor based satellite rainfall observations, TMPA, CMORPH and IMERG, precipitation response to ocean mesoscale eddies are examined and compared. The three satellite products are validated against the *in situ* measurement from the KEO mooring located in the Kuroshio Extension of the Northwestern Pacific Ocean. Different rainfall response strength to ocean eddies is found among different datasets and the underlying reason for the difference is explored. We also investigated the response difference between summer and winter, and between warm and cold eddies. The statistical robustness of the results is validated by comparing the analyses between the 11-year rainfall observation that covers the entire record length of TMPA and CMORPH and the short overlapping period shared by the three datasets.

Second, we explored the effect of OME-A feedback on eddy wind power through a scaling analysis and analysis of two sets of high-resolution coupled model experiments using both a regional (CRCM) and a global (CESM) climate models. The two sets of model experiments are nearly identical except that in the smoothed simulations,a spatial low-pass filter was applied to the modeled SST before passed to the atmosphere at each

coupling step. As such, the smoothed simulations suppressed the OME-A interaction. No such a filter was used in the control simulations, so that OME-A interaction is retained. Comparisons between control and smoothed simulations allow us to assess the impact of OME-A feedback on eddy wind power. The main conclusions of these two studies are summarized as follows.

4.1 Conclusions

Over 165,000 ocean mesoscale eddy snapshots were identified using satellite altimetry in the four most eddy-energetic regions of the ocean during the overlapped period from April 2014 to January 2016 of the three satellite rainfall datasets. Rainfall composites over these eddies show coherent enhanced rain rate over warm eddies and reduced rain rate over cold eddies. Among the three products, CMORPH exhibits similar mean rainfall to TMPA but the weakest rainfall response to ocean eddies than the other two products, while IMERG reveals the weakest mean rainfall but the strongest and most coherent rainfall responses to ocean eddies. This suggests that the mean rainfall strength has little direct bearing on the response strength to ocean eddies. The weakest rainfall response to ocean eddies in CMORPH may be caused by its morphing technique which tends to underestimate rainfall responses if eddies reside over areas between the paths of passive microwave instruments. Further analyses suggest that neither the enhanced resolution nor the wider range of rain type in IMERG contribute directly to the stronger rainfall response than the other two datasets. This leads to the conclusion that

improvements in passive microwave sensors and algorithms in IMERG are more likely to play a vital role in the improving rainfall response signal over ocean eddies

Validation against the KEO buoy rainfall measurement located in the Kuroshio Extension region shows that the newly available high-resolution rainfall product, IMERG, has the smallest systematic errors in not only the mean rainfall measurement but also the distribution of rain rate This indicates that IMERG is highly valuable for validating climate model simulations and advancing our understanding in air-sea interactions at oceanic mesoscales.

IMERG reveals a more distinctive seasonal asymmetry in rainfall response to oceanic eddies than other two rainfall datasets, with stronger response in winter than summer. The stronger rainfall response is only partially attributed to the larger eddy-induced SSTs in winter, the more responsive atmosphere also plays an important role in generating the stronger response in winter. During winter, the atmosphere is unstable due to the larger air-sea temperature differences over the oceanic frontal zones, and the frequent passage of cold air outbreaks that have the cold air above the warm ocean fronts, reducing the stability of the atmosphere. Thus the atmosphere is more sensitive to SST perturbations resulting in enhanced OME-A interactions in winter. This reasoning is also consistent with our analyses of the rainfall response for different rain types. By grouping precipitation into three types, light, moderate and heavy rain, it is found that rainfall response to ocean eddies increases as rain rate increases. This supports

the notion that the interaction between atmospheric synoptic storms and ocean mesoscale eddies during winter is of importance.

IMERG also reveals a more clear asymmetry of rainfall responses to warm *vs*. cold eddies. The atmosphere is more responsive to warm eddies than cold ones, leading to large rainfall anomalies over warm eddies than cold eddies. As a result, there is a non-zero net impact of ocean eddies on large-scale moisture budget within the PBL and the lower atmosphere. It implies that mesoscale SSTs have the potential to modulate the large-scale atmospheric circulations by affecting lower atmosphere and marine boundary layer moisture budget, which in turn may affect cyclogenesis and storm tracks.

OME-A feedback also influences the energetics of ocean circulation. Wind power is a measure of kinetic energy exchange between the ocean and the atmosphere by winds working on surface currents. Before the satellite era, due to the limited spatial and temporal resolutions of the global measurements, only large-scale wind power can be estimated. It is shown that the large-scale wind power provides a primary energy source to drive large-scale ocean circulations. In recent years, advancements in satellite observations allow us to measure surface geostrophic currents and wind stress in high resolutions, making it possible to study the small-scale wind power. The majority of this small-scale wind power is related to ocean eddies, and thus it is referred to as the eddy wind power in this study. It is mainly caused by ocean currents' feedback on wind stress and acts to sink EKE. Although OME-A interaction suggests that both wind speed and

wind stress above eddies are influenced by eddy-induced SSTs, whether it can significantly affect the wind work input into the ocean eddies remains unquantified .

The scaling analysis and the coupled climate model simulations both demonstrate OME-A feedback can have a sizable impact on eddy wind power acting to reduce its sink effect on EKE, although the amplitude of this impact on eddy wind power is smaller than that due to ocean current feedback. Without considering OME-A interaction, eddy wind power sink is overestimated by about 31% in CRCM and about 48% in CESM. This overestimation in eddy wind power holds in both summer and winter and for both anticyclonic warm eddies and cyclonic cold eddies. Again, an asymmetry is revealed in eddy wind power between winter and summer and between warm and cold eddies. OME-A feedback is stronger in winter than in summer and is more effective for the warm eddies than the cold eddies. These are in agreements with our previous analysis of rainfall response that the atmosphere is more responsive to SST perturbations in winter and OME-A interaction is stronger over warm eddies than cold eddies due to non-linear atmospheric PBL processes.

We also explored how eddy wind power is affected by OME-A feedback by compositing the mesoscale wind stress and currents above eddies. The change in wind structure above eddies due to OME-A feedback is the key process responsible for the modification in the eddy wind work. Without OME-A feedback, structure of the wind stress above eddies is determined by eddy current with its maximum values occurring along eddy edges. However, when OME-A feedback is included, wind speeds increase

over warm eddies and decrease over cold eddies near their core. The maximum wind stress above eddies moves toward the eddy center, where the current velocity is zero. And eddy wind power, which is the dot product of mesoscale wind stress and eddy currents, yields a smaller value. As a result, the integral of wind power over individual eddy decreases when OME-A feedback is present.

Based on our analyses, we advocate that understanding the elements of OME-A interaction and its feedback are important for understanding both atmospheric and oceanic large-scale circulations.

4.2 Future Work

The asymmetry between rainfall response to warm and cold eddies revealed by our study suggests that ocean eddy forcing may exert an influence on large-scale atmospheric circulation by affecting lower atmosphere and PBL moisture budget. Both high-resolution satellite measurements and regional climate models (Willison et al., 2013; Ma et al., 2015b; 2017) demonstrate that eddy-induced SSTs forcing affects cyclogenesis and storm track through moist baroclinic instability. These findings point to the potential of improving forecasts of winter storm systems by resolving ocean mesoscale eddies and their interactions with the atmosphere. Further studies are needed to test whether forecast skills of weather variability on subseasonal time scales can be improved by including OME-A interactions properly.

Recent studies (e.g., Ma et al. 2016, Renault et al., 2016) show that mesoscale eddies can play an important role in modulating large-scale ocean circulations through their interactions with the atmosphere in frontal regions, such as the Kuroshio Extension Region and Gulf Stream Extension Region. To understand the mechanisms, effect of OME-A feedback on eddy potential energy budget has been analyzed (Ma et al. 2016). Our study indicates eddy wind power, which is an important part in eddy kinetic energy budget, is decreased when including OME-A feedback in the eddy-resolving model simulations. Further detailed diagnostic analyses of ocean eddy kinetic energy budget are needed to assess the importance of OME-A feedback on both eddy potential and kinetic energy budget.

This dissertation mainly focus on the extratropical warm frontal zones where eddies are energetics and OME-A interactions are strong. However, positive correlations between mesoscale SST and wind speed anomalies are also found along equatorial cold tongues where Legeckis eddies or Tropical Instability Waves cause strong mesoscale SST variability. The physical processes behind mesoscale air-sea interactions over these different regions need to be further explored and compared.

REFERENCES

Adler, R. F., C. Kidd, G. Petter, M. Morissey, and H. M. Goodman, 2001: Intercomparison of global precipitation products: The Third Precipitation Intercomparison Project (PIP-3), *Bull. Amer. Meteor. Soc.*, **82**, 1377-1396

Arkin, P. A., and P. Xie, 1994: The Global Precipitation Climatology Project: first algorithm intercomparison project, *Bull. Amer. Meteor. Soc.*, **75**, 401-419, doi: 10.1175/1520-0477(1994)075<0401:TGPCPF>2.0.CO;2.

Barsugli, J. J., and Battisti D. S., 1998: The basin effects of atmosphere-ocean thermal coupling on midlatitude variability, *J. Atmos. Sci.*, **55**, 477-493.

Byrne, D., L. Papritz, I. Frenger, M. Münnich, and N. Gruber, 2015: Atmospheric response to mesoscale sea surface temperature anomalies: assessment of mechanisms and coupling strength in a high-resolution coupled model over the south Atlantic, *J. Atmos. Sci.*, **72**, 1872-1890, doi: 10.1175/JAS-D-14-0195.1.

Byrne, D., M. Münnich, I. Frenger and N. Gruber, 2016: Mesoscale atmosphere ocean coupling enhances the transfer of wind energy into the ocean. *Nat. Commun.*, **7**, 11867.

Chelton, D. B., 2013: Ocean-atmosphere coupling: mesoscale eddy effects, *Nature Geosci.*, **6**, 594-595, doi: 10.1038/ngeo1906.

Chelton, D. B., M. G. Schlax, M. H. Freilich, and R. F. Milliff, 2004: Satellite measurements reveal persistent small-scale features in ocean winds, *Science*, **303**, 978-983, doi: 10.1126/science.1091901.

Chelton, D. B, M. G. Schlax, R. M. Samelson, and R. A. de Szoeke, 2007: Global observations of large oceanic eddies, *Geophys. Res. Lett.,* **34**, L15606, doi: 10.1029/2007GL030812.

Chelton, D. B, M. G. Schlax, and R. M. Samelson, 2011: Global observations of nonlinear mesoscale eddies, *Prog. Oceanogr.,* **91**, 167-216, doi: 10.1016/j.pocean.2011.01.002.

Chelton, D. B., and S.-P. Xie, 2010: Coupled ocean-atmosphere interaction at oceanic mesoscales, *Oceanography*, **23**, 52-69, doi: 10.5670/oceanog.2010.05.

Chen, R., 2013: Energy pathways and structures of oceanic eddies from the ECCO2 state estimate and simplified models. *Diss. Massachusetts Institute of Technology*.

Dawe J. T., and L. Thompson, 2006: Effect of ocean surface currents on wind stress, heat flux and wind power input to the ocean. *Geophys. Res. Lett.,* **33***,* L09604.

Duhaut T. H. A., and D. N. Straub, 2006: Wind stress dependence on ocean surface velocity: implications for mechanical energy input to ocean circulation. *J. Phys. Oceanogr.*, **36***,* 202-211.

Ebert E. E., J. E. Janowiak, C. Kidd, 2007: Comparison of near-real-time precipitation estimates from satellite observations and numerical models, *Bull. Amer. Meteor. Soc.*, **88**, 47-64, doi: 10.1175/BAMS-88-1-47

Eden, C., and H. Dietze, 2009: Effects of mesoscale eddy/wind interactions on biological new production and eddy kinetic energy. *J. Geophys. Res.*, **114**, C05023.

Ferrari, R. and C. Wunsch, 2009: Ocean circulation kinetic energy: Reservoirs, sources, and sinks. *Annu. Rev. Fluid Mech.,* **41***,* 253–282.

Ferrari, R. and C. Wunsch, 2010: The distribution of eddy kinetic and potential energies in the global ocean. *Tellus,* **62A***,* 92-108.

Flierl. G. R., 1977: The application of linear quasigeostrophic dynamics to Gulf Stream rings. *J. Phys. Oceanogr.*, **7**, 365-379.

Fofonoff, N. P., 1981: The Gulf Stream system. *Evolution of Physical Oceanography. Scientific Surveys in Honor of Henry Stommel*, B. A. Warren and C. Wunsch, Eds., The MIT Press, 112-139.

Frenger, I., N. Gruber, R. Knutti, and M. Münnich, 2013: Imprint of Southern Ocean eddies on winds, clouds and rainfall, *Nat. Geosci.*, **6**, 608-612, doi: 10.1038/ngeo1863.

Gaube, P., D. B. Chelton, R. M. Samelson, M. G. Schlax, and L. W. O'Neill, 2014: Satellite observations of mesoscale eddy-induced Ekman pumping, *J. Phys. Oceanogr.*, **45***,* 104-132.

Gill, A. E., J. S. A. Green, and A. J. Simmons, 1974: Energy partition in the large-scale ocean circulation and the production of mid-ocean eddies, *Deep Sea Res.,* **21**, 499-528

Griffies, S. M., M. Winton, W. G. Anderson, R. Benson, T. L. Delworth, C. O. Dufour, J. P. Dunne, P. Goddard, A. K. Morrison, A. Rosati, A. T. Wittenberg, J. Yin and R. Zhang, 2015: Impacts on ocean heat from transient mesoscale eddies in a hierarchy of climate models, *J. Clim.*, **28,** 952-977, doi: 10.1175/JCLI-D-14-00353.1

Grooms, I., L.-P. Nadeau, and K. S. Smith, 2013: Mesoscale eddy energy locality in an idealized ocean model, *J. Phys. Oceanogr.*, **43***,* 1911-1923.

Hawcroft, M., K., L. C. Shaffrey, K. I. Hodges and H. F. Dacre, 2012: How much Northern Hemisphere precipitation is associated with extratropical cyclones?, *Geophys. Res. Lett.,* **39**, L24809, doi: 10.1029/2012GL053866

He, Z., L. Yang, F. Tian, G. Ni, A. Hou, and H. Liu, 2016: Intercomparison of rainfall estimates from the TRMM and GPM multi-satellite products over the Upper Mekong River Basin, *J. Hydrometeor.,* **18**, 413-430, doi: 10.1175/JHM-D-16-0198.1

Hou, A. Y., and Coauthors, 2014: The global precipitation measurement mission, *Bull. Amer. Meteor. Soc.*, **95**, 701-722 doi: 10.1175/BAMS-D-13-00164.1.

Huffman, G. J., R. F. Adler, D. T. Bolvin, G. Gu, E. J. Nelkin, K. P. Bowman, Y. Hong, E. F. Stocker and D. B. Wolff, 2007: The TRMM Multisatellite Precipitation

Analysis (TMPA): Quasi-global, multiyear, combined-sensor precipitation estimates at fine scales, *J. Hydrometeor.,* **8**, 38-55, doi: 10.1175/JHM560.1.

Huffman, G. J., R. F. Adler, D. T. Bolvin, and E. J. Nelkin, 2010: The TRMM Multisatellite Precipitation Analysis (TMPA), *Satellite rainfall applications for surface hydrology*, F. Hossain and M. Gebremichael, Eds., Springer-Verlag, 3-22.

Huffman, G. J., Pendergrass, Angeline & National Center for Atmospheric Research Staff (Eds), Last modified 02 May 2015a: The Climate Data Guide: TRMM: Tropical Rainfall Measuring Mission (available at https://climatedataguide.ucar.edu/climate-data/trmm-tropical-rainfall-measuring-mission).

Huffman, G. J., D. T. Bolvin, D. Braithwaite, K. Hsu, R. Joyce, C. Kidd, E. J. Nelkin and P. Xie, 2015b: NASA Global Precipitation Measurement (GPM) Integrated Multi-satellite Retrievals for GPM (IMERG), *Algorithm Theoretical Basis Doc.*, version 4.5, 26pp (available at https://pmm.nasa.gov/sites/default/files/document_files/IMERG_ATBD_V4.5_0.pdf).

Huffman, G. J., D. T. Bolvin and E. J. Nelkin, 2015c: Integrated Multi-satellite Retrievals for GPM (IMERG) technical documentation, *NASA Doc.*, 47 pp (available at https://pmm.nasa.gov/sites/default/files/document_files/IMERG_doc.pdf).

Huffman, G. J., D. T. Bolvin and E. J. Nelkin, 2015d: Day 1 IMERG final run release notes. *NASA Doc.*, 47 pp (available at https://pmm.nasa.gov/sites/default/files/document_files/IMERG_FinalRun_Day1_release_notes.pdf).

Hughes C. W. and C. Wilson, 2008: Wind work on the geostrophic ocean circulation: an observational study of the effect of small scales in the wind stress. *J. Geophys. Res.*, **113**, C02016.

Jin, X., C. Dong, J. Kurian and J. C. McWilliams, 2009: SST-wind interaction in coastal upwelling: oceanic simulation with empirical coupling, *J. Phys. Oceanogr.*, **39**, 2957-2970.

Joyce, R. J., J. E. Janowiak, P. A. Arkin, and P. P. Xie, 2004: CMORPH: A method that produces global precipitation estimates from passive microwave and infrared data at high spatial and temporal resolution, *J. Hydrometeor.,* **5**, 487-503, doi: 10.1175/1525-7541(2004)005<0487:CAMTPG>2.0.CO;2.

Kidd, C., D. R. Kniveton, M. C. Todd, and T. J. Bellerby, 2003: Satellite rainfall estimation using combined passive microwave and infrared algorithms, *J. Hydrometeor.,* **4**, 1088-1104

Kurian, J., F. Colas, X. Capet, J. C. McWilliams, and D. B. Chelton, 2011: Eddy properties in the California current system, *J. Geophys. Res.*, **116**, C08027, doi: 10.1029/2010JC006895.

Kwon, Y.-O., M. A. Alexander, N. A. Bond, C. Frankignoul, H. Nakamura, B. Qiu and L. A. Thompson, 2010: Role of the Gulf Stream and Kuroshio-Oyashio systerms in large-scale atmosphere-ocean interaction: a review. *J. Clim.*, **23,** 3249-3281, doi: 10.1175/2010JCLI3343.1

LaCasce, J. H., and J. Pedlosky, 2004: The instability of Rossby basin modes and the oceanic eddy field, *J. Phys. Oceanogr.*, **34**, 2027-2041.

Liu, Z., 2016: Comparison of Integrated Multisatellite Retrievals for GPM (IMERG) and TRMM Multisatellite Precipitation Analysis (TMPA) monthly precipitation products: initial results, *J. Hydrometeor.*, **17**, 777-790, doi: 10.1175/JHM-D-15-0068.1.

Lorenz, E. N., 1955: Available potential energy and the maintenance of the global circulation. *Tellus*, **7**, 157-167.

Luo, J., S. Masson, E. Roeckner, G. Madec, and T. Yamagata, 2005: Reducing climatology bias in an ocean-atmosphere CGCM with improved coupling physics, *J. Climate*, **18***,* 2344–2360, doi: 10.1175/JCLI3404.1.

Lueck, R., and R. Reid, 1984: On the production and dissipation of mechanical energy in the ocean. *J. Geophys. Res.*, **89**, 3439–3445.

Ma, J., H. Xu, C. Dong, P. Lin, and Y. Liu, 2015a: Atmospheric responses to oceanic eddies in the Kuroshio Extension region, *J. Geophys. Res*., **120**, 6313-6330, doi: 10.1002/2014JD022930.

Ma, X., P. Chang, R. Saravanan, R. Montuoro, J. Hsieh, D. Wu, X. Lin, L. Wu and Z. Jing, 2015b: Distant influence of Kuroshio eddies on north pacific weather patterns?, *Sci. Rep.,* **5**, 17785, doi: 10.1038/srep17785.

Ma, X., Z. Jing, P. Chang, X. Liu, R. Montuoro, R. J. Small, F. O. Bryan, R. J. Greatbatch, P. Brandt, D. Wu, X. Lin and L. Wu, 2016: Western boundary currents regulated by interaction between ocean eddies and the atmosphere, *Nature*, **535**, 533-537, doi:10.1038/nature18640.

Ma, X., P. Chang, R. Saravanan, R. Montuoro, H. Nakamura, D. Wu, X. Lin and L. Wu, 2017: Importance of resolving Kuroshio front and eddy influence in simulating the north Pacific strom track, *J. Clim.*, **30**, 1861-1880, doi: 10.1175/JCLI-D-16-0154.1

Maltrud, M. E. and J. L. McClean, 2005: An eddy resolving global 1/10 ocean simulation, *Ocean Modeling*, **8**, 31-54, doi: 10.1016/j.ocemod.2003.12.001

McWilliams, J. C., W. R. Holland, and J. S. Chow, 1978: A description of numerical Antarctic Circumpolar currents, *Dyn. Atmos. Oceans*, **2**, 213-291

Minobe, S., A. Kuwano-Yoshida, N. Komori, S.-P. Xie, and R. J. Small, 2008: Influence of the Gulf Stream on the troposphere, *Nature*, **452**, 206-209, doi: 10.1038/nature06690.

Minobe, S., M. Miyashita, A. Kuwano-Yoshida, H. Tokinaga and S.-P. Xie, 2010: Atmospheric response to the Gulf Stream: seasonal variations, *J. Clim.*, **23**, 3699-3719, doi: 10.1175/2010JCLI3359.1

Morrow, R. & Le Traon, P.-Y., 2012: Recent advances in observing mesoscale ocean dynamics with satellite altimetry, *Adv. Spa. Res.,* **50**, 1062-1076

O' Neill, L. W., D. B. Chelton, S. K. Esbensen and F. J. Wentz, 2005: High-resolution satellite measurments of the atmospheric boundary layer response to SST variations along the Agulhas Return Current, *J. Clim.*, **18**, 2706-2723, doi: 10.1175/JCLI3415.1.

O' Neill, L. W., D. B. Chelton and S. K. Esbensen, 2010: The effects of SST-induced surface wind speed and direction gradients on midlatitude surface vorticity and divergence, *J. Clim.*, **23**, 255-281, doi: 10.1175/2009JCLI2613.1.

O' Neill, L. W., D. B. Chelton and S. K. Esbensen, 2012: Covariability of surface wind and stress responses to sea surface temperature fronts, *J. Clim.*, **25**, 5916-5942, doi: 10.1175/JCLI-D-11-00230.1

O' Neill, L. W., T. Haack, D. B. Chelton and E. Skyllingstad, 2017: The Gulf Stream convergence zone in the time-mean winds, *J. Atmos. Sci.*, **74**, 2383-2412, doi: 10.1175/JAS-D-16-0213.1.

Oort, A. H., L. A. Anderson, and J. P. Peixoto, 1994: Estimates of the energy cycle of the oceans. *J. Geophys. Res.*, **99**, 7665–7688.

O' Reilly, C. and A. Czaja, 2015: The response of the pacific storm track and atmospheric circulation to Kuroshio Extension variability, *Q. J. Roy. Meteor. Soc.*, **141**, 52-66, doi: 10.1002/qj.2334

O' Reilly, C., M. Minobe, A. Kuwano-Yoshida and T. Woollings, 2017: The Gulf Stream influence on wintertime north Atlantic jet variability, *Q. J. Roy. Meteor. Soc.*, **143**, 173-183, doi: 10.1002/qj.2907

Pacanowski, R., 1987: Effect of equatorial currents on surface stress, *J. Phys. Oceanogr.*, **17***,* 833-838, doi: 10.1175/1520-0485(1987)017

Park, K.-A., P. Cornillon, D. L. Codiga, 2006: Modification of surface winds near ocean fronts: Effects of Gulf Stream rings on scatterometer (QuikSCAT, NSCAT) wind observations, *J. Geophys. Res.*, **111**, C3, doi: 10.1029/2005JC003016.

Prakash, S., A. K. Mitra, D. S. Pai and A. AghaKouchak, 2016: From TRMM to GPM: how well can heavy rainfall be detected from space?, *Adv. Water Resour.,* **88**, 1-7, doi: 10.1016/j.advwatres. 2015.11.008

Putrasahan, D. A., A. J. Miller and H. Seo, 2013: Isolating mesoscale coupled ocean-atmosphere interactions in the Kuroshio Extension region, *Dyn. Atmos. Ocean.*, **63**, 60-78, doi:10.1016/j.dynatmoce.2013.04.001.

Picot, N., K. Case, S. Desai, and P. Vincent, 2003: AVISO and PODAAC User Handbook, IGDR and GDR Jason Products, *SMM-MU-M5-OP-13184-CN (AVISO), JPL D-21352 (PODAAC),* Jet Propul. Lab., Calif. Inst. Of Technol., Pasadena, Calif. (Available at http://podaac.jpl.nasa.gov/jason/documents/Handbook_Jason.pdf).

Renault, L., and Coauthors, 2016: Modulation of Wind-Work by Oceanic Current Interaction with the Atmosphere. *J. Phys. Oceanogr.*, **46**, 1685-1704.

Salmon, R., 1978: Two-layer quasigeostrophic turbulence in a simple special case. *Geophys. Astrophys. Fluid Dyn.*, **10**, 25-52.

Scott, R. B., 1999a: Geostrophic energetics and the small viscosity behaviour of an idealized ocean circulation model. *Ph.D. dissertation, McGill University*, 124 pp. *[Available from Schulich Library of Science and Engineering, Macdonald Stewart Library Building, McGill University, 809 Sherbrooke St. West, Montreal, QC H3A 2K6, Canada.]*.

Scott, R. B., 1999b: Mechanical energy flux to the surface geostrophic flow using TOPEX/Poseidon data. *23d EGS General Assembly*, Nice, France, European Geophysical Society, 399–402.

Scott, R. B. and F. Wang, 2005: Direct evidence of an oceanic inverse kinetic energy cascade from satellite altimetry. *J. Phys. Oceanogr.*, **35**, 1650-1666

Scott, R.B. and Xu, Y., 2009: An update on the wind power input to the surface geostrophic flow of the World Ocean. *Deep-Sea Res. Part I*, **56***,* 295-304.

Seo, H., A. J. Miller, and J. R. Norris, 2016: Eddy–wind interaction in the California Current System: Dynamics and impacts. *J. Phys. Oceanogr.*, **46***,* 439–459.

Seo, H., 2017: Distinct influence of air-sea interactions mediated by mesoscale sea surface temperature and surface current in the Arabian Sea. *J. Climate,* **30***,* 8061-8080

Serra, Y. L., M. J. Mcphaden, 2003: Multiple time- and space-scale comparisons of ATLAS Buoy rain gauge measurements with TRMM satellite precipitation measurements, *J. Appl. Meteorol.*, **42**, 1045-1059, doi: 101175/1520-0442(2002)015<0983:DVOTRR>2.0.CO;2.

Small, R. J., S. P. deSzoeke, S.-P. Xie, L. O'Neill, H. Seo, Q. Song, P. Cornillon, M. Spall, S. Minobe, 2008: Air-sea interaction over ocean fronts and eddies, *Dyn. Atmos. Oceans.*, **45**, 274-319, doi: 10.1016/j.dynatmoce.2008.01.001.

Small, R. J., et al., 2014: A new synoptic scale resolving global climate simulation using the Community Earth Systerm Model. *J. Adv. Model. Earth Syst.*, **6**, 1065-1094, doi: 10.1002/2014MS000363

Tang, G., Y. Ma, D. Long, L. Zhong, and Y. Hong, 2016: Evaluation of GPM Day-1 IMERG and TMPA Version-7 legacy products over mainland China at multiple spatiotemporal scales, *J. Hydrol.,* **533**, 152-167, doi: 10.1016/j.jhydrol.2015.12.008

Tokinaga, H., Y. Tanimoto, and S.-P. Xie, 2005: SST-induced surface wind variations over the Brazil-Malvinas confluence: satellite and in situ observations, *J. Clim.*, **18**, 3470-3482, doi: 10.1175/JCLI3485.1.

von Storch J. S., H. Sasaki, and J. Marotzke, 2007: Wind-generated power input to the deep ocean: an estimate using a 1/10 general circulation model. *J. Phys. Oceanogr*., **37**, 657-672.

von Storch J. S., C. Eden, I. Fast, H. Haak, D. Hernandez-Deckers, E. Maier-Reimer, J. Marotzke, and D. Stammer, 2012: An estimate of the Lorenz energy cycle for the world ocean based on the STORM/NCEP simulation. *J. Phys. Oceanogr*., **42**, 2185-2205.

Wallace, J. M., T. P. Mitchell, and C. Deser, 1989: The influence of sea surface temperature on surface wind in the eastern equatorial Pacific: Seasonal and interannual variability. *J. Climate,* **2***,* 1492–1499.

Witter, D. L. and D. B. Chelton, 1998: Eddy-mean flow interaction in zonal oceanic jet flow along zonal ridge topography, *J. Phys. Oceanogr.*, **28**, 2019-2039

Wunsch, C., 1998: The work done by the wind on the oceanic general circulation. *J. Phys. Oceanogr.*, **28**, 2332-2340.

Wunsch, C. and R. Ferrari, 2004: Vertical mixing, energy and the general circulation of the oceans, *Annu. Rev. Fluid Mech.*, **36**, 281-314.

Xie, S.-P., 2004: Satellite observations of cool ocean –atmosphere interaction, *Bull. Amer. Meteor. Soc*., **85**, 195-208, doi: 10.1175/BAMS-85-2-195.

Xu, Y. and R. B. Scott, 2008: Subtleties in forcing eddy resolving ocean models with satellite wind data. *Ocean Model.*, **20***,* 240-251.

Xu, C., X. Zhai and X. Shang, 2016: Work done by atmospheric winds on mesoscale ocean eddies. *Geophys. Res. Lett.,* **43***,* 12, 174-12, 180, doi:10.1002/2016GL071275.

Xu, R., F. Tian, L. Yang, H. Hu, H. Lu and A. Hou, 2017: Ground validation of GPM IMERG and TRMM 3B42V7 rainfall products over southern Tibetan Plateau based on a high-density rain gauge network, *J. Geophys. Res.*, **122**, 910-924, doi: 10.1002/2016JD025418

Zhai X., and R. J. Greatbatch, 2007: Wind work in a model of the northwest Atlantic Ocean. *Geophys. Res. Lett.,* **34***,* L04606.

Zhai, X., H. L. Johnson, D. P. Marshall, and C. Wunsch, 2012: On the wind power input to the ocean general circulation. *J. Phys. Oceanogr.*, **42,** 1357-1365.

Zhang, Z., W. Wang, and B. Qiu, 2014: Oceanic mass transport by mesoscale eddies. *Science*, **345**, 322-324.